Physique mésoscopique d'un gaz de Bose unidimensionnel : courants permanents et excitations dipolaires collectives

Marco Cominotti

UNIVERSITÉ DE GRENOBLE

THÈSE

Pour obtenir le grade de

DOCTEUR DE L'UNIVERSITÉ DE GRENOBLE

Spécialité : **Physique Théorique**

Arrêté ministériel : 7 Août 2006

Présentée par

Marco COMINOTTI

Thèse dirigée par **Anna MINGUZZI**
et codirigée par **Frank W. J. HEKKING**

préparée au sein du
Laboratoire de Physique et Modélisation des Milieux Condensés
et de l' **École Doctorale de Physique**

Physique mésoscopique d'un gaz de Bose unidimensionnel : courants permanents et excitations dipolaires collectives

Thèse soutenue publiquement le **9 Octobre 2015**,
devant le jury composé de :

Mme. Julia Meyer
Université de Grenoble, CEA Grenoble INAC/SPSMS, Grenoble, Présidente
Mme. Isabelle Bouchoule
Laboratoire Charles Fabry, Institut d'Optique/CNRS, Palaiseau, Rapportrice
Mr. Wilhelm Zwerger
Technische Universität München, Garching, Allemagne, Rapporteur
Mme. Veronica Ahufinger Breto
Universitat Autònoma de Barcelona, Bellaterra, Espagne, Examinatrice
Mr. Sandro Stringari
Università di Trento, INO-CNR BEC Center, Povo, Italie, Examinateur
Mme. Anna Minguzzi
LPMMC, Grenoble, Directrice de thèse
Mr. Frank W. J. Hekking
Université de Grenoble, LPMMC, Grenoble, Co-Directeur de thèse

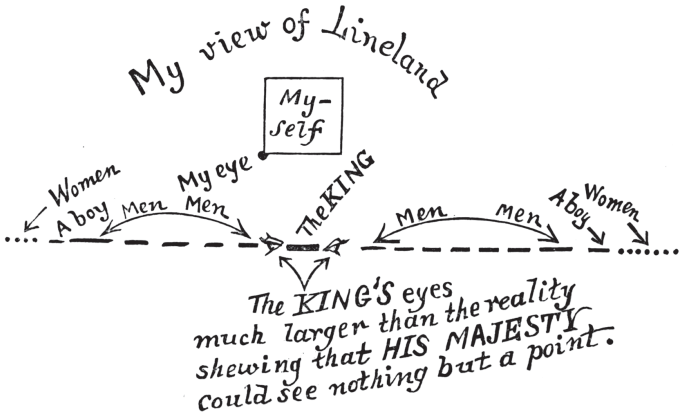

How I had a Vision of Lineland

Having amused myself till a late hour with my favourite recreation of Geometry, I had retired to rest with an unsolved problem in my mind. In the night I had a dream. I saw before me a vast multitude of small Straight Lines – all moving to and fro in one and the same Straight Line. [. . .] Approaching one [. . .], replied the small Line "I am the Monarch of the world." [. . .]

It seemed that this poor ignorant Monarch – as he called himself – was persuaded that the Straight Line which he called his Kingdom, and in which he passed his existence, constituted the whole of the world, and indeed the whole of Space. Not being able either to move or to see, save in his Straight Line, he had no conception of anything out of it. [. . .]

His subjects – of whom the small Lines were men and the Points Women – were all alike confined in motion and eye-sight to that single Straight Line, which was their World. [. . .] Moreover, as each individual occupied the whole of the narrow path, so to speak, which constituted his Universe, and no one could move to the right or left to make way for passers by, it followed that no Linelander could ever pass another. Once neighbours, always neighbours. [. . .]

Such a life, with all vision limited to a Point, and all motion to a Straight Line, seemed to me inexpressibly dreary; and I was surprised to note the vivacity and cheerfulness of the King.

E. A. Abbott, *Flatland: A Romance of Many Dimensions*, 1884.

Table of Contents

Preface

THIS thesis summarizes the main topics of the research activity I have performed during the three years of my PhD education at the *Laboratoire de Physique et Modélisation des Milieux Condensés* in Grenoble, as a student of the *Ecole doctorale de Physique* of the *Université de Grenoble*, under the supervision of Dr. Anna Minguzzi and Prof. Frank Hekking. The object of this thesis is the study of one-dimensional mesoscopic quantum systems constituted by ultracold atomic Bose gas.

The interest in one-dimensional (1D) quantum many-body systems dates back to the early years of Quantum Mechanics. One reason is that 1D systems often constitute simple toy-models, in which analytical approaches are applicable. For example, in his pioneering work of 1931, H. Bethe found an exact solution to the 1D Heisenberg model using the famous ansatz for the wave function that nowadays bears his name [1]. Subsequently, during the last century, the study of 1D quantum many-body systems has led to the discovery of other paradigmatic examples of exactly solvable models, such as the Lieb-Liniger, and the Hubbard ones, as well as to the development of powerful theoretical methods especially suited for 1D systems [2, 3], such as the Luttinger liquid theory, just to cite one of the most celebrated. One-dimensional quantum systems have thus been found to present interesting, unexpected and often counterintuitive features, as compared to their higher-dimensional counterparts. For instance, the reduced dimensionality drastically affects the nature of the excitations. Also the effects of quantum fluctuations and interparticle interactions are greatly enhanced as compared to higher dimensions, thus leading to different phases, superfluid properties and even to the surprising phenomenon of statistical transmutation: strongly interacting bosons that display fermionic properties. The interest in such low-dimensional systems, however, is not restricted to a purely fundamental ground. The technological developments of the 20th and 21st centuries in the fields of chemical synthesis, microfabrication, criogeny, and, more recently, control and manipulation of ultracold

atomic gases through light-matter interaction, led to the discovery and realization of many (quasi-)1D systems, such as carbon nanotubes [4], quantum wires [5–7], Josephson junctions arrays [8], liquid ^{4}He in elongated nanopores [9], and ultracold atomic gases confined in very anisotropic traps. In particular, ultracold atomic gases have become object of intense experimental and theoretical research in the 1990s, triggered by the first achievement of Bose-Einstein condensation in dilute vapours of alkali atoms cooled down to fractions of microkelvin [10,11]. Subsequently, the aforementioned experimental progress in cooling, trapping and manipulating such systems has reached an extraordinary and unprecedented degree of control of the parameters of the system, whose dimensionality, geometry and interparticle interactions can be adjusted at will [12]. In recent experiments, quantum state preparation of few-particle states with a control even at the single atom level have been demonstrated [13]. Thanks to this progress, ultracold atomic gases are considered nowadays as model quantum fluids, that find applications in the field of quantum simulation [14], the study of quantum physics problem by mimicking hardly accessible systems via analogous and easily controllable cold atomic ones, and, more recently, in the emerging one of atomtronics [15], that aims to realize atomic-based devices counterparts of electronic ones, with applications *e.g.* in quantum computation.

The aim of this PhD thesis is to study theoretically a few 1D mesoscopic systems of ultracold bosonic gases which exhibit interesting quantum phenomena, and are also potentially relevant for some new technological applications. In particular, as a recurring theme in this thesis, I focus on the interplay of effects arising from the presence of interactions, quantum fluctuations and of localized potential barriers in the systems, whose contributions are all enhanced in 1D. The manuscript starts with a general chapter introducing the 1D Bose gas, followed by three chapters, each dedicated to a specific system. The thesis is completed by three appendixes which detail some calculations.

The thesis is organized as follows. The *first chapter* provides a general introduction to the physics of the 1D Bose gas. It includes a description of its experimental realization with ultracold atomic gases, a discussion of its most important and peculiar physical features, and a description of the interparticle interactions, pointing out the main differences between the weak- and strong-interaction regimes. Then, the theoretical methods employed to describe the 1D Bose gas in different physical regimes are explained in detail. These methods will be used in the research projects described in the following chapters.
In the *second chapter* we study the phenomenon of persistent currents in a system of interacting 1D bosons confined in a ring trap and subjected to a rotating barrier poten-

tial. By employing a combination of analytical and numerical techniques, we provide a complete characterization of the persistent current amplitude in the system, as a function of the interparticle interaction strength and of the system size. We identify the existence of a regime of maximal screening of the barrier by the fluid, arising from the interplay between classical and quantum screening. In this regime, the persistent current amplitude is maximal and its scaling behaviour with the system size is most favourable for its observation.
In the *third chapter* we consider an interacting Bose gas confined in a 1D ring-shaped optical lattice, in the presence of an artificial gauge potential and a potential barrier, realizing an atomtronic quantum interference device. Such system has been proposed for the realization of atomic flux-qubits and macroscopic superpositions of current states for quantum computation. We perform a systematic study of the quality of the qubit realized by such system, identifying the best system's parameters regime for its realization, definition and detection via time-of-flight measurements of the momentum distribution.
In the *fourth chapter* we study the dipolar excitation of a Bose gas confined in a 1D split trap, subjected to a sudden quench of the center of the trapping potential. We characterize the oscillation frequency of the system in all the interaction regimes, by a combination of theoretical and analytical techniques. We find a non-trivial dependency of the oscillation frequency on the interaction strength. Also in this case this is understood in terms of barrier screening and renormalization, showing that this phenomenon, first elucidated in the study of persistent currents, is very generally affecting various physical observables. Furthermore, we find a surprising parity effect in the oscillation frequency at strong interactions, originated from the statistical transmutation of the strongly correlated Bose system, and reminiscent of fermionic transport processes.
Finally, the manuscript ends with a summary of the main original results of the research projects presented in the thesis, together with an outlook for future research.

List of publications

The original results presented in this thesis have been published in the following articles:

(i) M. Cominotti, D. Rossini, M. Rizzi, F. Hekking, and A. Minguzzi. Optimal Persistent Currents for Interacting Bosons on a Ring with a Gauge Field, *Phys. Rev. Lett.*, **113**, 025301, 2014. Ref. [16].

(ii) M. Cominotti, M. Rizzi, D. Rossini, D. Aghamalyan, L. Amico, L.-C. Kwek, F. Hekking, and A. Minguzzi. Optimal scaling of persistent currents for interacting bosons on a ring, *The European Physical Journal Special Topics*, **224**, 519, 2015. Ref. [17].

(iii) D. Aghamalyan, M. Cominotti, M. Rizzi, D. Rossini, F. Hekking, A. Minguzzi, L.-C. Kwek, and L. Amico. Coherent superposition of current flows in an Atomtronic Quantum Interference Device, *New J. Phys.*, **17**, 045023, 2015. Ref. [18].

(iv) M. Cominotti, F. Hekking, and A. Minguzzi. Dipole mode of a strongly correlated one-dimensional Bose gas in a split trap: Parity effect and barrier renormalization, *Phys. Rev. A*, **92**, 033628, 2015. Ref. [19].

Préface

Cette thèse théorique résume les principaux projets de recherche que j'ai abordés au cours de mon doctorat au sein du Laboratoire de Physique et Modélisation des Milieux Condensés à Grenoble, en tant que doctorant de l'Ecole doctorale de Physique de l'Université de Grenoble, sous la direction d'Anna Minguzzi et de Frank Hekking. L'objet de cette thèse est l'étude de systèmes quantiques mésoscopiques unidimensionnels constitués par des gaz d'atomes ultrafroids, qui presentent des phénomènes quantiques intéressants, et pourraient mener à de nouvelles applications technologiques. Mon étude prend en compte les effets combinés des interactions, des fluctuations quantiques et des barrières de potentiel localisés dans les systèmes, dont l'effet est plus fort en une dimension qu'en dimensions supérieures. Le manuscrit commence par un chapitre général qui introduit le gaz de Bose en une dimension, suivi de trois chapitres, chacun dédié à l'étude théorique d'un système spécifique. La thèse est complétée par trois annexes qui détaillent certains calculs.

Chapter 1

Theoretical methods for one-dimensional bosons

1.1 Introduction

THIS first chapter is devoted to a general review of the properties of the one-dimensional (1D) Bose gas of ultracold atoms, and of the theoretical methods that have been employed to study it in different physical regimes in the following chapters. In particular we focus on the effect of interparticle interactions. A more specific introduction and motivation to the systems and problems that have been studied is given in the following dedicated chapters. I would like to stress that several of the methods mentioned in this chapter, and of the results discussed later, are not specific for 1D ultracold atomic gases, but are in fact more general and could be extended to other quantum fluids of different nature.

1.1.1 One-dimensionality

The realization of 1D systems of ultracold atoms is obtained by tightly confining, through very anisotropic trapping potentials, the motion of the atoms in two directions (the transverse directions), limiting their motion to zero point oscillations. Then, the 3D many body wave function can be factorized as

$$\Psi(\mathbf{r}_1, ..., \mathbf{r}_N) = \Psi(x_1, ..., x_N) \prod_{i=1}^{N} \phi_0(\mathbf{r}_{i\perp}) \,, \tag{1.1}$$

where $\mathbf{r}_{i\perp} = (y_i, z_i)$ and $\phi_0(\mathbf{r}_\perp)$ is the single particle wave function that corresponds to the lowest energy transverse quantum state. To reach this situation, the energy

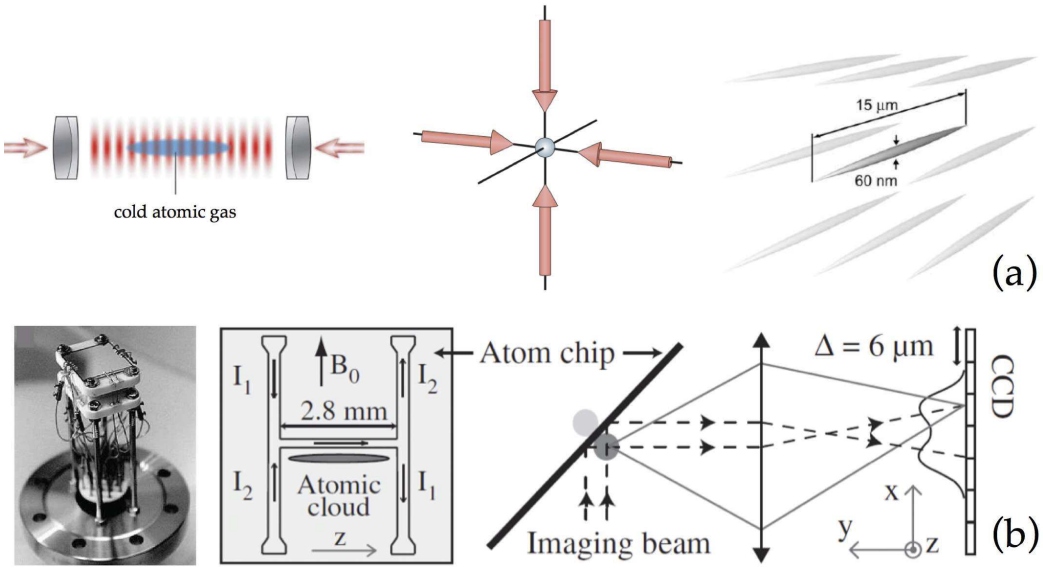

Figure 1.1: **(a)** Superposition of two counter-propagating laser beams creating a standing wave periodic potential for the atoms. Superpostion of two of orthogonal standing waves creating a 2D optical lattice, resulting in an array of 1D tubes (From Ref. [20–22]). **(b)** Atom chip magnetically trapping the atoms in a single tube, and imaging system (From Ref. [23, 24]).

scale associated with the energy gap of the transverse confinement should be much larger than all the other energy scales present in the system, such as thermal energy and chemical potential, which assuming a harmonic transverse confinement with frequency $\omega_\perp$, translates into the condition

$$\hbar\omega_\perp \gg k_B T,\ \mu\ . \tag{1.2}$$

In this case, the transverse degrees of freedom are frozen out and one can focus only on the degrees of freedom described by $\Psi(x_1, ..., x_N)$, and thus kinematically the gas is 1D. The value of the effective 1D interparticle interaction depends on the transverse confinement, as I will detail in the next section.

The experimental realization of such very anisotropic confinements for the atoms is most commonly achieved via two possible schemes. (i) Atoms can be trapped in 2D optical lattices, which are realized superimposing two orthogonal light standing waves. Each light standing wave, in turn, is realized superimposing two counter-propagating laser beams. The dipole force acting on the atoms, as a consequence of the ac-Stark shift, localizes the atoms in the minima (or maxima) of the intensity of the light wave, depending whether the laser frequency is blue (or red) detuned with respect to the corresponding atomic transition frequency. In this way an array of tightly

confining 1D potential tubes is created [12,21] (see Fig. 1.1(a)). (ii) In a second scheme, atoms can be magnetically trapped in an atom chip. In the microchip magnetic fields are created via the the current flowing in microscopic wires and electrodes microfabricated on a carrier substrate. The precision in the fabrication of such structures allows for a very good control of the generated magnetic field, that via the Zeeman force acting on the atoms designs the potential landscape [23] (see Fig. 1.1(b)). In this latter configuration a single 1D sample can be produced, instead of an array of several copies like with the optical lattice. Both techniques are nowadays employed in several laboratories around the world, among which we may cite [23–40].

1.1.2 Interactions in one-dimension

In a dilute and ultracold gas the interactions between the particles are due only to two-body collisions. These collisions, at low-energy, can be characterized by a single parameter, the s-wave scattering length a, independently of the details of the two-body potential $V(\mathbf{r}-\mathbf{r}')$. This allows to introduce the effective contact interaction potential $V(\mathbf{r}-\mathbf{r}') = g\delta(\mathbf{r}-\mathbf{r}')$, where the interaction strength g is related to the scattering length a through $g = 4\pi\hbar^2 a/m$ [41]. The scattering problem, however, is modified by the presence of an external tight confinement and the interaction coupling is modified in lower dimensionalities with respect to the 3D case. For example, in the experimentally relevant case of a tight 2D harmonic confinement of frequency $\omega_\perp$, that restrict the system to an effective 1D geometry, it has been shown in [42] that the effective 1D scattering length a_{1D} reads

$$a_{1D} = -\frac{a_\perp^2}{2a}\left(1 - C\frac{a}{a_\perp}\right) , \tag{1.3}$$

where $a_\perp = \sqrt{\hbar/m\omega_\perp}$ is the transverse harmonic oscillator length, and $C = |\zeta(1/2)| = 1.4603...$, where $\zeta(...)$ is the Riemann zeta function. Then the effective contact interaction strength in 1D is related to the effective 1D scattering length a_{1D} by

$$g_{1D} = -\frac{2\hbar^2}{m a_{1D}} . \tag{1.4}$$

The dependence of a_{1D} and g_{1D} on the 3D s-wave scattering length a is shown in Fig. 1.2. In the rest of this thesis, since I will always refer to 1D systems, for the sake of compactness I will indicate the 1D effective interaction strength g_{1D} simply as g.

The interaction strength between the particles in 1D can be modified by tuning the transverse confinement frequency alone. This technique, which goes under the name of confinement-induced-resonance, is an additional tool, compared to higher dimen-

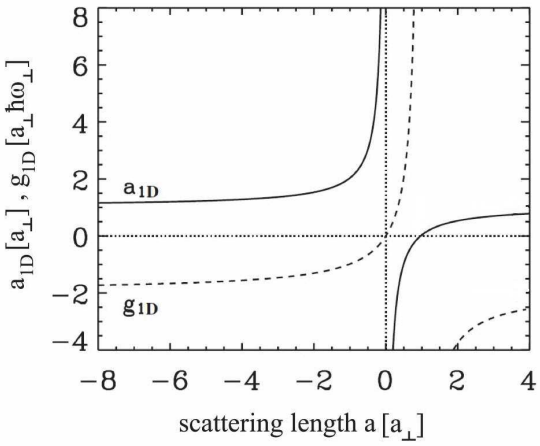

Figure 1.2: Effective 1D scattering length a_{1D} and interaction strength g_{1D} vs. the 3D s-wave scattering length a, in units of the transverse oscillator length $a_\perp$ and the radial oscillator frequency $\omega_\perp$. (Figure from Ref. [44]).

sions, to tune the interparticle interaction strength. Another possibility, which is not specific for low-dimensional system, is the application of external magnetic fields, that through Feshbach resonances allows to tune the strength of the interparticle interactions, even allowing a change from repulsive to attractive [43].

A useful dimensionless interaction parameter, that allows to quantify whether the system is in a weakly or strongly interacting regime, is given by the ratio between the interaction energy per particle, $E_{int} = n_0 g$, with n_0 the average system density, and the characteristic kinetic energy of particles at a mean separation $1/n_0$ between them, $E_{kin} = \hbar^2 n_0^2/m$

$$\gamma = \frac{E_{int}}{E_{kin}} = \frac{mg}{\hbar^2 n_0} \,. \tag{1.5}$$

A small value of γ corresponds to a weakly interacting system, in which particles tend to be delocalized and overlap. On the contrary, a large value of γ corresponds to a strongly interacting system, in which particles tend to avoid each other, hence are spatially localized by the strong correlations among each other, as illustrated in Fig. 1.3. In the limit of infinitely strong repulsive interactions ($\gamma \to \infty$), the so-called Tonks-Girardeau regime, the interactions mimic Pauli's exclusion principle and bosons behave in various respects like fermions. This shows the absence of a well defined concept of statistics in 1D (see Sec. 1.2). From Eq. (1.5) one can observe another peculiar property of a 1D gas, which becomes more strongly interacting at decreasing the particle density, counterintuitively and differently with respect to higher dimensions.

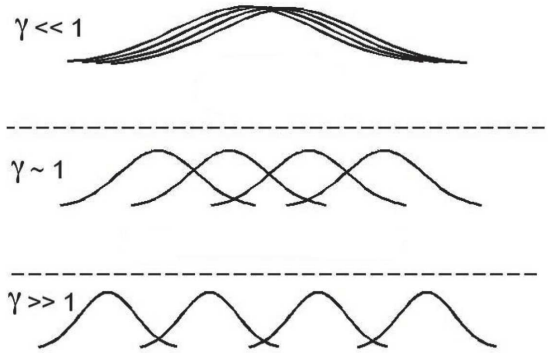

Figure 1.3: Cartoon of the 1D atomic distribution, illustrating the size and separation of single-particle wave functions as a function of the dimensionless interaction parameter γ. (Figure adapted from Ref. [27]).

1.1.3 Coherence properties of one-dimensional bosons

One-dimensional Bose systems at low temperature display peculiar coherence properties, drastically changed with respect to their higher dimensional counterparts. One reason lies in the fact that in 1D being all the transverse degrees of freedom frozen, quantum fluctuations can only propagate longitudinally, and this implies that their effect is enormously enhanced. A major difference with respect to higher dimensional systems is for instance the absence of Bose-Einstein condensation (BEC) in an interacting 1D Bose gas in the thermodynamic limit ($N, L \to \infty$, where N is the total number of particles and L the system size, with $n_0 = N/L$ constant), both at finite and zero temperature. Bose-Einstein condensation can be defined in two ways: in a homogeneous system by the presence of off-diagonal long range order, namely a non vanishing value of the one-body density matrix $g^{(1)}(x, x') = \langle \psi(x)^\dagger \psi(x') \rangle$ at long distances $|x - x'| \to \infty$ [45], where $\psi(x)$ is the bosonic field operator, or by the presence of a macroscopic eigenvalue in the one-body density matrix, of the order of the total number of particles [46]. The latter definition holds also for a confined system. The two definitions underline two of the main features of BEC: phase coherence over the whole system size and macroscopic occupation of a single quantum state [41]. In the thermodynamic limit, and at finite temperatures, the momentum distribution $n(k)$ of the Bose gas presents a quadratic infrared divergence as predicted by the Hohenberg theorem [47]:

$$n(k) \geqslant \frac{m k_{\mathrm{B}} T}{k^2} \frac{N_0}{N} - \frac{1}{2} \,, \tag{1.6}$$

where N_0 is the number of condensed particles. This inequality states the absence of condensation according to the Penrose-Onsager criterion: the fraction of condensed particles N_0 can not be of macroscopic order, since the total number of particles $N =$

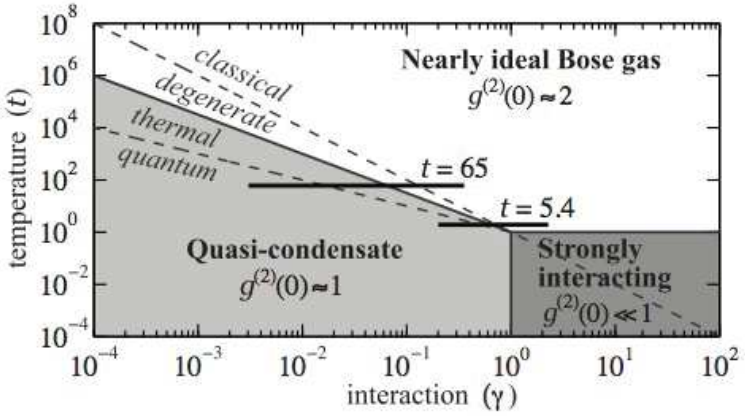

Figure 1.4: Phase diagram in the dimensionless interaction-temperature ($t = \hbar 2 k_{\mathrm{B}} T / m g^2$) parameter space for a repulsive uniform 1D Bose gas, derived from atom number fluctuations measurements [39]. $g^{(2)}(0)$ is the local two-body correlation, indicated for the three main regimes (white and grey areas). The two black horizontal lines show the parameters regimes explored in the experiment. (Figure from Ref. [39]).

$\int \mathrm{d}k\ n(k)$ must be finite. Also, the one-body density matrix decays exponentially at large distances, due to long-wavelength quantum fluctuations that prevent long range phase coherence. Despite the absence of condensation, however, a rich behaviour is found upon varying the interaction strength from weakly to strongly repulsive [24,39], as it is shown in Fig. 1.4. At zero temperature condensation is also prevented. The momentum distribution $n(k)$ presents a linear infrared divergence [48]:

$$n(k) \underset{k \to 0}{\geqslant} \frac{m v_s}{2\hbar k} \frac{N_0}{N} - \frac{1}{2}\,, \tag{1.7}$$

where v_s is the sound velocity of Bogoliubov excitations. Also in this case this inequality states the absence of condensation, because N_0 can not be of macroscopic order to have a finite number of particles $N = \int \mathrm{d}k\ n(k)$. At zero temperature, however, the one-body density matrix presents a power-law decay $g^{(1)}(x, x') \propto |x - x'|^{-1/2K}$, where $K \geqslant 1$ is the interaction dependent Luttinger parameter (see Sec. 1.4) [49,50], and one can speak of algebraic or quasi-long range order and of a quasi-condensate phase [51]. For a trapped system, such as in the presence of harmonic confinement, the density of states is modified compared to the homogeneous case, but BEC is still prevented in the thermodynamic limit, the critical transition temperature going to zero [52]. For a finite system size and number of particles, and at very low temperatures, instead, the system can exhibit a large occupation of a single-particle state and the phase coherence can extend to the whole system, thus reaching a true-condensate regime [51].

1.1.4 Theoretical Methods

To describe 1D systems of interacting bosons there are various methods available that rely on different assumptions and approximations. In the next sections I will review the methods that have been employed to obtain the results presented in Chap. 2, 3, and 4. I will not provide an exhaustive description of all the methods present in the literature, since this goes beyond the scope of this thesis.

The 1D homogeneous Bose gas with arbitrary contact interactions is a very special quantum many-body problem, that, together with few other examples, is integrable via Bethe ansatz. This celebrated model goes under the name of Lieb-Liniger model, after the names of the two physicists that in 1963 found an exact solution for its many-body wave function [53, 54]. The availability of such an exact solution is not only relevant in itself for its beautiful mathematical rigour, but it is also very important as a benchmark to prove the validity of other approximated methods. The fact that this integrable model can not take into account the presence of an external potential however limits its applicability with respect to relevant experimental situations, where a external confinement is usually present. Therefore, in order to treat this general situation, other methods have been developed, that rely on different assumptions and approximations depending, for instance, on the interparticle interaction strength. I will describe in particular the exact solution based on the Tonks-Girardeau Bose-Fermi mapping in the infinitely strong (or hard-core) interacting limit, the mean-field Gross-Pitaevskii equation valid for weak interactions and large number of particles, the Luttinger liquid effective field theory approach valid at strong interactions when the low-energy excitations are collective phonon waves, and the numerical diagonalization method, applicable at any interaction strength but only for small system sizes. Another method that has been employed in the research projects presented in Chaps. 2, 3 is the numerical density-matrix renormalization group (DMRG) approach. This represents nowadays probably the most efficient numerical method for 1D quantum systems [55–57]. It is an iterative variational method based on a renormalization procedure, that allows to reduce the exponentially growing size of the Hilbert space to effective degrees of freedom that are the most important for a certain target state, *e.g.* the ground state. Since the implementation and use of this method was not the object of my research activity, but was done by other researchers [1] within a scientific collaboration with our group, I will not present in this thesis the details of this technique.

[1] The implementation of the DMRG method has been done by Matteo Rizzi (Institut für Physik, Johannes Gutenberg-Universität, Staudingerweg 7, D-55099 Mainz, Germany), and Davide Rossini (NEST, Scuola Normale Superiore and Istituto Nanoscienze-CNR, I-56126 Pisa, Italy).

1.2 Tonks-Girardeau Bose-Fermi mapping

The general Hamiltonian describing a system of N bosons of mass m in 1D, interacting via the contact potential $V(x-x') = g\delta(x-x')$, and subjected to an external potential $V_{\rm ext}(x)$, is given in first quantization by

$$\mathcal{H} = \sum_{j=1}^{N} -\frac{\hbar^2}{2m}\frac{\partial^2}{\partial x_j^2} + V_{\rm ext}(x_j) + \frac{g}{2}\sum_{j,l=1}^{N}\delta(x_j - x_l)\ , \tag{1.8}$$

where x_j is the j-th particle coordinate. The problem of solving the full many-body Schrödinger equation associated to this Hamiltonian is very hard. In the general case, an exact solution can be obtained only through *ab initio* numerical simulations, based for instance on Quantum Monte Carlo or DMRG techniques, that are exact within statistical errors. However, in the limit of infinitely strong contact repulsion between the bosons (impenetrable or hard-core bosons) $g \to \infty$, an exact solution exists for the bosonic many-body wave function $\Psi_B(x_1, ..., x_N)$. This solution, that was introduced by M. D. Girardeau in 1960 [58], constitutes to some extent a particular case of the Bethe anzatz Lieb-Liniger exact solution [53, 54] that is valid at arbitrary interaction strength, but at the same time an important generalization of the latter, being applicable also in the case of an inhomogeneous system in the presence of an external potential. The Bose gas in the infinitely interacting limit is usually referred to in the literature as Tonks-Girardeau (TG) gas, after the physicists M. D. Girardeau and L. Tonks.

The presence of the interacting contact potential between the particles can be translated into the well-known cusp condition for the many-body wave function

$$\frac{\hbar}{2mg}\left[\left(\frac{\partial\Psi_B}{\partial x_j} - \frac{\partial\Psi_B}{\partial x_l}\right)_{x_j=x_l^+} - \left(\frac{\partial\Psi_B}{\partial x_j} - \frac{\partial\Psi_B}{\partial x_l}\right)_{x_j=x_l^-}\right] = \Psi_B(x_j = x_l)\ . \tag{1.9}$$

In the infinitely interacting limit $g \to \infty$, this expression implies that Ψ must vanish at contact between two particles

$$\Psi_B(x_1, ..., x_N) = 0 \ \text{ if } \ x_j = x_l,\ 1 \leqslant j < l \leqslant N\ . \tag{1.10}$$

The surfaces $x_j = x_l$ thus divide the N-dimensional configuration space into $N!$ disconnected regions, usually referred to as coordinate sectors, in each of which the many-body problem is reduced to a non interacting one. Girardeau then observed that such a bosonic wave function has a property in common with the wave function of a spin-polarized (or spinless) fermionic system subjected to the same boundary

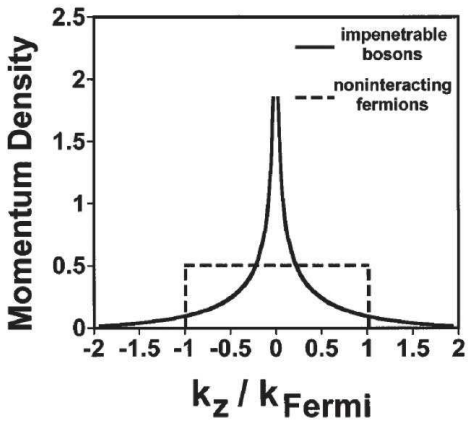

Figure 1.5: Comparison between the momentum distribution of a TG Bose gas and a non-interacting Fermi gas at zero temperature in the thermodynamic limit. (Figure from Ref. [42]).

conditions and external potential, which also must vanish at contact between two particles, as imposed by Pauli's exclusion principle. From these two observations, he had the idea that the bosonic many-body wave function for the infinitely interacting problem can be expressed in terms of the many-body wave function of spin-polarized (or spinless) non-interacting fermions subject to the same external potential, through the Bose-Fermi mapping:

$$\Psi_B(x_1, ..., x_N) = \mathcal{A}(x_1, ..., x_N)\Psi_F(x_1, ..., x_N) \ , \tag{1.11}$$

where the fermionic wave function is given by the Slater determinant

$$\Psi_F(x_1, ..., x_N) = (1/\sqrt{N!})\mathrm{det}[\psi_k(x_j)]_{k,j=1...N} \ , \tag{1.12}$$

$\psi_j(x_k)$ being the single-particle orbitals for the given external potential labelled by the index k, and $\mathcal{A}(x_1, ..., x_N)$ is a unitary mapping function, antisymmetric under exchange of two particles, that ensures the proper overall bosonic symmetry under exchange of two particles

$$\mathcal{A}(x_1, ..., x_N) = \prod_{1 \leqslant i < l \leqslant N} \mathrm{sgn}(x_i - x_l) \ . \tag{1.13}$$

The bosonic and fermionic wave functions then differ only by an overall phase factor in each coordinate sector. As a consequence, all the observables of the TG Bose gas that do not depend on the sign of the many-body wave function coincide with the

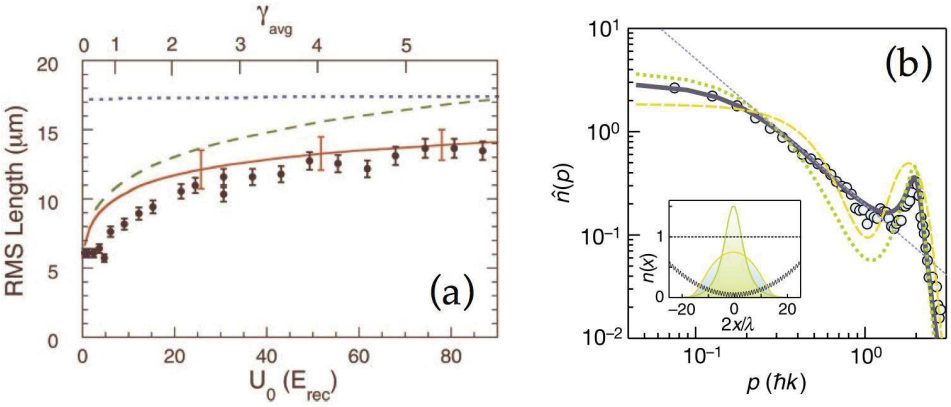

Figure 1.6: First experimental observations of the TG regime. **(a)** Increasing the interaction strength γ between the particles, the cloud size slowly approaches the one predicted for the TG gas, indicated by the horizontal dotted line. The measured values coincide with the solid curve which represents the expected behaviour of the 1D Bose gas theory. The dashed line represents a mean-field calculation (Figure from Ref. [27]). **(b)** Momentum distribution of the 1D atomic gas in an optical lattice. The dots represent measured data whereas the lines correspond to the computed momentum distributions. The green dotted line represents ideal bosons, the yellow dashed line represents the ideal Fermi gas and the gray solid line represents the TG gas. Due to the non-uniformity of the TG gas on the lattice, the slope of the linear part in the double logarithmic plot deviates from the expected 1/2 behaviour of the uniform TG gas indicated in short dashes (Figure from Ref. [28]).

corresponding ones of the mapped Fermi gas, we may cite as an example the particle and current densities, and the energy spectra. For this reason the TG gas is often called also fermionized Bose gas. The ground-state energy of the TG gas for instance is given by $E_{TG} = \sum_{i=0}^{N-1} \varepsilon_i$, where ε_i are the single-particle energies, and the particle density by $n(x) = \sum_{i=0}^{N-1} |\psi_i(x)|^2$. On the other hand, all the quantities sensitive to the relative phases imposed by the mapping function, such as the one-body density matrix $g^{(1)}(x, x') = \int \mathrm{d}x_2 ... \mathrm{d}x_N \ \Psi_B^*(x, x_2, ..., x_N)\Psi_B(x', x_2, ..., x_N)$, and the momentum distribution $n(k) = \int \mathrm{d}x \int \mathrm{d}x' \ g^{(1)}(x, x')e^{ik(x-x')}$, are markedly different for bosons as compared to fermions. A comparison between the fermionic momentum distribution and the TG bosonic one is shown in Fig. 1.5. As it is expected, the Fermi system is dominated by the effect of the exclusion principle and the momentum states occupation is uniform and equal to 1 up to the Fermi momentum and zero otherwise. In contrast, the TG bosonic system reflects tendency toward condensation, even if the $1/\sqrt{k}$ peak at low momenta [59] proves the absence of a true BEC. This is confirmed also by the fact that the largest eigenvalue of the one-body density matrix scales as $\sqrt{N}$ [60]. At high momenta, also in contrast with the Fermi system, the TG Bose gas displays a $1/k^4$ long tail decay that is found to be an universal feature [61, 62].

The extension of the mapping (1.11) to the time-dependent case becomes straightforward, after remarking that the impenetrability condition and the consequent separation of the many-body wave function in disconnected coordinate sectors hold at any time, and that consequently the Bose-Fermi mapping can be applied for any configuration of the particles, at any time [63]:

$$\Psi_B(x_1, ..., x_N; t) = \mathcal{A}(x_1, ..., x_N)\Psi_F(x_1, ..., x_N; t) \ , \tag{1.14}$$

where the mapping function $\mathcal{A}$ is the same as the one found for the time-independent case, Eq. (1.13), and does not entails explicitly the dependence on time.

Experimentally, the 1D TG strongly interacting regime has been reached for the first time in 2004 by two different groups [27, 28], that demonstrated the successful fermionization measuring respectively the cloud size and the momentum distribution of the gas, as illustrated in Fig. 1.6.

In Chaps. 2, 3, and 4 I will show properties of the TG Bose gas that are peculiar of fermionic system, such as a parity effect, leading to different values of a given observable depending on whether the number of particles is even or odd, and the appearance of Friedel oscillations of the density in the proximity of an abrupt potential (see *e.g.* Fig. 2.6). Furthermore, I will show that the TG exact solution can be used not only to study the behaviour of a 1D Bose gas in the infinitely interacting limit, but also as a valuable benchmark to compare with other approximated methods, as the Luttinger liquid theory, and to fix some non universal parameters present in the theory.

1.3 Gross-Pitaevskii equation

As I have stressed in the previous section, the many-body quantum problem to solve the Schrödinger equation associated with Hamitonian (1.8) is very hard in general, both analytically and numerically. A common approach that is developed to tackle it is based on the mean-field approximation, that in the context of ultracold dilute quantum gases has been proven to be very successful in providing not only qualitative but also quantitative predictions for static, dynamic and thermodynamic properties [41, 64].

The mean-field description of a zero-temperature Bose gas of N particles is based on the assumption that the many body wave function can be written in Hartree approximation as a symmetrized product of single-particle wave functions, that in the

fully condensed state all coincide with the same single-particle state $\phi(x)$

$$\Psi_B(x_1, ..., x_N, t) = \prod_{i=1}^{N} \phi(x_i, t) \ . \tag{1.15}$$

This approximation amounts thus to neglecting all the correlations between the particles, that are not taken into account by this form of the wave function, and that become less and less important as the interparticle interactions are weakened ($\gamma \ll 1$). Also, it neglects the quantum depletion of the condensate, namely the fraction of particles that are not in the macroscopically occupied state. A large occupation of a single state is realized also in 1D, as we have seen in Sec. 1.1.3, even if the depletion is more important than in higher dimensions and one can not always speak of a true BEC [51]. In general, the depletion of the condensate is less and less important as the number of particles is increased [65]. Applying Hamiltonian (1.8) to the wave function written in this way, one gets the following expression for the energy of the system

$$E = N \int \mathrm{d}x \ \left[\frac{\hbar^2}{2m} |\partial_x \phi(x)|^2 + V_{\mathrm{ext}}(x) |\phi(x)|^2 + \frac{N-1}{2} g |\phi(x)|^4 \right] \ . \tag{1.16}$$

It is then convenient to introduce the so-called wave function of the condensate

$$\Phi(x) = \sqrt{N} \phi(x) \ , \tag{1.17}$$

where the same single-particle state $\phi(x)$ is normalized to unity. The density of particles is thus given by $n(x) = |\Phi(x)|^2$, and under the assumption $N \gg 1$, the energy functional of the system can be rewritten as

$$E \simeq \int \mathrm{d}x \ \left[\frac{\hbar^2}{2m} |\partial_x \Phi(x)|^2 + V_{\mathrm{ext}}(x) |\Phi(x)|^2 + \frac{g}{2} |\Phi(x)|^4 \right] \ . \tag{1.18}$$

The optimal form for the ground-state of the condensate wave function is then found minimizing the energy functional (1.18), under the condition $N = \int \mathrm{d}x |\Phi(x)|^2$ that the total number of particles is constant. Therefore, equating to zero the variation of $E - \mu N$ with respect to $\Phi^*(x)$, where the Lagrange multiplier μ is the chemical potential, that ensures the constancy of the particle number, one finally gets the time-independent Gross-Pitaevskii (GP) equation, that was derived for the first time in 1961, independently by the physicists E. Gross and L. Pitaevskii [66, 67]:

$$-\frac{\hbar^2}{2m} \frac{\partial^2}{\partial x^2} \Phi(x) + V_{\mathrm{ext}}(x) \Phi(x) + g |\Phi(x)|^2 \Phi(x) = \mu \Phi(x) \ . \tag{1.19}$$

The time evolution of the condensate wave function can then be determined by

$$i\hbar\frac{\partial\Phi(x,t)}{\partial t} = \frac{\delta E}{\delta\Phi^*} \,. \tag{1.20}$$

If the external potential is independent of time, Eq (1.20) admits the stationary solution

$$\Phi(x,t) = \Phi(x,0)e^{-i\mu t/\hbar} \,. \tag{1.21}$$

Remarkably, the time evolution of the condensate wave function is thus determined by the chemical potential and not by the energy, as it happens with usual wave functions.

It is useful to remark for subsequent discussion, that in the case of a uniform Bose gas, in absence of motion of the center of mass, one can take $\Phi = \sqrt{N/L}$, where L is the system size, and Eq. (1.19) reduces to $\mu = gn$, with $E/L = gn^2/2$.

The GP equation is a nonlinear partial differential equation, which cannot be solved analytically in the general case. Exact analytical solutions may be found in special cases. A particularly famous class of these solutions for instance is represented by the solitary waves, or solitons. In Chap. 2 and App. A a special analytical solution of this equation is presented, for a gas in a ring geometry in the presence of a rotating potential barrier. In the general case, to solve the stationary GP equation (1.19) one can adopt a numerical method based directly on a self-consistent minimization the energy functional, as detailed in [68]. This method consists in projecting an initial arbitrary trial condensate wave function $\Phi(x)$ onto the minimum of the energy functional (1.18), by propagating it in imaginary time according to the diffusive equation

$$\hbar\frac{\partial\Phi(x,\tau)}{\partial\tau} = -\frac{\delta E}{\delta\Phi^*(x,\tau)} \,, \tag{1.22}$$

obtained from Eq. (1.20) applying the Wick rotation of the time coordinate $t \to -i\tau$. This self-consistent equation, under the further constraint of normalization, defines thus a trajectory in the wave function space, that for $\tau \to \infty$ converges to the exact solution which corresponds to $\partial\Phi/\partial\tau = 0$. In practice, the minimization of the gradient is done by choosing a time step $\Delta\tau$ and iterating the equation

$$\Phi(x,\tau+\Delta\tau) \simeq \Phi(x,\tau) - \Delta\tau\mathcal{H}_{GP}\Phi(x,\tau) \,, \tag{1.23}$$

where $\mathcal{H}_{GP} = -(\hbar^2/2m)\partial_x^2) + V_{\rm ext}(x) + g|\Phi(x)|^2$ depends nonlinearly on Φ, and normalizing the wave function to N at each iteration. The convergence of such an iterative procedure depends thus on the initial choice of the wave function, and its rate is controlled by the time step $\Delta\tau$.

1.4 Luttinger liquid effective field theory

The Luttinger liquid (LL) is a universality class of 1D quantum many-body systems, called in this way by Haldane [69] after the earlier contribution to their study of Luttinger [70], and sometimes also referred as Tomonaga-Luttinger liquid [71]. It includes a wide variety of celebrated 1D systems, among which we may cite the Bose gas with repulsive contact interactions, the Heisenberg model, interacting spinless and spin-$\frac{1}{2}$ fermions, electrons in the edge states of the quantum Hall effect, and many others [2]. At low temperatures all these systems exhibit a fluid phase in which no continuous or discrete symmetries are broken, in agreement with the Mermin-Wagner-Hohenberg theorem [47, 72], and that has the key feature that the low-energy excitations are collective modes with a gapless linear dispersion. Haldane brought a significant contribution to the development of a universal description of such systems in terms of a low-energy harmonic field theory approach [49], which corresponds to a quantum hydrodynamics description, in which the excitation spectrum is described in terms of non-interacting bosonic collective modes (bosonization). The collective nature of the elementary excitations in 1D can be easily understood in these terms: in the presence of interactions, any individual motion of a particle is immediately converted into a collective one, since a moving particle can not avoid its neighbours to propagate. This has also the consequence of greatly enhancing the effect of interactions between the particles in 1D.

Let us consider a homogeneous 1D system of length L, containing N particles. It is not necessary at this point to specify its boundary conditions. In order to construct a quantum hydrodynamic description of the system we consider the conjugate fields density $\rho(x)$ and velocity $v(x)$, that in the case of a potential flow can be expressed as the gradient of a dimensionless potential $\phi(x)$ as $v(x) = (\hbar/m)\partial_x\phi(x)$, satisfying the canonical commutation relation $[\rho(x), \phi(x')] = i\delta(x-x')$. The low-energy Hamiltonian of the system can be expressed in terms of such fields as

$$\mathcal{H} = \int_0^L \mathrm{d}x \ \left[\frac{1}{2}m\rho(x)v^2(x) + e(\rho)\right] , \tag{1.24}$$

where the first term corresponds to the kinetic energy density and the second to the internal energy one [73]. At low-energy and low-momenta the hydrodynamic description of the system can be simplified performing an expansion of Hamiltonian (1.24) for long wave-length and small fluctuations of the density and small velocities. Therefore, under the assumption that the velocity of the fluid $v(x)$, and the low-momenta ($|k| \ll n_0$) density fluctuation above the the equilibrium value of the density $\Pi(x) = \rho(x) - n_0$,

with $n_0 = N/L$, are small quantities of the same order, the first non-vanishing contributions to the Hamiltonian, after the constant zero-order terms, are of the quadratic form $(mn_0/2)v^2(x)$, and $(\partial^2 e(\rho)/\partial\rho^2)|_{\rho=n_0}\Pi^2(x)/2$. Hamiltonian (1.24) can then be recast in the harmonic-fluid form

$$\mathcal{H} = \frac{\hbar v_s}{2}\int_0^L \mathrm{d}x\ \left[\frac{K}{\pi}(\partial_x\phi(x))^2 + \frac{\pi}{K}\Pi^2(x)\right]\ , \tag{1.25}$$

by introducing the two parameters K and v_s, which are known respectively as the Luttinger parameter and the sound velocity, defined by $v_s K = \hbar\pi n_0/m$, and $v_s/K = (1/\hbar\pi)(\partial\mu_B/\partial\rho)|_{\rho=n_0}$, where $\mu_B = \partial E/\partial N$ is the chemical potential of the Bose gas [50]. From these relations one can see immediately that the Luttinger parameter K corresponds to the square root of the ratio between the adiabatic compressibility of an ideal Fermi gas in the same geometry, $\kappa_F = (\partial\mu_F/\partial\rho)|_{\rho=n_0} = \pi^2\hbar^2 n_0/m$, and the actual compressibility of the Bose gas $\kappa_B = (\partial\mu_B/\partial\rho)|_{\rho=n_0}$, $K = \sqrt{\kappa_F/\kappa_B}$, where μ_F is the chemical potentials of the Fermi gas.

The low-energy physics of the 1D Bose gas is thus governed by a quadratic Hamiltonian, with a linear and gapless sound waves excitation spectrum $\omega(k) = v_s k$, and two non-universal parameters v_s and K, that depend on the interaction strength g, the density n_0, and on the form of the compressibility of the gas. The terms of higher order in the expansion of Hamiltonian (1.24) represent the anharmonicity of the sound vibrations, taking into account phonon interactions.

The Luttinger parameter K and the sound velocity v_s are related to measurable properties of the systems. In some special cases, for which the corresponding microscopic model is integrable, they can be related to the microscopic ones. This is the case of the 1D Bose gas for which the Lieb-Liniger Bethe ansatz solution exists [53, 54], as illustrated in Fig. 1.7. In general, analytical expressions are not available for arbitrary values of the interaction parameter γ, defined by Eq. (1.5). However, in the limit of large and small γ the following asymptotic expressions are known [50]:

$$K(\gamma) = \begin{cases} 1 + \frac{4}{\gamma} & \text{for } \gamma \gg 1 \\ \frac{\pi}{\sqrt{\gamma}}\left(1 - \frac{\sqrt{\gamma}}{2\pi}\right)^{-1/2} & \text{for } \gamma \ll 1 \end{cases} \tag{1.26}$$

and

$$v_s(\gamma) = \begin{cases} v_F\left(1 - \frac{4}{\gamma}\right) & \text{for } \gamma \gg 1 \\ v_F\frac{\sqrt{\gamma}}{\pi}\left(1 - \frac{\sqrt{\gamma}}{2\pi}\right)^{1/2} & \text{for } \gamma \ll 1 \end{cases} \tag{1.27}$$

where $v_F = \hbar\pi n_0/m$ is the Fermi velocity of a Fermi gas with the same density. In the TG limit, due to the Bose-Fermi mapping (see Sec. 1.2), the compressibility of the Bose

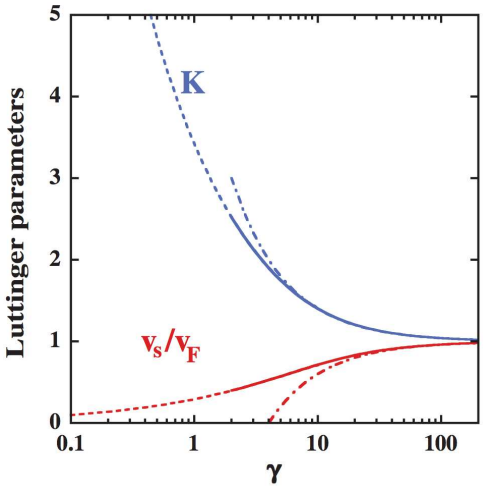

Figure 1.7: Luttinger parameter K and sound velocity v_s, in units of the Fermi velocity v_F, as a function of the dimensionless interaction strength γ. The dashed and dotted-dashed lines correspond to the asymptotic results given by Eqs. (1.26), and (1.27), the solid line corresponds to the numerical calculation from the Bethe ansatz equations. (Figure from Ref. [50]).

gas is identical to the one of the corresponding Fermi gas and the Luttinger parameter K approaches unity. In the same limit, the sound velocity is close to the Fermi velocity. In the weakly interacting limit, instead, the bosonic compressibility tends to zero and the Luttinger parameter K diverges, while phase fluctuations are small and the sound velocity is strongly suppressed. An important property to keep in mind is that the Luttinger parameter K for bosons with contact interactions is larger than or equal to one, and it decreases as the interactions become more repulsive.

The power of the LL approach goes beyond the simple description of the hydrodynamics of the system in terms of the quadratic Hamiltonian (1.25). Its peculiarity consists in the representation of the microscopic bosonic and density fields $\psi^\dagger(x)$ and $\rho(x)$, in terms of the phase and long wave-length density fluctuation ones $\phi(x)$ and $\Pi(x)$, via a systematic expansion taking into account fluctuations of any wave-vector. The density operator is defined in first quantized form as

$$\rho(x) = \sum_{j=1}^{N} \delta(x - x_j) \,, \tag{1.28}$$

where x_j is the position of the j-th particle. One can introduce a labelling field $\Theta(x)$ which takes the value $\Theta(x_j) = j\pi$ at the position x_j, and satisfies the topological property $\Theta(L) - \Theta(0) = \pi N$. Using $\delta[f(x)] = \delta(x - x_0)/|\partial_x f(x_0)|$, where $f(x_0) = 0$,

we can recast the density operator in the form

$$\rho(x) = \partial_x \Theta(x) \sum_{l=-\infty}^{+\infty} \delta(\Theta(x) - l\pi) \ . \tag{1.29}$$

Then applying Poisson's summation formula [2], one gets

$$\rho(x) = \frac{1}{\pi} \partial_x \Theta(x) \sum_{l=-\infty}^{+\infty} e^{i2l\Theta(x)} \ . \tag{1.30}$$

It is customary in the literature to work with the field

$$\theta(x) \equiv \Theta(x) - \pi n_0 x \ , \tag{1.31}$$

the density operator then reads

$$\rho(x) = \left(n_0 + \frac{1}{\pi} \partial_x \theta(x) \right) \sum_{l=-\infty}^{+\infty} e^{i2l(\theta(x) + \pi n_0 x)} \ . \tag{1.32}$$

Taking the spatial average of the density operator over distances larger than the mean interparticle distance $1/n_0$, all the oscillating terms vanish in the homogeneous system, and only the $l = 0$ leading contribution describing the long wave-length fluctuations with $|k| \ll n_0$ around the mean density n_0 remains $\rho(x) \simeq n_0 + \partial_x \theta(x)/\pi$, thus allowing us to identify $\Pi(x) \equiv \partial_x \theta(x)/\pi$. The $l \pm 1$ terms describe fluctuations with momenta $k \approx 2\pi n_0$, and $l \pm 2$ those with $k \approx 4\pi n_0$, etc. The single-particle creation field operator $\psi^\dagger(x)$ can be represented in terms of the Luttinger fields $\theta(x)$ and $\phi(x)$, through the density $\rho(x) = \psi^\dagger(x)\psi(x)$ and phase $\phi(x)$ representation

$$\psi^\dagger(x) = \sqrt{\rho(x)} e^{-i\phi(x)} \ . \tag{1.33}$$

In the case of bosonic particles, the single-particle operator $\psi^\dagger(x)$ satisfies the usual bosonic commutation rule $[\psi(x), \psi^\dagger(x')] = \delta(x - x')$, which translates into the commutation rule for the Luttinger fields $\theta(x)$ and $\phi(x)$:

$$\left[\partial_x \theta/\pi, \phi(x') \right] = i\delta(x - x') \ . \tag{1.34}$$

Recalling Fermi's trick $[\delta(\theta)]^2 = A\delta(\theta)$, where A is a non-universal constant that depends on the Dirac delta function representation, and thus on the way the high energy

[2] $\sum_{k=-\infty}^{+\infty} f(k) = \sum_{l=-\infty}^{+\infty} \int_{-\infty}^{+\infty} \mathrm{d}z f(z) e^{i2l\pi z}$.

fluctuations are cut-off, applying Poisson's summation formula, and finally multiplying by $e^{-i\phi(x)}$ from the right, one gets the final expression for the bosonic creation field operator

$$\psi^\dagger(x) \propto \sqrt{n_0 + \frac{1}{\pi}\partial_x\theta(x)} \sum_{l=-\infty}^{+\infty} e^{i2l(\theta(x)+\pi n_0 x)} e^{-i\phi(x)} \ . \tag{1.35}$$

Where the proportionality symbol indicates that this expression is valid only up to a cut-off dependent prefactor A.

The effective low-energy harmonic-fluid Hamiltonian (1.25) can be recast in terms of the gradients of the Luttinger fields $\theta(x)$ and $\phi(x)$, by recalling the representation of the long wave-length fluctuations of the density as $\Pi(x) \equiv \partial_x\theta(x)/\pi$

$$\mathcal{H}_{\rm LL} = \frac{\hbar v_s}{2\pi} \int_0^L \mathrm{d}x \ \left[K(\partial_x\phi(x))^2 + \frac{1}{K}(\partial_x\theta(x))^2 \right] \ . \tag{1.36}$$

To conclude this section on the LL low-energy effective field theory it is interesting to compare *a posteriori* the regime of validity of such a quadratic theory, that predicts a linear and gapless sound waves excitation spectrum, with the true excitation spectrum known from the exact solution of the Lieb-Liniger model, which is shown in Fig. 1.8. One can notice that the long wave-length fluctuations approximation, $|k| \ll n_0$, that has been done while deriving Hamiltonian (1.36), does not suffice to describe all the possible low-energy density fluctuations. It is therefore necessary to distinguish between low-energy and low-momenta. A 1D interacting Bose gas shows low-energy density excitations with momenta $\sim n_0$ or higher. Indeed, the energy spectrum of a system of N bosons of size L with periodic boundary conditions, shown in Fig. 1.8(a), has local minima at the so-called supercurrent states I ($I = 0, 1, 2, ...$) with $k_I = 2\pi n_0 I$, that lie on the parabola $\hbar^2 k^2/2mN$. These local minima are in correspondence with the so-called umklapp excitations, that correspond to excitations in which a momentum $\hbar 2\pi/L$, corresponding to the reciprocal wave vector of system, is imparted to each particle. These processes are taken into account through the higher harmonics, $l = \pm 1, \pm 2, ...$, in the Luttinger field expansions Eqs. (1.35) and (1.32). The position of these minima does not depend on interactions and their energy tends to zero in the thermodynamic limit, breaking superfluidity according to Landau's criterion [74].

In his seminal work [54], E. H. Lieb characterized the nature of the excitation spectrum of the 1D Bose gas identifying two types of possible excitations, that he labelled Type I and Type II, see Fig. 1.8(b). The Type I excitations are the so-called elementary excitations that correspond to Bogoliubov's excitation spectrum at weak interactions (yellow line in Fig. 1.8(a)), while Type II excitations are the lowest energy single particle-hole excitations (green line in Fig. 1.8(a)), that have no equivalent in Bogoli-

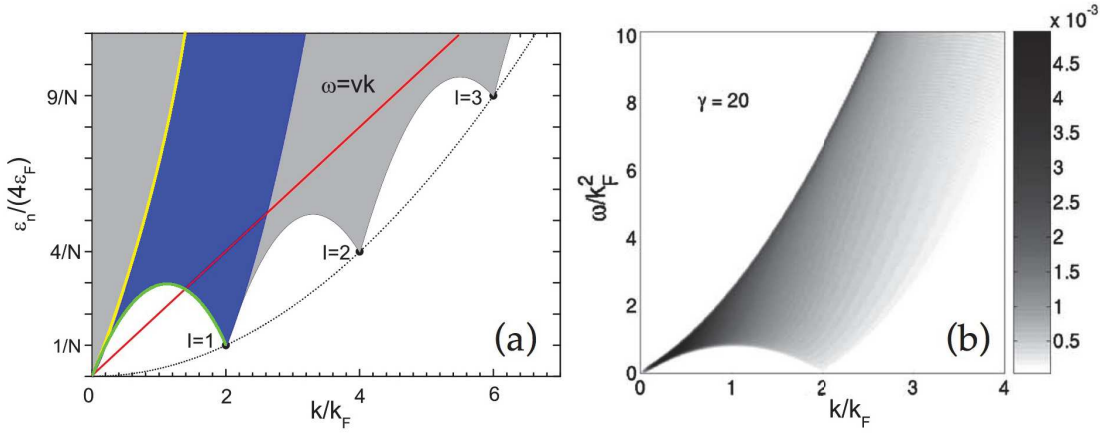

Figure 1.8: **(a)** Scheme of the energy domain of the excitation spectrum of the 1D Bose gas in a homogeneous system of size L, in units of $k_F = \hbar\pi n_0$ and $\varepsilon_F = \hbar^2 k_F^2/2m$. Excitations occur in the shaded area, the blue part corresponding to single particle-hole excitations. The discreteness on the spectrum is not shown for simplicity. The yellow line corresponds to Bogoliubov elementary excitations (Lieb Type I), and the green line to the lowest energy single particle-hole excitations (Lieb Type II). The transitions from the ground state caused by the motion of an obstacle with velocity v, lie on the red line $\omega = vk$. (Figure adapted from Ref. [75]). **(b)** Density plot of the zero-temperature dynamical structure factor $S(k,\omega)$, quantifying the probability of single particle excitations, obtained from Bethe ansatz for a 1D bosonic system at interaction strength $\gamma = 20$ quasi at the thermodynamic limit (Figure from Ref. [74]).

ubov's perturbative analysis. The validity of the LL harmonic fluid approach is thus restricted to the low-energy and low-momenta region of the spectrum, where Type I and Type II excitations dispersion relations coincide, approaching $k \to 0$ with a slope equal to the sound velocity $v_s(\gamma)$. The probability of excitation of such one-body processes by an infinitesimal external probe transferring momentum $\hbar k$ and energy $\hbar\omega$ to the system, can be quantified via the dynamical structure factor, which is the Fourier transform of the time-dependent density-density correlation function [41], $S(k,\omega) = \int \mathrm{d}t \int \mathrm{d}x\ e^{-ikx+i\omega t}\langle\rho(x,t)\rho(0,0)\rangle$. Its analytical calculation can be done for instance at strong interactions, via a perturbative approach starting from the TG solution [76], or, at low energy, via the LL approach starting from expression (1.32) for the density [77]. Its exact calculation, instead, has been done numerically via Bethe ansatz [74], an example of the result is shown in Fig. 1.8(b). A recent experimental measurement of the dynamical structure factor for a 1D Bose gas via Bragg spectroscopy has been reported *e.g.* in [78].

In the next chapters I will apply the LL effective field theory to the specific system considered. In particular, in Chap. 2 I will present how a mode expansion for the Luttinger fields, dependent on the system's boundary conditions, can be used to diago-

nalize Hamiltonian (1.36), and in Chap. 3. I will show how the present harmonic-fluid description can be extended to the case of an inhomogeneous system.

1.5 Exact diagonalization

The exact diagonalization method can be used to calculate the low-energy eigenspectrum and eigenfunctions of a time-independent Hamiltonian. This method is extremely general in its formalism, and not restricted to the case of 1D bosons to which it is applied in this thesis [79]. The starting point is the stationary Schrödinger equation

$$\mathcal{H}|\Psi\rangle = E|\Psi\rangle \ , \tag{1.37}$$

where $|\Psi\rangle$ is the many body state in Dirac representation. In order to solve this eigenvalue problem, one should chose an arbitrary basis of the Hilbert space $\{|n\rangle\}_{n=1,2,...}$, and project the stationary Schrödinger equation on the states $|n\rangle$

$$\langle n|\mathcal{H}\sum_{n'}|n'\rangle\langle n'|\Psi\rangle = E\langle n|\Psi\rangle \quad \forall n \ . \tag{1.38}$$

This set of equations can be written in matrix form, and the problem is therefore simply reduced to the diagonalization of the Hamiltonian matrix $\langle n|\mathcal{H}|n'\rangle_{n,n'=1,2,...}$.

The formalism of second quantization is particularly suitable in this context to represent the many-body state as a Fock state $|n_1, n_2, ...\rangle$, where n_α is the number of particles that occupy the α-th single-particle basis state. All the many-particle operators (one- and two-body) present in Hamiltonian (1.8) then can be expressed by means of creation and annihilation operators $a_\alpha^\dagger$ and a_α of a particle in a single-particle basis state [80], obeying the commutation relation $[a_\alpha, a_\beta^\dagger] = \delta_{\alpha,\beta}$. The kinetic and potential energy are one-body operators that are represented as

$$\sum_{j=1}^{N} -\frac{\hbar^2}{2m}\frac{\partial^2}{\partial x_j^2} + V_{\rm ext}(x_j) = \sum_{j=1}^{N} h_0^j = \sum_{\alpha,\beta}\langle\alpha|h_0|\beta\rangle a_\alpha^\dagger a_\beta \ ; \tag{1.39}$$

while the interaction energy is a two-body operator, that is represented as

$$\frac{g}{2}\sum_{i,j=1}^{N}\delta(x_i - x_j) = \sum_{i,j=1}^{N} h_{\rm int}^{i,j} = \sum_{\alpha,\beta,\gamma,\delta}\langle\alpha\beta|h_{\rm int}|\gamma\delta\rangle a_\alpha^\dagger a_\beta^\dagger a_\gamma a_\delta \ . \tag{1.40}$$

The matrix elements $\langle\alpha|h_0|\beta\rangle$ and $\langle\alpha\beta|h_{\rm int}|\gamma\delta\rangle$ are thus evaluated by means of the

wave functions of the single-particle basis $\varphi_\alpha = \langle x|\alpha\rangle$ as

$$\langle\alpha|h_0|\beta\rangle = \int \mathrm{d}x\ \varphi^*_\alpha(x)\left(-\frac{\hbar^2}{2m}\frac{\partial^2}{\partial x^2} + V_{\mathrm{ext}}(x)\right)\varphi_\beta(x)\ , \tag{1.41}$$

and

$$\langle\alpha\beta|h_{\mathrm{int}}|\gamma\delta\rangle = \frac{g}{2}\int \mathrm{d}x \int \mathrm{d}x'\ \varphi^*_\alpha(x)\varphi^*_\beta(x')\delta(x-x')\varphi_\gamma(x)\varphi_\delta(x')\ . \tag{1.42}$$

In Chap. 3 we have chosen, for instance, Wannier functions as a basis for the single particle states, relevant for the problem on a lattice considered there, that in such a way is mapped onto the Bose-Hubbard model, while in Chap. 4 we have chosen the Whittaker functions that diagonalize the one-body part of the Hamiltonian.

The diagonalization of the Hamiltonian matrix can be efficiently performed on a computer. However, the dimension of the Hilbert space is in general infinite, hence in the actual calculation one must restrict the basis $\{|n\rangle\}$ to a finite number, due to CPU and memory limitations. This truncation gives rise to a deviation between the exact and numerically obtained eigenenergies and eigenfunctions. Strictly speaking, the name exact diagonalization is thus improper, indicating simply the absence of any further approximation or assumption on the wave function. The accuracy of the result depends strongly on a 'good choice' of the basis functions and their number. The size D of the many-body Hilbert space for a bosonic gas is obtained through elementary combinatorics as the binomial

$$D = \binom{S+N-1}{N} = \frac{(N+S-1)!}{N!(S-1)!}\ , \tag{1.43}$$

where S is the number of single-particle states $|\alpha\rangle$ used to build the finite-size many-body basis $|n_1, n_2, ..., n_S\rangle$, and $N = \sum_{\alpha=1}^{S} n_\alpha$ is the total number of particles. We see that the size of the Hilbert space grows factorially with the system size, and thus only small systems can be tackled with this method. To improve the accuracy of the estimation of the eigenvalues a finite size scaling over different number of single-particle states can be performed, as in Chap. 4.

Résumé du chapitre

Méthodes theorique pour bosons unidimensionnels

Ce premier chapitre est consacré à une présentation générale des propriétés du gaz bosonique d'atomes ultrafroids en une dimension (1D), et des méthodes théoriques qui ont été employées pour l'étudier dans différents régimes physiques dans les chapitres suivants. En particulier, nous nous concentrons sur l'effet des interactions entre les particules. Un système unidimensionnel est realisé par un piège fortement confinant dans deux directions spatiales, ce qui limite le mouvement des atoms aux oscillations de point zero dans les deux directions transverse. Le gaz de Bose unidimensionnel présente des propriétés de cohérence très particulières à basse température, radicalement différentes de celles observées dans les systèmes de dimension supérieure. Une différence majeure est par exemple l'absence de condensation de Bose-Einstein dans un gaz 1D de bosons en interaction à la limite thermodynamique, tant à température finie qu'à température nulle. Plusieurs methodes, exactes et approchees, sont connues pour decrire des gaz de bosons unidimensionnels.

Dans ce chapitre je présente en particulier la solution exacte de Tonks-Girardeau, basée sur la correspondance de Bose-Fermi dans la limite des interactions infiniment fortes, l'équation de Gross-Pitaevskii basée sur une approximation de champ moyen valable dans le régime d'interactions faibles et d'un grand nombre de particules, la théorie effective du liquide de Luttinger valable pour interactions fortes lorsque les excitations de basse énergie sont des phonons, et la méthode numérique de diagonalisation exacte, applicable pour tous les valeurs des interactions mais seulement pour des systèmes de petite taille. Une autre méthode qui a été employée dans les projets de recherche présentés dans cette thèse est l'approche numérique de groupe de renormalisation de la matrice densité (DMRG), qui est une méthode variationnelle itérative basée sur une procédure de renormalisation.

Chapter 2

Persistent currents for interacting bosons on a ring

2.1 Introduction

In this chapter I present our study of persistent currents in a system of interacting one-dimensional bosons confined in a ring.

The persistent currents phenomenon is essentially a manifestation of the Aharonov-Bohm effect, that entails the influence of a gauge field on the quantum dynamics of charged particles in a multiply-connected geometry [82]. One of the most striking consequences of this effect in condensed matter physics occurs when one considers *e.g.* a mesoscopic metallic quantum ring threaded by a static magnetic field at low temperature. In this case, if the quantum phase coherence extends to the whole system and thermal fluctuations do not wash it out, the Aharonov-Bohm effect shows up at the many-body level as a dissipationless equilibrium current flowing through the system even in the absence of any applied voltage [83, 84]. The theoretical and experimental investigation of this counterintuitive phenomenon of an electric current that flows without dissipating energy in a normally resistive medium has attracted in the last 50 years an enormous attention. Persistent currents were first observed in solid state electronic systems subjected to a magnetic field: first in bulk superconductors [85], and more recently, overcoming the challenges of decoherence induced by inelastic scattering also in normal metallic rings [86–88]. The measurement of persistent current in such electronic systems is in general very challenging because of its small signal (typically of the order of ~ 1 nA) and its high sensitivity to the electromagnetic environment and to the effect of microscopic disorder present in the material [88].

The most recent development in the manipulation of ultracold atomic gases has

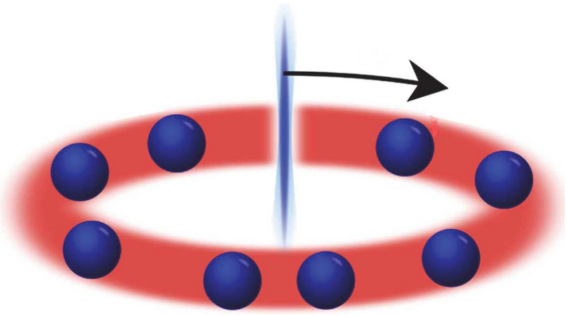

Figure 2.1: Sketch of atoms confined in a tight ring trap realized by an attractive (red-detuned) laser beam with a rotating barrier realized by a repulsive (blue-detuned) one. (Figure adapted from Ref. [81]).

led to the realization of micrometric ring traps [89–95], disclosing a novel platform for the study of the persistent currents phenomenon. Ultracold gases are model quantum fluids characterized by long-range coherence properties, that compared to their electronic counterparts are extremely tunable and clean. Experimentally it is possible to adjust at will the dimensionality, the geometry of the confining potential, and even the strength of the interactions, thus giving rise to a very versatile platform for the quantum simulation of many quantum phenomena [12,14], including that of the persistent currents. Because of the charge neutrality of the atoms that constitute the quantum gas it is not possible to induce a persistent current by means of a magnetic field, as for the electronic systems. However, thanks to the formal equivalence between the Lorentz force acting on charged particles in a magnetic field and the Coriolis force acting on particles under rotation, it is possible to generate for the neutral atoms a rotational phase analogous to the vector potential one for charged particles, thus applying an artificial gauge field. This idea has been applied in several experiments, in which a Bose-Einstein condensate of ultracold atoms confined on a ring trap has been set into motion by stirring it with a well-focused repulsive (blue-detuned) laser beam that acts as a sort of optical paddle, see the sketch in Fig. 2.1. In this way persistent flows with quantized circulation have been induced, and precise control both in inducing and arresting the particles flow has been demonstrated [96–98]. The state of circulation of the system can be tested via time-of-flight expansions measurements [94, 95], that allow to access the momentum distribution of the gas, or directly by interferometric measurements, as has been recently proposed in [99, 100]. This rapid experimental progress of the last years has motivated an intense investigation of such systems. On the fundamental side a lot of effort has been devoted to the study of the superfluid properties and decay mechanisms of such currents once the stirring is arrested: long-lived metastable superflows with lifetimes up to 40 s have been observed [94], and

the nucleation of vortices has been identified as one of the fundamental mechanisms leading to phase slips and current decay [101]. On the application side such systems are regarded with more and more attention as the best candidates for the realization of high-precision gyroscopes based on matter-wave interferometry [102], superpositions of current states and flux qubits (see Chap. 3) [81, 103–106].

The scenario becomes particularly intriguing if the transverse section of the ring is sufficiently thin to effectively confine the system to 1D. In this case the rich interplay between interactions, quantum fluctuations and the presence of a stirring potential barrier, whose effects are all enhanced in 1D, acquires a role of primary relevance. In this context we have provided a complete characterization of the persistent currents for 1D bosons, studying its amplitude and scaling properties with the system size in all the interaction and barrier strength regimes.

2.2 Persistent currents for bosons on a ring

We consider a system of N bosons of mass m, interacting with each other via the contact potential $V(x-x') = g\,\delta(x-x')$, and confined in a 1D ring of circumference L. The ring contains a localized barrier, modelled as a delta function $U_b(x,t) = U_0\delta(x-vt)$, rotating along its circumference at constant tangential velocity v. We consider the stationary regime, at zero temperature, reached after the barrier has been adiabatically switched on and set into motion at early times, such that no high-energy excitations are produced. The rotation induces an effective $U(1)$ gauge field for the neutral atoms [107], with a Coriolis flux $\Omega = mvL/2\pi\hbar$ threading the ring. The same artificial gauge field could also be applied in a non-rotating system by imparting a geometric phase directly to the atoms via suitably designed laser fields [108–110]. The corresponding system's Hamiltonian, in the rotating frame, reads

$$\mathcal{H} = \sum_{j=1}^{N} \frac{\hbar^2}{2m}\left(-i\frac{\partial}{\partial x_j} - \frac{2\pi}{L}\Omega\right)^2 + U_0\delta(x_j) + \frac{g}{2}\sum_{j,l=1}^{N}\delta(x_j - x_l)\ , \tag{2.1}$$

where $x_j \in [0, L]$ is the j-th particle coordinate along the ring circumference. This generalizes the Lieb-Liniger model to the rotating case and is non-integrable due to the presence of the barrier external potential.

In the absence of the barrier ($U_0 = 0$), the system is rotationally invariant, and the total linear momentum $P = -i\hbar\sum_{l=1}^{N}\partial_{x_l}$ along the circumference, and the total angular momentum $\mathcal{L}_{\hat{z}} = PL/2\pi$, commute with Hamiltonian (2.1), their eigenvalues being good quantum numbers. The wave function for the system confined in the ring has to fulfil periodic boundary conditions (PBC) for each particle $l = 1, ..., N$, *i.e.*

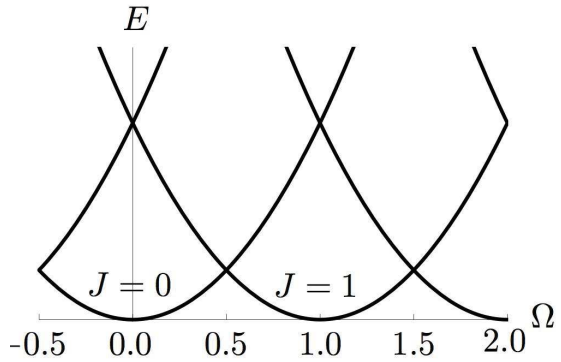

Figure 2.2: Scheme of the energy spectrum for bosons on a ring under the influence of an artificial gauge field with Coriolis flux Ω. The periodically repeated parabolas correspond to states with well-defined circulation J and total angular momentum $JN\hbar$.

$\Psi(x_1, ..., x_l, ..., x_N) = \Psi(x_1, ..., x_l+L, ..., x_N)$. The many-body wave function in general can be written as a linear combination of products of single-particle wave functions $\psi_j(x)$, with j a quantum number, as $\Psi(x_1, ..., x_N) = \sum_{\{j_1,...,j_N\}} c_{\{j_1,...,j_N\}} \prod_{l=1}^{N} \psi_{j_l}(x_l)$, and then the single-particle wave functions must also fulfil PBC, $\psi_j(x) = \psi_j(x + L)$. Applying Bloch theorem for the case of a homogeneous ring we have that the single-particle wave functions are plane waves $\psi_j(x) = (1/\sqrt{L}) \exp(ik_j x)$ with single particle energy $\varepsilon_j = \hbar^2 k_j^2/2m$, and wave vectors quantized by the periodicity condition, $k_j = 2\pi j/L$ for j integer. The periodic boundary conditions of the ring thus quantize the linear momentum in units of $2\pi\hbar/L$, and provide a natural energy unit for this system, that is the smallest non-zero kinetic energy of a single particle

$$E_0 = \frac{2\pi^2\hbar^2}{mL^2} \ . \tag{2.2}$$

From the commutation of the total linear momentum P with the Hamiltonian, the many-body wave function can be written, separating the degree of freedom of the center of mass $x_{\rm cm} = \sum_{l=1}^{N} x_l/N$, in the form

$$\Psi(x_1, ..., x_N) = e^{iPx_{\rm cm}/\hbar} \chi_P(x_1, ..., x_N) \ , \tag{2.3}$$

where the "intrinsic" wave function $\chi_P(x_1, ..., x_N)$ is a linear combination of products of single-particle wave functions $\chi_P(x_1, ..., x_N) = \sum_{\{j_1,...,j_N\}} c_{\{j_1,...,j_N\}} \prod_{l=1}^{N} \psi_{j_l}(\zeta_l)$, with $\zeta_l = x_l - x_{\rm cm}$, and such that $P/\hbar = \sum_{l=1}^{N} k_{j_l}$. Applying the Bloch unitary transformation $\mathcal{U} = \exp(i2\pi\Omega x/L)$, the Ω-dependence is removed from the Hamiltonian, and the PBC of the wave function translates into twisted boundary conditions (TBC), $\psi_j(x) = e^{i2\pi\Omega}\psi_j(x + L)$. This means that a phase factor proportional to the Coriolis

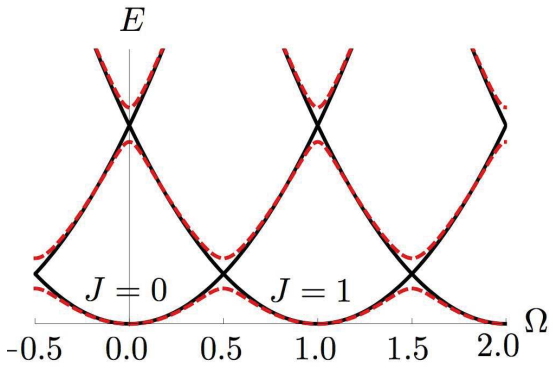

Figure 2.3: Scheme of the energy spectrum for bosons on a ring under the influence of an artificial gauge field with Coriolis flux Ω. The black-solid line corresponds to the case in the absence of the barrier ($U_0 = 0$), and the red-dashed line to the the case in the presence of a finite barrier ($U_0 > 0$) that opens gaps in the spectrum.

flux is added to the wave function after a full loop around the ring, giving rise to the Aharonov-Bohm effect [82]. The wave function given by Eq. (2.3) then takes the form

$$\Psi(x_1, ..., x_N) = e^{i(P/\hbar - \Omega 2\pi n_0)x_{\rm cm}} \chi_P(x_1, ..., x_N) \ , \tag{2.4}$$

where $n_0 = N/L$, and the intrinsic wave function $\chi_P(x_1, ..., x_N)$ is left unchanged by this unitary transformation. The many-body ground state energy as a function of the Coriolis flux Ω is thus given by

$$E(\Omega, J) = NE_0(J - \Omega)^2 + E_{int} \ , \tag{2.5}$$

where $J = P/2\pi\hbar n_0$, and E_{int} is the Ω-independent interaction energy. These are parabolas, corresponding to states with well defined circulation J and corresponding total angular momentum $JN\hbar$, periodically shifted by a Galilean transformation in Ω with period 1, and intersecting at the so-called frustration points at half-integer values of the flux (see Fig. 2.2) [111, 112]. Given the periodicity of the spectrum, in the following we will always restrict to the first rotational Brillouin zone $\Omega \in [0, 1]$.

The presence of a finite barrier ($U_0 > 0$) breaks the rotational symmetry of the system, and, coupling states with different circulation J, opens gaps in the spectrum that lift the degeneracy in correspondence of the crossing between parabolas (see Fig. 2.3). As I will present in detail in Chap. 3, this forms the working point for a qubit based on a superposition of current states. The shape of the energy bands in the presence of a barrier, and the size of the gaps at the frustration points depend in general on the barrier potential strength and on the interaction strength between the particles.

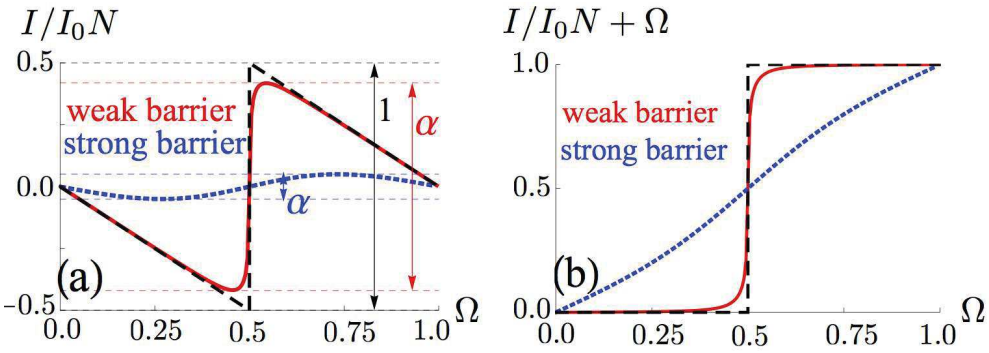

Figure 2.4: Scheme of the persistent currents in the first rotational Brillouin zone **(a)** in the rotating frame and **(b)** in the non-rotating frame, in units of $NI_0 = 2\pi\hbar N/mL^2$ for zero barrier (black-dashed line), weak barrier (red-solid line) and strong barrier (blue dotted line) at fixed interaction strength.

From the previous considerations on the spectrum of the system, we have that the ground state of the system in the presence of Coriolis flux can carry a non-zero circulation. An interesting quantity to study is therefore the particle current flowing in the ring. Both in the context of cold atoms confined in ring traps under rotation and in the analogous one of electronic systems in circuits threaded by magnetic fields, the current induced by a gauge flux as a consequence of the Aharonov-Bohm effect is usually referred to in the literature as persistent current. At zero temperature, the spatially averaged particle current $I(\Omega)$, or persistent current, is obtained from the ground state energy $E(\Omega)$ via the thermodynamic relation [113]:

$$I(\Omega) = -\frac{1}{2\pi\hbar}\frac{\partial E(\Omega)}{\partial \Omega} \,. \tag{2.6}$$

The current calculated in this way corresponds to the one in the co-rotating frame. The current in the non-rotating frame, can be obtained performing a Galilean boost

$$I_{nr}(\Omega) = I(\Omega) + n_0 v = I(\Omega) + \frac{2\pi\hbar N}{mL^2}\Omega \,. \tag{2.7}$$

Applying the Hellmann-Feynman theorem[1] it is easy to see that the current calculated in this way corresponds to the spatially averaged particle current $I_{nr}(\Omega) = \frac{1}{L}\int_0^L \mathrm{d}x \;\; j(x,\Omega)$, where the current density is given by the usual expectation value of the momentum operator $j(x,\Omega) = (1/m)\langle\Psi(\Omega)|\sum_{l=1}^{N} -i\hbar\partial_{x_l}|\Psi(\Omega)\rangle$.

In the absence of the barrier, the current corresponding to the periodic parabolic ground state energy of Eq. (2.5) is given, for any interaction regime, in the rotating frame by a sawtooth [114, 115], and in the non-rotating frame by a staircase function,

[1] $\frac{\mathrm{d}}{\mathrm{d}\Omega}E(\Omega) = \langle\Psi(\Omega)|\frac{\mathrm{d}}{\mathrm{d}\Omega}\mathcal{H}(\Omega)|\Psi(\Omega)\rangle/\langle\Psi(\Omega)|\Psi(\Omega)\rangle$.

with plateaus corresponding to states with well defined circulation, see Fig. 2.4. In absence of any barrier, the sawtooth current attains its maximal amplitude NI_0, with

$$I_0 = \frac{E_0}{\pi\hbar} = \frac{2\pi\hbar}{mL^2} \,. \tag{2.8}$$

A diamagnetic or paramagnetic response depending on the population parity is expected for fermions but not for bosons [84,116]. The presence of a level mixing barrier, that gives rise to gap openings at the frustration points in the spectrum, is visible also in the current. For a weak barrier, that opens a small gap in the spectrum, the current becomes a smeared sawtooth and a smeared staircase in the rotating and non-rotating frame respectively (see Fig. 2.4). For a large barrier that opens a large gap, or small-tunnelling limit, the current acquires a modulated-linear and sinusoidal behaviour respectively (see Fig. 2.4), as obtained for thin superconducting rings from a Luttinger-liquid approach [117]. Beyond these limiting regimes the physics of bosonic persistent current was unexplored before our work.

2.3 Optimal amplitude of persistent currents

In this section I present a complete characterization of persistent currents for 1D bosons, focusing on the amplitude α of the persistent current in the rotating frame

$$\alpha = \frac{I_{\max} - I_{\min}}{NI_0} \,, \tag{2.9}$$

and determining its value in all the regimes of interaction and barrier strength. The results presented in this section are part of the original work of my PhD and are summarized in the first publication [16]. This work has been the result of a collaboration of our group with Davide Rossini [2], and Matteo Rizzi [3]. Below in this section, I provide primarily details on our results, and on the methods I have implemented myself. For further details on the DMRG technique, that was implemented by our collaborators, I refer to the publication [16] and to the references therein.

By combining analytical as well as numerical techniques suited for the 1D problem, we have found that the current amplitude is a non-monotonic function of the interaction strength and displays a pronounced maximum at intermediate interaction in all regimes of barrier height, see Fig. 2.5. The presence of an optimal regime of maximal current amplitude illustrates the highly non trivial combination of correlations, quantum fluctuations and barrier effects.

[2] NEST, Scuola Normale Superiore and Istituto Nanoscienze-CNR, I-56126 Pisa, Italy.
[3] Institut für Physik, Johannes Gutenberg-Universität, Staudingerweg 7, D-55099 Mainz, Germany.

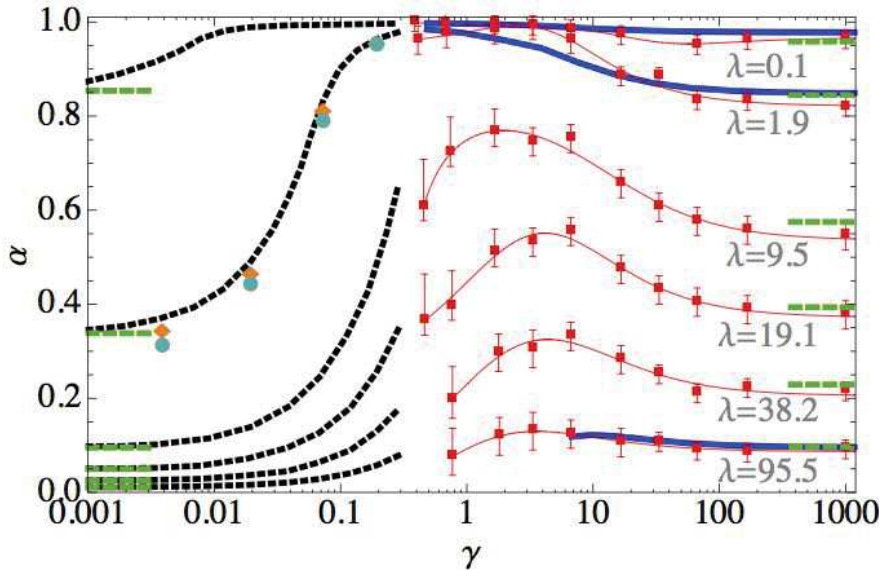

Figure 2.5: Persistent current amplitude α, in units of $NI_0 = 2\pi\hbar N/mL^2$, as a function of the interaction strength γ at varying dimensionless barrier strength $\lambda = mU_0L/\pi\hbar^2$, for $N = 18$, from Gross-Pitaevskii equation (black dotted lines), Luttinger liquid approach (blue solid lines), numerical DMRG calculations (red squares, red thin lines are guides to the eye) and non-interacting and Tonks-Girardeau exact solutions (green dashes). Orange diamonds and cyan circles are for a Gaussian barrier of width $\sigma = 0.5, 2\, n_0^{-1}$ respectively.

2.3.1 Non-interacting and impenetrable boson limits

Both for zero and infinitely large repulsive interactions, it is possible to find an exact solution to the many-body Schrödinger equation $\mathcal{H}\Psi(x_1, \dots x_N) = E\Psi(x_1, \dots x_N)$. For a non-interacting (NI) Bose gas, the many-body wave function

$$\Psi_{\rm NI}(x_1, \dots x_N) = \prod_{i=1}^{N} \psi_0(x_i) \tag{2.10}$$

is simply given by the product of N identical single-particle wave functions $\psi_0(x_i)$, which are ground-state solutions of the corresponding one-body Schrödinger equation

$$\frac{\hbar^2}{2m}\left(-i\frac{\partial}{\partial x} - \frac{2\pi}{L}\Omega\right)^2 \psi_n + U_0\delta(x)\psi_n = \varepsilon_n\psi_n \,, \tag{2.11}$$

and has energy $E_{\rm NI} = N\varepsilon_0$.

In the infinitely interacting limit of impenetrable bosons, or Tonks-Girardeau (TG) gas, the solution is obtained by mapping the system onto a gas of non-interacting

fermions subjected to the same external potential (see Sec. 1.2 for details)

$$\Psi_{\rm TG}(x_1,\dots x_N)=\prod_{1\le j<\ell\le N}\mathrm{sgn}(x_j-x_\ell)\det[\psi_k(x_i)]\ . \tag{2.12}$$

The corresponding energy $E_{\rm TG}=\sum_{k=0}^{N-1}\varepsilon_k$ and density profile $n(x)=\sum_{k=0}^{N-1}|\psi_k|^2$ directly reflect the fermionization properties of the strongly interacting Bose gas. The Friedel-like oscillations of the density profile, shown in Fig. 2.6, are indeed a signature of the strongly correlated regime [118].

The persistent current amplitude in the zero and infinitely interacting limits is then obtained from Eq. (2.6). We need thus to solve the one-body Schrödinger equation (2.11) to compute the ground state energy in the two cases. The single particle eigenfunctions take the form

$$\psi_n(x;\Omega)=\begin{cases}\frac{1}{\mathcal{N}_n}\,e^{-i\Omega\pi}\left[e^{ik_n(x-L/2)}+A_{n,\Omega}e^{-ik_n(x-L/2)}\right] & x\in[0,L/2)\\ \frac{1}{\mathcal{N}_n}\,e^{i\Omega\pi}\left[e^{ik_n(x+L/2)}+A_{n,\Omega}e^{-ik_n(x+L/2)}\right] & x\in[-L/2,0)\end{cases} \tag{2.13}$$

that satisfy the twisted boundary conditions $\psi_n(-L/2;\Omega)=e^{i2\pi\Omega}\psi_n(L/2;\Omega)$. By imposing unity normalization, and the cusp condition at the position of the barrier $\partial_x\psi_n^+(0^+;\Omega)-\partial_x\psi_n^-(0^-;\Omega)=\lambda\psi_n(0;\Omega)$, where $\lambda=mU_0L/\pi\hbar^2$ is the dimensionless barrier strength, we obtain the transcendental equation for the wave vectors

$$k_n=\pm\lambda\frac{\pi}{L}\frac{\sin(k_nL)}{\cos(2\pi\Omega)\mp\cos(k_nL)}\,, \tag{2.14}$$

where the $\pm$ sign refers to a number of particles N odd or even respectively. This follows from the fact that the mapping function $\mathcal{A}=\Pi_{1\le j<\ell\le N}\mathrm{sgn}(x_j-x_\ell)$ used to build the TG wavefunction $\Psi_{\rm TG}(x_1,\dots x_N)=\mathcal{A}\det[\psi_k(x_i)]$ is periodic (antiperiodic) for odd (even) N respectively; correspondingly, the single-particle orbitals need to be periodic (antiperiodic) for odd (even) N [53,58]. The coefficients entering in Eq. (2.13) are $A_{n,\Omega}=\frac{\sin(k_nL/2+\Omega\pi)}{\sin(k_nL/2-\Omega\pi)}$ for N odd and $A_{n,\Omega}=-\frac{\cos(k_nL/2+\Omega\pi)}{\cos(k_nL/2-\Omega\pi)}$ for N even, while $\mathcal{N}_n=\sqrt{L\Big(1+A_{n,\Omega}^2+2A_{n,\Omega}\frac{\sin(k_nL)}{k_nL}\Big)}$ is the normalization factor. The single particle energies are then given by

$$\varepsilon_n=\frac{k_n^2\hbar^2}{2m}\,, \tag{2.15}$$

and allow us to compute the many-body ground state energy and the current.

In the weak barrier limit $\lambda\ll 1$ we determined also perturbatively the persistent current amplitude. The single-particle energy levels $\varepsilon_n^{(\pm)}$ are obtained by degenerate perturbation theory around the unperturbed parabolas $\epsilon_n=\frac{(2\pi\hbar)^2}{2mL^2}(\Omega-n)^2$, where we

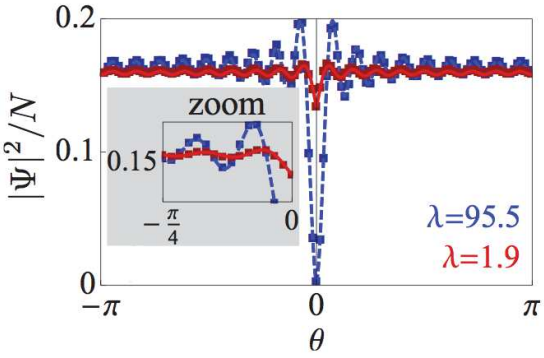

Figure 2.6: Normalized density *vs.* angular coordinate θ along the ring for the values of the dimensionless barrier strength λ specified in the figure and $N = 18$, $\Omega = 0.4$. The lines correspond to the analytical TG solution, the squares to the numerical DMRG results in the same parameter regime, the zoom showing the excellent agreement between the two. The density displays a Friedel-like oscillatory modulation induced by the presence of the barrier that is typical of fermionic systems [118]. A study of its dependence on the rotation velocity is reported in [119].

have chosen N odd for simplicity [4]. Close to the frustration point $\Omega = 1/2$ the pairs of degenerate levels are ϵ_n and ϵ_{1-n}, and we immediately get

$$\varepsilon_n^{(\pm)} = \frac{(2\pi\hbar)^2}{2mL^2}\left\{[\delta\Omega^2 + (n-1/2)^2] \pm 2(n-1/2)\sqrt{\delta\Omega^2 + \tilde{\lambda}_n^2}\right\} \tag{2.16}$$

where $\delta\Omega = \Omega - 1/2$ and $\tilde{\lambda}_n = \lambda/(2n-1)$. The TG ground-state energy is thus given by $E_{\rm TG} = \sum_{n=0}^{(N-3)/2}(\varepsilon_n^{(+)} + \varepsilon_n^{(-)}) + \varepsilon_{(N-1)/2}^{(-)}$. In this sum the $\pm$ terms in the right hand side of Eq. (2.16) compensate except the highest-energy one, as is typical in fermionic systems, where only the highest occupied level determines the transport properties. This yields the analytical expression for the persistent current

$$I(\Omega) = -NI_0\,\delta\Omega\left[1 - \left(\sqrt{4\delta\Omega^2 + \lambda_{\rm eff}^2/\pi^2}\right)^{-1}\right], \tag{2.17}$$

with $\lambda_{\rm eff} = \lambda/N$. As we shall see in Sec. 2.3.3, comparing this expression with the result of the Luttinger liquid theory, allows us to choose the short-distance cutoff of the Luttinger theory.

The persistent current amplitude α in the zero and infinitely interacting limits, obtained in this way, is shown in Fig. 2.5. We find that the current amplitude depends on the interaction regime. In particular, for all values of barrier strength, α is always

[4] In the case of N even one should consider antiperiodic boundary conditions [53, 58], that lead to a $1/2$ shift in Ω of the single-particle spectrum, and thus to the same final expression for the current, Eq (2.17).

larger in the strongly interacting regime than in the non-interacting one. This behaviour is due to the fact that the barrier affects in proportion more the lower-energy NI system than the higher-energy TG one. As a result, the current amplitude is smaller for non-interacting bosons, occupying only the lowest level, than for the TG gas, where the levels are filled up to the Fermi energy.

2.3.2 Weak interactions

In order to explore the role of interactions, we start from the non-interacting result and consider the effect of weakly repulsive interactions. In this regime we neglect quantum fluctuations and describe the system making use of the mean-field Gross-Pitaevskii (GP) equation, see Sec 1.3 for details. In the co-rotating frame, this takes the form

$$\frac{\hbar^2}{2m}\left(-i\frac{\partial}{\partial x}-\frac{2\pi}{L}\Omega\right)^2\Phi+U_0\delta(x)\Phi+g|\Phi|^2\Phi=\mu\Phi\ , \tag{2.18}$$

where Φ is the condensate wave function and μ the chemical potential. We have found an analytical dark-soliton solution for Φ in terms of Jacobi elliptic functions, thus extending Refs. [120,121] to the presence of a barrier potential. The details of the derivation are presented in App. A, and the final expressions for the density and phase are given by Eqs. (A.5), (A.11). The resulting density profile has a minimum pinned at the barrier position, whose depth and healing length depend on the interaction strength, the barrier height, and the rotation velocity, see Fig. 2.7(a-d). The solitary suppression of the density is accompanied by a winding of the phase, known as a phase-slip, see the insets of Fig. 2.7(a-d).

The soliton energy is obtained from the GP energy functional

$$E_{\rm GP}[\Phi]=\int_0^L \mathrm{d}x\ \Phi^*\frac{\hbar^2}{2m}\left(-i\frac{\partial}{\partial x}-\frac{2\pi}{L}\Omega\right)^2\Phi+\frac{g}{2}|\Phi|^4+U_0\delta(x)|\Phi|^2\ , \tag{2.19}$$

which encodes the dependence on Ω also in the condensate wave function. Computing then the persistent current amplitude α through Eq. (2.6) we find that it increases monotonically with the interaction strength γ, as illustrated in Fig. 2.5. This is due to the fact that the healing length $\xi=\hbar/\sqrt{2mgn_0}$, decreases at increasing interaction strength, as is visible also in the density profile (see Fig. 2.7(b)), thus yielding a more effective screening of the barrier.

By performing imaginary-time numerical integration of the GP equation, we have checked that the analytical soliton solution given by Eqs. (A.5), (A.11) coincides with the numerical ground state, see the excellent agreement in Fig. 2.7(e). Via the imaginary-time integration technique, we have also considered the case of a finite-width Gaus-

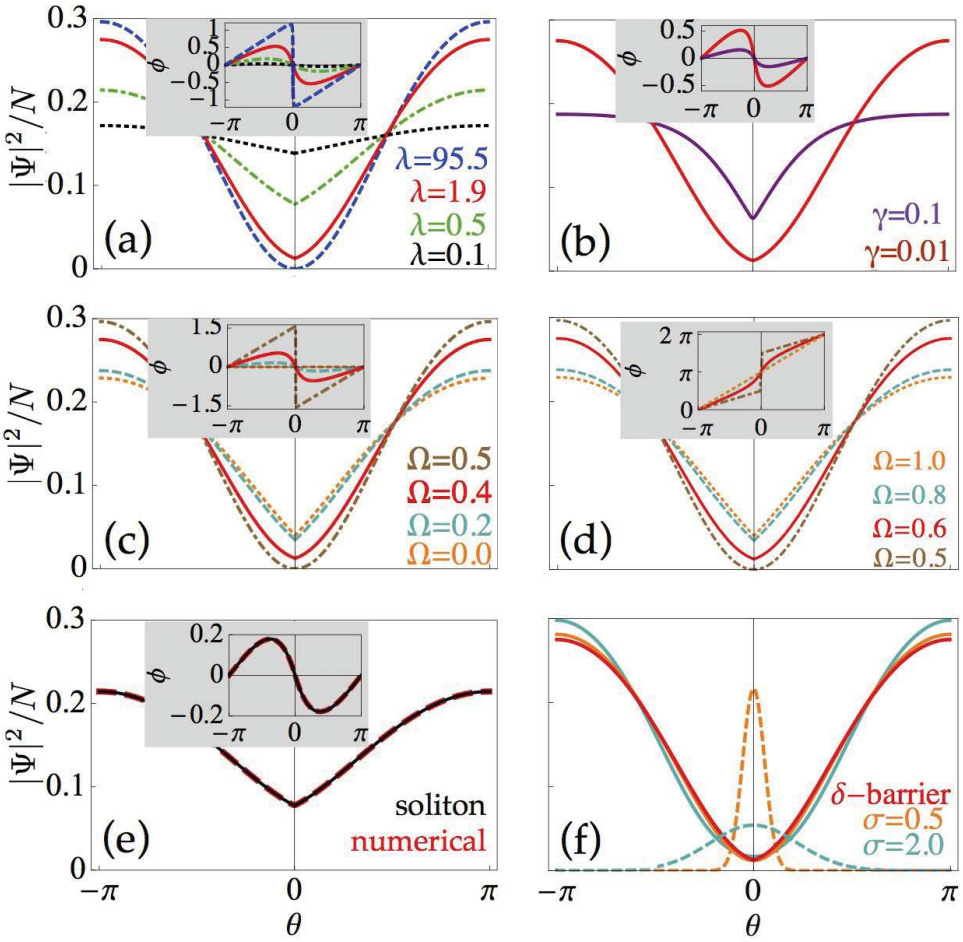

Figure 2.7: **(a)** GP soliton solution for the density (main figure) and phase (inset) as a function of the angular coordinate θ along the ring, for various values of the dimensionless barrier strength λ, as indicated in the figure, at fixed $\Omega = 0.4$, $N = 18$ and $\gamma = 0.01$. **(b)** GP soliton solution for various values of the interaction strength γ, at fixed $\Omega = 0.4$, $N = 18$ and $\lambda = 1.9$. **(c, d)** GP soliton solution for various values of the Coriolis flux Ω , at fixed $\lambda = 1.9$, $N = 18$ and $\gamma = 0.01$. **(e)** Comparison of the analytical GP soliton solution (black solid line) with the imaginary-time numerical solution (red dashed line) for $N = 18$, $\Omega = 0.4$, $\lambda = 0.5$, and $\gamma = 0.01$. The corresponding numerical ground state energy is $E_{\rm num}/E_0 = 0.2965(3)$ to be compared with the soliton solution one $E_{\rm sol}/E_0 = 0.2966$. **(f)** GP numerical solution (solid lines) at $\gamma = 0.01$ for a Gaussian barrier of strength $\lambda = 1.9$, for various values of the barrier width σ (in units of n_0^{-1}), and corresponding barrier potential (dashed lines, in units of $10E_0$).

sian barrier, as could be realized experimentally, finding results which are very similar to the case of localized barrier, as long as the barrier width does not exceed the mean interparticle distance $\sigma \lesssim n_0^{-1}$. This is a realistic condition, achievable *e.g.*, with a microscope-focused stirring beam [122], see Figs. 2.7(f), and 2.5.

2.3.3 Strong interactions

For strong interparticle interactions the effect of quantum fluctuations on the persistent current cannot be neglected as in the mean-field Gross-Pitaevskii theory. To cover this regime we apply the Luttinger liquid (LL) theory. As introduced in Sec. 1.4, this is a low-energy, quantum hydrodynamics description of the bosonic fluid, in terms of the canonically conjugate fields θ and ϕ corresponding to density fluctuations and phase respectively.

In the rotating frame, the effective LL Hamiltonian for a uniform ring is

$$\mathcal{H}_0 = \frac{\hbar v_s}{2\pi}\int_0^L \mathrm{d}x \left[K\Big(\partial_x\phi(x) - \frac{2\pi}{L}\Omega\Big)^2 + \frac{1}{K}(\partial_x\theta(x))^2\right]. \tag{2.20}$$

The microscopic interaction strength enters through the Luttinger parameter K and the sound velocity v_s. In the case of repulsive contact interactions their dependence on the interaction strength is known (see Eqs. (1.26), (1.27) and Fig. 1.7): at vanishing interactions, K tends to infinity and v_s vanishes, while, in the TG limit, $K = 1$ and v_s corresponds to the Fermi velocity of the fermionized Bose gas.

In the presence of a barrier, the nonlinear term

$$\mathcal{H}_\mathrm{b} = \int_0^L \mathrm{d}x\, U_0\delta(x)\rho(x) \tag{2.21}$$

is added to the Hamiltonian (2.20). We treat this term perturbatively in the limits of weak and strong barrier strength. The problem of the transmission of a 1D quantum fluid through a potential barrier has been widely studied in condensed matter physics, through LL renormalization group approaches. Some remarkable results in the context of electronic systems are for instance summarized in [123, 124].

Weak barrier – In the weak barrier case, we start from the mode expansion for the Luttinger fields θ and ϕ that diagonalize the Hamiltonian $\mathcal{H}_0$ for a uniform ring with periodic boundary conditions [49, 50]

$$\theta(x) = \theta_0 + \frac{1}{2}\sum_{q\neq 0}\left|\frac{2\pi K}{qL}\right|^{1/2}[e^{iqx}b_q + e^{-iqx}b_q^\dagger], \tag{2.22}$$

$$\phi(x) = \phi_0 + \frac{2\pi x}{L}(J-\Omega) + \frac{1}{2}\sum_{q\neq 0}\left|\frac{2\pi}{qLK}\right|^{1/2}\mathrm{sgn}(q)[e^{iqx}b_q + e^{-iqx}b_q^\dagger], \tag{2.23}$$

where $q = 2\pi j/L$ with j integer, J is the angular momentum operator and the following commutation relations hold: $[b_q, b_{q'}^\dagger] = \delta_{q,q'}$, and $[J, e^{-i2\theta_0}] = e^{-i2\theta_0}$. The latter

property implies that the zero-mode θ_0 acts as a raising operator for the states $|J\rangle$ of given angular momentum: $e^{-i2\theta_0}|J\rangle = |J+1\rangle$. The effect of the rotation has been reabsorbed in the definition of the phase field going from periodic to twisted boundary conditions, and appears explicitly in the mode expansion for the phase. Inserting Eqs. (2.22) and (2.23) in the Hamiltonian (2.20) we obtain

$$\mathcal{H}_0 = E_0(J-\Omega)^2 + \hbar v_s \sum_q |q| \left(b_q^\dagger b_q + \frac{1}{2} \right) , \tag{2.24}$$

where E_0 is given by Eq. (2.2), and we have used the relation $v_s K = \hbar\pi n_0/m$ between the Luttinger parameters, see Sec. 1.4 for details.

In the weak barrier regime the contribution of the barrier part of the Hamiltonian, Eq. (2.21), can be treated as a perturbation and is obtained by keeping only the lowest harmonics in the density field expansion $\rho(x) = (n_0+\partial_x\theta(x)/\pi)\sum_{l=-\infty}^{+\infty} e^{i2l\theta(x)+i2l\pi n_0 x}$, see Eq. (1.32), which then reads

$$\rho(x) \simeq (n_0 + \partial_x\theta(x)/\pi)\left\{1 + 2\cos\left[2\theta(x) + 2\pi n_0 x\right]\right\} . \tag{2.25}$$

Correspondingly, the barrier term (2.21) in the Hamiltonian reads

$$\mathcal{H}_\mathrm{b} \simeq U_0(n_0 + \partial_x\theta(0)/\pi)\left\{1 + 2\cos\left[2\theta(0)\right]\right\} . \tag{2.26}$$

The backscattering term $2U_0 n_0 \cos[2\theta(0)]$ breaks angular momentum conservation inducing transitions of one quantum of angular momentum due to the zero-mode part in $\theta(x) \equiv \theta_0 + \delta\theta(x)$. Using $e^{-i2\theta_0} = \sum_J |J+1\rangle\langle J|$ we obtain thus

$$\mathcal{H}_\mathrm{b} \simeq \frac{U_0}{\pi}\partial_x\theta(0) + n_0 U_0 \sum_J |J-1\rangle\langle J| e^{i2\delta\theta(0)} + |J\rangle\langle J+1| e^{-i2\delta\theta(0)} . \tag{2.27}$$

The non-zero modes $\delta\theta(x)$ correspond to quantum fluctuations, while higher harmonics in the expansion induce jumps of more than one unit of angular momentum. The latter can be ignored for a weak barrier, their probability becoming exponentially small as the angular momentum difference increases [125].

To calculate the current using perturbation theory to first order in the barrier potential, according to Eq. (2.6), we need to average the total Hamiltonian $\mathcal{H} = \mathcal{H}_0 + \mathcal{H}_\mathrm{b}$ over the unperturbed ground state of the system. The average is performed in two steps. First, using the mode expansion of the field θ we average the total Hamiltonian over the non-zero modes, obtaining an effective Hamiltonian for the angular momentum operator. The average over the non-zero modes is done by employing the zero-temperature relations $\langle b_q^\dagger b_{q'}\rangle = 0$, and $\langle b_q b_{q'}^\dagger\rangle = \delta_{q,q'}$, which lead to the re-

sults $\langle \partial_x \theta(0) \rangle = 0$, since it is linear in the b_q operators, and $\langle \delta\theta^2(0) \rangle = \sum_{q>0}^{2\pi d} \pi K/qL \approx (K/2)\ln(d/L)$, where d is a short distance cut-off of the order of the interparticle distance n_0^{-1}. Hence $\langle e^{\pm i2\delta\theta(0)} \rangle = e^{-2\langle \delta\theta^2(0)\rangle} = (d/L)^K$. We can now write an effective Hamiltonian for the angular momentum operator J

$$\mathcal{H}_J = E_0(J-\Omega)^2 + n_0 U_{\rm eff} \sum_J |J+1\rangle\langle J| + \text{H.c.}\,, \tag{2.28}$$

where we have introduced the effective barrier strength

$$U_{\rm eff} = U_0 \left(\frac{d}{L}\right)^K \tag{2.29}$$

that takes into account the renormalization introduced by the screening of the barrier due to density quantum fluctuations. By choosing $d = K/n_0$, this expression coincides with the exact TG result at $K = 1$, see Eq. (2.17), and takes into account the shrinking of the linear region of the excitation spectrum once interactions are decreased away from the TG limit. Note that the quantum fluctuations of the density suppress the effective barrier strength more for weak interactions ($K \gg 1$) than for strong interactions ($K \gtrsim 1$). This is coherent with the larger suppression of density fluctuations at strong interactions expected from LL, which predicts a power-law scaling of the density-density correlation function $\langle \rho(x)\rho(x') \rangle \propto |x-x'|^{-2K}$ [49, 50]. In a second step, we represent the effective Hamiltonian $\mathcal{H}_J$ on the basis of the angular momentum eigenvectors. The ground state value of $\mathcal{H}_0$ is characterized by a quantum number J which depends on the value of the Coriolis flux Ω, and in the absence of the barrier is the integer closest to Ω. At half-integer values of Ω there is a degeneracy of the ground state. This degeneracy is lifted by the barrier. In the weak barrier limit $\lambda_{\rm eff} = mU_{\rm eff}L/\pi\hbar^2 \ll 1$, degenerate perturbation theory yields the ground state energy

$$E(\Omega) = NE_0\Big[\delta\Omega^2 - \sqrt{\delta\Omega^2 + \lambda_{\rm eff}^2/4\pi^2}\Big]\,, \tag{2.30}$$

with $\delta\Omega = \Omega - 1/2$. As a result, upon using the thermodynamic relation (2.6), the persistent current is given by a smeared sawtooth

$$I(\Omega) = -NI_0\,\delta\Omega\Big[1 - \Big(\sqrt{4\delta\Omega^2 + \lambda_{\rm eff}^2/\pi^2}\Big)^{-1}\Big]\,, \tag{2.31}$$

The corresponding amplitude α is shown in Fig. 2.5 for small values of the dimensionless barrier strength λ. For decreasing interactions down from the TG limit, the quantum fluctuations of density increase, thereby suppressing the barrier more strongly, and thus increasing α. Interestingly, the renormalization by quantum fluctuations at

intermediate interactions is effective enough to turn a relatively large barrier into a weak one. This quantum healing phenomenon completely changes the physical scenario and illustrates the dramatic effect of interplay of interactions and quantum fluctuations.

Strong barrier – In order to treat the case of a strong barrier, we start by considering a ring which is cut by an infinitely large barrier at $x = 0 = L$. The appropriate mode expansion for the Luttinger fields θ and ϕ, that diagonalize the $\mathcal{H}_0$ part of the Hamiltonian in the case of open boundary conditions reads [49,50]

$$\theta(x) = \theta_0 + i\sum_{q>0}\left(\frac{\pi K}{qL}\right)^{1/2}\sin(qx)[b_q - b_q^\dagger]\,, \tag{2.32}$$

$$\phi(x) = \phi_0 + \frac{2\pi x}{L} + \sum_{q>0}\left(\frac{\pi}{qLK}\right)^{1/2}\cos(qx)[b_q + b_q^\dagger]\,, \tag{2.33}$$

where $q = j\pi/L$ with j integer. Note that the absence of the angular momentum operator J in this mode expansion is a consequence of the fact that no circulation is allowed in the limit of infinitely large barrier. Inserting Eqs.(2.32) and (2.33) in Hamiltonian (4.18) we obtain

$$\mathcal{H}_0 = \hbar v_s \sum_{q>0} q\left(b_q^\dagger b_q + \frac{1}{2}\right)\,. \tag{2.34}$$

We describe the transport of bosons across a barrier of large but finite strength localized at $x = 0 \equiv L$ via a single-particle tunnelling Hamiltonian

$$\mathcal{H}_\tau = -\tau\psi^\dagger(0)\psi(L) + \text{H.c.}\,, \tag{2.35}$$

where the tunnelling amplitude τ depends on the details of the barrier potential. This Hamiltonian takes into account the possibility for a boson to tunnel through the barrier potential from $x = 0^+$ to $x = L^-$, and the Hermitian conjugate to tunnelling processes in the opposite direction. In the case of a strong barrier τ is small, and the $\mathcal{H}_\tau$ term of the Hamiltonian will be treated as a perturbation. Inserting the representation of the bosonic field, Eq. (1.35), and keeping only the $l = 0$ term, we find the standard Josephson Hamiltonian

$$\mathcal{H}_\tau \simeq -2\tau n_0\cos[\phi(L) - \phi(0) - 2\pi\Omega]\,, \tag{2.36}$$

where the effect of the rotation has been reabsorbed in the definition of the phase field

passing from periodic to twisted boundary conditions.

In order to calculate the current we consider the only term in $\mathcal{H} = \mathcal{H}_0 + \mathcal{H}_\tau$ that depends on the flux Ω, that is the tunnelling part. As in the weak-barrier case, we average Hamiltonian over the fluctuation modes obtaining the Ω-dependent part of the energy

$$E(\Omega) = -2\tau n_0 \langle \cos(\phi(L) - \phi(0) - 2\pi\Omega) \rangle \; . \tag{2.37}$$

Separating the cosine of the sum we get two contributions: the $\sin$ term vanishes taking the average, while the $\cos$ term becomes $\langle \cos(\phi(L) - \phi(0)) \rangle = \langle e^{i[\phi(L)-\phi(0)]} \rangle = e^{-\langle [\phi(L)-\phi(0)]^2 \rangle/2}$. Making the same choice for the short-distance cut-off length d as in the weak-barrier case above, we get $\langle [\phi(L) - \phi(0)]^2 \rangle = 4 \sum_{q>0}^{\pi d} \frac{\pi}{qLK} (\cos(\pi n_0) - 1)^2 \equiv (2/K) \ln(d/L)$. Thus, finally, we get the the ground state energy

$$E(\Omega) = -2\tau_{\text{eff}} n_0 \cos(2\pi\Omega) \; , \tag{2.38}$$

where the effective tunnelling amplitude

$$\tau_{\text{eff}} = \tau \left(\frac{d}{L} \right)^{1/K} \tag{2.39}$$

takes into account the renormalization introduced by the screening of the tunnelling barrier due to the quantum phase fluctuations. Using the thermodynamic relation (2.6), we get immediately the persistent current

$$I(\Omega) = -(2\tau_{\text{eff}} n_0/\hbar) \sin(2\pi\Omega) \, . \tag{2.40}$$

Notice that in this tunnel limit the persistent current has a sinusoidal shape, differently from the weak interaction case. Increasing the interaction strength the quantum phase fluctuations screen more the tunnelling amplitude, that translates into a smaller value of the current amplitude α. This is coherent with the large effect of phase fluctuations at strong interactions expected from the Luttinger power-law behaviour of the one-body density matrix $\langle \psi^\dagger(x)\psi(x') \rangle \propto |x - x'|^{-1/2K}$ [49,50]. Note the dual nature of this behaviour (exponent $1/K$) as compared to the one obtained for a weak barrier (power K), Eq. (2.31).

The duality between the two models can also be used to establish a link between the tunnel amplitude τ and dimensionless barrier strength λ at given interparticle interactions. For this purpose we use the result of Weiss [126]

$$\tau/L = \Gamma(1+K)\, \Gamma(1+1/K)^K \, (\hbar\omega_c)^{1+K} \, (U_0/L)^{-K}, \tag{2.41}$$

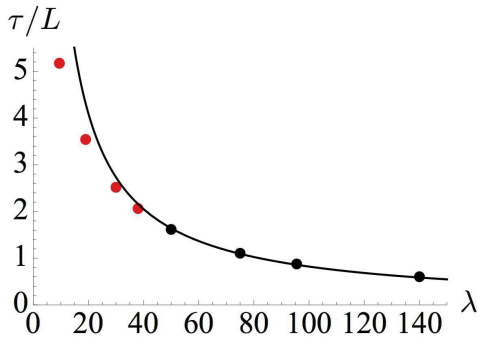

Figure 2.8: Tunneling amplitude τ *vs.* barrier strength λ in the TG limit for $N = 18$. For the red dots, the value of λ is too weak for the tunneling approximation to hold, and a deviation from the hyperbolic behaviour is observed.

where $\Gamma(...)$ is the Euler Gamma function, and the model-dependent cut-off frequency ω_c is determined using the exact TG result in the case $K = 1$. In essence, for large values of the barrier strength we perform exact calculations of the current I *vs.* Coriolis flux Ω, then use Eq. (2.40) as fitting function to extract the value of the tunnel amplitude τ. The resulting dependence of τ on the barrier strength is shown in Fig. 2.8. For sufficiently large values of the barrier strength (*i.e.*, $\lambda \gtrsim 50$) a very good agreement is found with the hyperbolic law (2.41), allowing therefore to extract ω_c.

The persistent current amplitude for large barrier is also shown in Fig. 2.5 for large values of the dimensionless barrier strength λ. Both for weak and large barriers, the LL description breaks down for sufficiently weak interactions when the short-distance cut-off required in the theory increases, until it becomes comparable with the system size.

2.3.4 DMRG numerical results

Away from the weakly and the strongly interacting regime and for arbitrary barrier strength it is difficult to tackle the many-body Schrödinger equation corresponding to Hamiltonian (2.1) with analytical approaches; therefore, we resorted to numerical simulations based on a density-matrix renormalization-group (DMRG) approach (see, *e.g.*, Ref. [56,57]). This technique has been implemented by our collaborators.

After discretizing the space on M sites, we map Eq. (2.1) onto a Bose-Hubbard model on a 1D ring lattice:

$$\mathcal{H} = \sum_{j=1}^{M} -t \left(e^{-i\frac{2\pi\Omega}{M}} b_j^\dagger b_{j+1} + \text{H.c.} \right) + \frac{U}{2} n_j (n_j - 1) + (\Lambda\, \delta_{j,1} n_j - \mu\, n_j) \ , \tag{2.42}$$

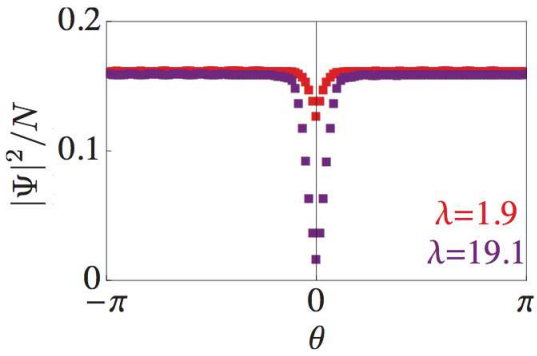

Figure 2.9: Normalized density computed with the numerical DMRG technique *vs.* angular coordinate θ along the ring, for the values of the dimensionless barrier strength λ specified in the figure and $\gamma = 3.3$, $N = 18$, $\Omega = 0.4$.

where $b_j^\dagger$ (b_j) are bosonic creation (annihilation) operators at site j, $n_j = b_j^\dagger b_j$ counts the number of bosons on site j, t is the tunnel energy for bosons on adjacent sites, U is the on-site repulsion energy, Λ is the barrier strength, and μ is the chemical potential. The presence of the gauge flux Ω is taken into account through the Peierls phase twist Ω/M [110, 127]. By taking the continuum limit of Hamiltonian (2.42), we link the parameters t, U and Λ of the Bose-Hubbard model to the parameters m, g and U_0 of the continuum Hamiltonian (1) in the main text. Specifically we have $\hbar^2/2m = ta^2$, $g = Ua$ and $U_0 = a\Lambda$, where $a = L/M$ is the lattice spacing of the discrete model.

In order to minimize the lattice effects and be able to compare the results for the discrete system with the ones for the continuous one, we have chosen the parameter of the discrete model in such a way to be in a low filling regime. In this way the particles occupy only the low parabolic part of the cos energy dispersion of the Bose-Hubbard model, and mimic, with an effective mass, the behaviour of free particles in the continuum having a parabolic dispersion. In the simulations we have chosen $M = 120$ sites and fixed the chemical potential μ in such a way to have $N \sim 18$ particles in the system. We thus kept an average low filling $\langle n_j \rangle \lesssim 0.15$. The resulting density profiles are shown in Fig. 2.6, and Fig. 2.9. For large interactions the density profiles display Friedel oscillations, in very good agreement with the analytical predictions in the TG limit (Fig. 2.6). The oscillations are strongly damped at intermediate and weak interactions.

The amplitude α of the persistent current computed with the DMRG technique, for a large range of barrier heights and interaction strengths, is shown in Fig. 2.5. The DMRG algorithm allows us to reach an accuracy of the order 10^{-7} in terms of absolute values of energies, thus leading to an error in the extrapolation of the particle current $I(\Omega)$ of the order of 1%, that is barely visible on the scale of Fig. 2.5. A further and

most important source of inaccuracies comes from the determination of the average number of particles N, which in some cases (especially for small interactions) becomes less accurate when varying the barrier strength. As a combination of these two sources of errors, the bars in Fig. 2.5 have been computed from point to point.

Remarkably, the numerical approach confirms the non-monotonic behaviour estimated connecting the weak- and strong-interaction results. We understand this effect as being a result of the interplay between barrier backscattering and interaction effects. Furthermore, this results allows us to confirm the expected regimes of validity of the analytical predictions.

2.3.5 Conclusion on optimal amplitude of persistent currents

In this section I have presented our study of the persistent currents for interacting one-dimensional bosons on a tight ring trap, subjected to a rotating barrier potential, which induces an artificial $U(1)$ gauge field. Our results, summarized in Fig. 2.5, evidence the presence of a regime, at intermediate interaction strength, in which the the persistent current response is maximal. This is due to a subtle interplay of effects due to the barrier, the interaction and quantum fluctuations. While at increasing interactions a classical bosonic field screens the barrier more and more, going towards the strongly correlated regime, quantum fluctuations screen the barrier less and less. Our results imply that, for intermediate interaction strengths, unwanted impurities or imperfections on the ring are expected to only weakly affect the system properties. On the other hand, for the applications to quantum state manipulation, the regimes of choice should be either weak or strong interactions, since these are the regimes where the system responds stronger to a localized external probe. Our predictions are relevant for ongoing experiments with ultracold atomic gases on mesoscopic rings, and could be tested via time-of-flight measurements of the momentum distribution, similar to those used to probe circulation in atomic rings [94,95], see Sec. 3.4 of Chap. 3 for a thorough analysis.

As a final remark, I would like to stress that the calculations presented in this section refer to a system at zero temperature. The presence of thermal fluctuations at low but finite temperature is expected to give rise to an additional smearing of the persistent currents, starting from a typical temperature $k_B T \sim N E_0$ [84,115,128]. For a system of 18 ^{87}Rb atoms, as the one considered in Fig. 2.5, confined in a ring of ~ 5 μm diameter, a system size that should be attainable in the next-generation of experiment on a chip, this corresponds to a typical energy $N E_0 \sim 550$ Hz.

The persistent current that we have studied is a thermodynamic, equilibrium, quantity. But the interplay of barrier, interactions and quantum fluctuations should

have a similar impact also on out-of-equilibrium properties such as collective excitation modes and transport phenomena. We have explored these features in Ref. [19], and they are the object of Chap. 4.

2.4 Optimal scaling of persistent currents

In the previous section, I have discussed how the persistent current amplitude depends, at fixed ring length L, on the barrier height and on the interaction strength, finding an optimal regime at intermediate interaction strength, where the current amplitude is maximal. In this section I focus on another important property of persistent current, especially in view of their experimental observation, namely the scaling of the persistent current amplitude with the system size. The results presented in this section are part of the original work of my PhD and are summarized in the second publication [17]. This work has been the result of a collaboration of our group with Matteo Rizzi [5], Davide Rossini [6], Davit Aghamalyan [7], Luigi Amico [8], and Leong-C. Kwek [9].

In Sec. 2.2 I have discussed how the persistent current phenomenon, namely the particle current response to the flux of an applied gauge field, is a manifestation of the Aharonov-Bohm effect at the many-body level, that occurs when the phase coherence length of the fluid extends to the whole system. This effect vanishes when the system size is large and phase fluctuations wash out the coherence.

A first simple consideration on the scaling properties of the persistent current can be obtained already from the current unit we have chosen. As I have already discussed in Sec. 2.2, in the absence of the barrier and for any interaction strength, the ground-state energy of Hamiltonian (2.1) is given by a series of parabolas corresponding to states of well-defined circulation, and the corresponding persistent current is a perfect sawtooth of the maximal attainable amplitude NI_0, where $I_0 = 2\pi\hbar/mL^2$ is given in Eq. (2.8). Hence, we notice immediately that in the thermodynamic limit ($N \to \infty$, $L \to \infty$, at fixed $n = N/L$) the persistent current amplitude $NI_0 \propto n_0 L^{-1}$ vanishes, the persistent current being thus a mesoscopic phenomenon, as is well known [88, 129].

We have considered again Hamiltonian (2.1), and in order to solve the many-body problem associated with it, and study how the current amplitude α depends on the

[5] Institut für Physik, Johannes Gutenberg-Universität, Staudingerweg 7, D-55099 Mainz, Germany.
[6] NEST, Scuola Normale Superiore and Istituto Nanoscienze-CNR, I-56126 Pisa, Italy.
[7] Centre for Quantum Technologies, National University of Singapore, Singapore 117543.
[8] CNR-MATIS-IMM & Dipartimento di Fisica e Astronomia, I-95127 Catania, Italy and Centre for Quantum Technologies, National University of Singapore, Singapore 117543.
[9] Centre for Quantum Technologies, National University of Singapore, Singapore 117543 and Institute of Advanced Studies, Nanyang Technological University, Singapore 637616.

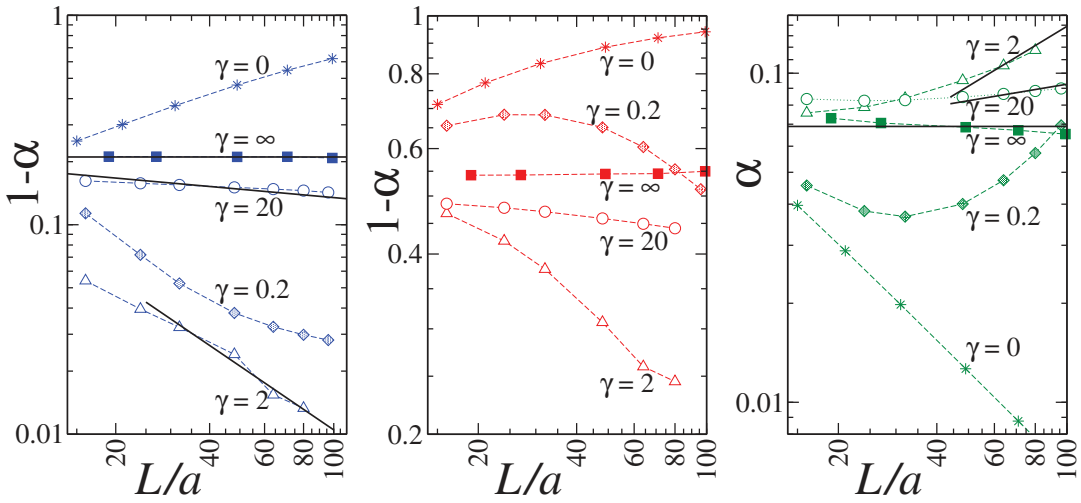

Figure 2.10: Log-Log plots of the persistent current amplitude versus system size L/a, at fixed density $n_0 = 0.25/a$ at various values of the interactions $\gamma = \infty$ (TG (■)), 20 (DMRG (◯)), 2 (DMRG (△)), 0.2 (GP (♢)), 0 (NI (∗)). For weak barrier strength $U_0 4\pi^2 a/E_0 L^2 = 0.1$ (blue) and 1 (red), we plot $1-\alpha$, with faster decaying curves being more favourable for the current, while for large barrier strength $U_0 4\pi^2 a/E_0 L^2 = 10$ (green) we more conveniently show α, with reverted meaning of the scaling behaviour. The solid black lines show the predictions of the LL, Eq. (2.43) for weak barrier (first panel) and (2.44) for strong barrier (third panel), with LL parameter $K|_{\gamma=\infty} = 1.00$, $K|_{\gamma=20} \simeq 1.20$ and $K|_{\gamma=2} \simeq 2.52$, as extracted from the asymptotic expansions of $K(\gamma)$, see Eqs. (1.26), (1.27).

system size, for various values of barrier and interaction strengths, we have resorted to the same combination of analytical and numerical techniques employed in Sec. 2.2. At arbitrary barrier strength and for intermediate-to-strong interactions we have adopted a DMRG numerical technique, in which space has been discretized in M lattice sites of spacing $a = L/M$, that we take as the length unit, see Sec. 2.3.4. In the two opposite limiting cases of non-interacting and infinitely interacting Tonks-Girardeau gas, the many-body problem reduces to a single-particle one and is therefore solved exactly, as in Sec. 2.3.1. At weak interactions the bosonic fluid is described within a mean-field approximation via the Gross-Pitaevskii equation, see Sec. 2.3.2. Finally, at strong interaction, we use the Luttinger liquid theory developed in Sec. 2.3.3.

In Fig. 2.10 I show the scaling of the persistent current amplitude α calculated with the above mentioned methods. We observe that for all values of the barrier the scaling strongly depends on the interaction strength. In the NI regime the scaling is unfavourable, because increasing the system size the current amplitude vanishes even faster than $n_0 L^{-1}$, the overall scaling factor encoded in the current unit NI_0. At increasing interactions, we observe instead that the scaling gets more favourable,

because the decay of the current amplitude with the system size is, in part, compensated by many-body effects. In particular, we observe that there is an optimal regime, at intermediate interactions ($\gamma \simeq 2$), for which the scaling is the most favourable, in all the regimes of barrier height. In the first and third panels of Fig. 2.10 we notice that, at large enough interactions, the current amplitude obtained numerically scales as a power law. In order to give a theoretical interpretation to this behaviour we consider the results obtained for the LL theory in Sec. 2.3.3. For a small barrier strength we have obtained Eq. (2.31) for the persistent current. The amplitude of the current given by this expression, in units of NI_0, is then $\alpha = 1 - (3/2)(\lambda_{\rm eff}/\pi)^{2/3}$, where $\lambda_{\rm eff} = mU_0(d/L)^K L/\pi\hbar^2$ is the effective barrier strength, renormalized by the quantum fluctuations of the density (see Sec. 2.3.3 for details). Therefore, we obtain the scaling

$$1 - \alpha \propto L^{(2/3)(1-K)} . \tag{2.43}$$

In the opposite regime of large barrier strength, we we have obtained Eq. (2.40) for the persistent current. The amplitude of the current given by this expression, in units of NI_0, is $\alpha = 2\tau_{\rm eff} n_0/NI_0$, where $\tau_{\rm eff} = \tau(d/L)^{1/K}$ is the effective tunnelling amplitude across the barrier, renormalized by the quantum fluctuations of the phase (see Sec. 2.3.3 for details). The tunnelling amplitude t across the barrier, depends on the system size, and is related to the barrier strength via Eq. (2.41), with cut-off energy $\hbar\omega_c \sim NE_0 \sim n_0 L^{-1}$. Therefore the current amplitude α, in units of NI_0, for large barrier scales as

$$\alpha \propto L^{1-1/K} . \tag{2.44}$$

In Fig. 2.10 one can note the good agreement of the numerical results with the LL expressions (2.43) and (2.44).

2.4.1 Conclusion on the optimal scaling of persistent currents

In this section I have shown our results on the scaling of the persistent currents with system size. We have found that the scaling depends on the interaction strength, and that the persistent current amplitude decreases slower at intermediate interactions than at very large or very small ones. This non-monotonic effect can be understood also in this case in terms of the combination of the effects of interaction and quantum fluctuations that determine a screening of the barrier.

Our results are important in view of the forthcoming experimental realizations, where the best regime for observing the largest possible current signal should be found from the trade-off between realizable small system size and interaction strength.

Résumé du chapitre

Courants permanents pour bosons en interaction dans un anneau

Dans ce chapitre, je présente notre étude des courants permanents dans un système de bosons unidimensionnels en interaction, confinés dans un piège en forme d'anneau.

Le phénomène des courants permanents est une manifestation de l'effet Aharonov-Bohm. Une des conséquences les plus frappantes de cet effet dans la matière condensée se produit lorsqu'on considère par exemple un anneau métallique mésoscopique à basse température traversé par un champ magnétique statique. Dans ce cas, l'effet Aharonov-Bohm se manifeste sous la forme d'un courant d'équilibre circulant sans dissipation à travers le système, même en l'absence de toute tension appliquée. L'étude théorique et expérimentale de ce phénomène paradoxal d'un courant électrique qui circule sans dissipation d'énergie dans un milieu normalement résistif a attiré une attention considérable au cours des 50 dernières années.

Des développements récents dans la manipulation des gaz atomiques ultrafroids a conduit à la réalisation de pièges annulaires micrométriques, qui offrent une nouvelle plate-forme pour l'étude du phénomène des courants permanents. Les gaz ultrafroids sont des fluides quantiques modèles, caractérisés par de longs temps de cohérence, et qui par rapport à leurs homologues électroniques sont extrêmement ajustables et propres. Dans plusieurs expériences, un condensat de Bose-Einstein d'atomes ultrafroids confinés sur un piège en forme d'anneau a été mis en mouvement par agitation d'un faisceau laser répulsif bien focalisé qui agit comme une sorte de cuillère optique. De cette façon, des courants à circulation quantifiée ont été induits dans le système. L'état de circulation du système peut être testé par des mesures de temps de vol, qui permettent d'accéder à la distribution d'impulsions du gaz.

Le scénario devient particulièrement intrigant si la section transversale de l'anneau est suffisamment petite pour confiner efficacement le système à une dimension. Dans ce cas, les effets conjugués des interactions, des fluctuations quantiques et de la présence d'une barrière de potentiel, dont les effets sont tous amplifiés en 1D, jouent un rôle de première importance. Dans ce contexte, nous avons fourni une caractérisation complète des courants permanents pour les bosons en 1D, nous avons étudié son amplitude et renormalisation avec la taille du système dans tous les régimes d'interaction et de amplitude de la barriere.

En combinant des techniques analytiques ainsi que numériques adaptées pour le problème 1D, nous avons constaté que l'amplitude du courant est une fonction non-monotone de la force d'interaction et présente un maximum prononcé aux interactions intermédiaires dans tous les régimes de hauteur de la barrière. La présence d'un régime optimal d'amplitude maximale du courant illustre la combinaison hautement non triviale des corrélations et des fluctuations quantiques qui déterminent un écrantage de la barrière. Nous avons également constaté que la renormalisation dépend de la force des interactions, et que l'amplitude du courant permanent

diminue avec la taille du système plus lentement pour les interactions intermédiaires que dans les régimes de fortes ou faibles interactions.

Nos résultats sont importants dans la perspective des prochaines réalisations expérimentales, où le meilleur régime pour observer le meilleur signal devrait résulter du compromis entre la réalisation d'une petite taille du système et la force des interactions.

Chapter 3

Flux qubit and superposition of circulation states in a ring-lattice

3.1 Introduction

In the introduction of Chap. 2, I have discussed how the recent development in the micro-fabrication of ring traps for ultracold atomic gases has disclosed a novel platform for the study of persistent currents. However, this progress has boosted not only fundamental research but also the development of technological applications of such systems, leading to the foundation of atomtronics, an emerging interdisciplinary field that seeks to develop devices and circuits where ultracold atoms play the role of electrons in electronics [15]. Key features of atomtronic circuits are the high degree of control, where it is possible to chose the statistic of the current-carrying particles (bosons/fermions), to change the geometry and the dimensionality of the system, and to tune the interactions from attractive to repulsive as well as to choose short- or long- range ones. Furthermore, the neutrality of the atoms carrying the current, and their consequent insensitivity to the electromagnetic environment, substantially reduces decoherence sources.

The most paradigmatic example of an atomtronic circuit is provided by a Bose-Einstein condensate flowing in a ring-shaped trapping potential [89,91,94,95]. If a potential barrier is painted along the ring, giving rise to a so-called weak link, *i.e.* a region of low atomic density where atoms can tunnel through the barrier, this creates an ultracold atoms analogue of the rf-SQUID: a superconducting ring interrupted by a Josephson junction [130], namely an atomtronic quantum interference device (AQUID). The first experimental realizations made use of a Bose-Einstein condensate confined along a toroidal potential, where a potential constriction (giving rise to the aforementioned

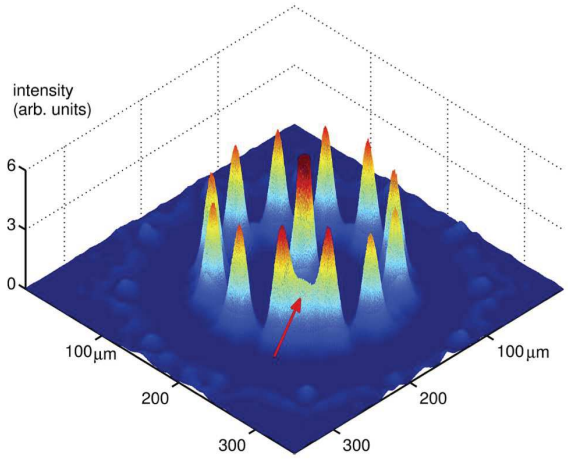

Figure 3.1: Experimental realization of a ring-lattice potential with an adjustable weak link, created by a potential barrier localized on one lattice well (red arrow). The figure shows the measured optical intensity distribution realized with a spatial light modulator, as reported in [135]. The central peak is the residual zero-order diffraction and does not affects the geometry of the ring-lattice. The size of the structure is scalable from a radius of $\sim 90\mu$m to $\sim 5\mu$m. (Figure from Ref. [135]).

weak link) was created via a focused laser beam or a painting potential [96–98, 131]. The interest in creating an atomic analogue of the SQUID comes mainly from the possible applications in the field of quantum information. In this context the SQUID has already been applied to realize qubits, namely quantum two-level systems, via macroscopic quantum superposition states of many-body current states [132–134]. Thanks to the above mentioned tunability of ultracold atomic systems, the AQUID is expected to push even forward the progress in this field.

The possibility to realize macroscopic superposition states with an AQUID has been the object of recent theoretical investigation. It has been shown that the presence of a weak link indeed generates a macroscopic two-level system, whose features have been studied in some special cases so far [81,103–106,136]. For instance, a NOON superposition state, a maximally entangled state very interesting for quantum computation, which is constituted by a two-mode superpositon of all the atoms having *e.g.* zero or one quanta of angular momentum, has been predicted to be very unfavourable to realize, being very sensitive to particle losses and displaying an exponentially decreasing gap of the corresponding two-level system with the particle number [81,106]. The regime of infinitely strong interactions between the particles, instead, has been identified to be favourable from this point of view, the qubit gap being insensitive to the particle number, as long as the weak-link is extremely localized on the ring circumference [104].

In this chapter I present a systematic study of the quality of the qubit in an AQUID, with the aim of identifying the best regime of system parameters for its experimental realization. We consider specifically an interacting Bose gas tightly confined to a 1D ring-shaped optical lattice, in the presence of an artificial gauge potential inducing a persistent current through it, and a potential barrier. This set-up can be realized following different routes, for instance by interfering a Laguerre-Gauss beam with a plane wave, or via a spatial light modulator, see *e.g.* [135, 137] and Fig. 3.1. It presents several advantages for the design of an AQUID. From an experimental point of view, the presence of the lattice helps to realize effective one-dimensional dynamics, to tune the interparticle interaction strength [28], and allows to localize the barrier potential to a single lattice well, which has been found to be important for a favourable scaling of the qubit gap [104]. We have corroborated the emergence of an effective two-level system in such a setup for certain values of the artificial gauge flux, and we have assessed its quality, in terms of its inner energy gap and its separation from the rest of the many-body spectrum, examining its dependence on the system size, the bosonic density, and the interaction and barrier strengths. Furthermore, we have studied how it is possible to observe experimentally, via time-of-flight measurements of the momentum distribution, the superposition of the circulation states characterizing the states of the qubit. By employing a combination of analytical and numerical techniques, that allows us to cover all the relevant physical regimes of system sizes, filling, barrier and interaction strengths, we have shown that a mesoscopic ring lattice with intermediate-to-strong interactions and weak barrier strength is the most favourable regime for setting up, manipulating and probing a qubit in the next generation of atomic experiments. The results presented in this chapter are part of the original work of my PhD, and are summarized in the third publication [18]. This work has been the result of a collaboration of our group with Davit Aghamalyan [1], Matteo Rizzi [2], Davide Rossini [3], Leong-C. Kwek [4], and Luigi Amico [5].

3.2 The ring-lattice

We consider a system of N interacting bosons at zero temperature, loaded into a 1D ring-shaped optical lattice of M sites. The discrete rotational symmetry of the

[1] Centre for Quantum Technologies, National University of Singapore, Singapore 117543.
[2] Institut für Physik, Johannes Gutenberg-Universität, Staudingerweg 7, D-55099 Mainz, Germany.
[3] NEST, Scuola Normale Superiore and Istituto Nanoscienze-CNR, I-56126 Pisa, Italy.
[4] Centre for Quantum Technologies, National University of Singapore, Singapore 117543 and Institute of Advanced Studies, Nanyang Technological University, Singapore 637616.
[5] CNR-MATIS-IMM & Dipartimento di Fisica e Astronomia, I-95127 Catania, Italy and Centre for Quantum Technologies, National University of Singapore, Singapore 117543.

lattice ring is broken by the presence of a localized barrier potential on one lattice site, which gives rise to a weak link. The ring is also threaded by a dimensionless gauge flux Ω, which can be experimentally induced for neutral atoms as a Coriolis flux by rotating the lattice at constant velocity [107], or as a synthetic magnetic flux by imparting a geometric phase to the atoms [108–110, 138–140]. As compared to the system considered in Chap. 2, we consider here the addition of a lattice modulation along the ring circumference.

In the deep optical lattice regime, this system can be described in tight-binding approximation by the 1D Bose-Hubbard (BH) Hamiltonian

$$\mathcal{H} = \sum_{j=1}^{M} -t(e^{-i\frac{2\pi\Omega}{M}} b_j^\dagger b_{j+1} + \text{H.c.}) + \frac{U}{2} n_j(n_j - 1) + \Lambda\delta_{j,1} n_j \ , \tag{3.1}$$

where b_j ($b_j^\dagger$) are bosonic annihilation (creation) operators on the j-th site and $n_j = b_j^\dagger b_j$ is the corresponding number operator. Periodic boundary conditions are assumed in order to account for the ring geometry of the system, and are imposed by taking $M + 1 \equiv 1$ for the lattice sites. The parameter U takes into account the on-site repulsion energy, t is the hopping energy, and $\Lambda\delta_{j,1}$ defines an externally localized barrier potential on a single site. The presence of the flux Ω is taken into account through the Peierls phase twist $2\pi\Omega/M$ [110, 127]. In the thermodynamic limit, the BH model with $\Lambda = 0$ displays a superfluid to Mott-insulator transition for integer fillings $\nu = N/M$, and at a critical value of the ratio U/t of interaction-to-tunnel energy [141, 142]. On a finite system the phase boundaries of the transition are expected to be affected by the presence of the gauge flux [143], although this phenomenon is rather a crossover, the ring being of finite size.

In order to investigate the feasibility and identify the best regime of parameters for the experimental realization of a flux qubit and of a superposition of states of different circulation with the system described by Hamiltonian. (3.1), we have pursued a thorough analysis of the system, for different interaction and barrier strengths, as well as densities and system sizes. In the hard-core limit of infinite repulsions we have applied the Tonks-Girardeau (TG) mapping that allows an exact description. At weak interactions and for large particle numbers we have applied the mean-field Gross-Pitaevskii (GP) approximation. In the continuum limit of small filling and at strong interactions we have applied the Luttinger liquid description developed in Sec. 2.3.3. Lastly, numerical analyses based on truncated and exact diagonalization (ED) methods, and the density-matrix renormalization-group (DMRG) technique have been employed to cover the intermediate parameter regimes. Below I provide some details on

the methods I have implemented myself. For further details on the techniques that have been implemented by our collaborators (DMRG and ED for this study) I refer to the publication [18] and to the references therein.

3.2.1 Hard-core bosons

In the limiting case of infinite repulsive contact interaction between the particles ($U \to \infty$), the so-called hard-core bosons or Tonks-Girardeau gas, an exact approach can be pursed to diagonalize Hamiltonian (3.1). Since multi-occupancy of one site is forbidden by the infinite interaction energy, it can be simplified into

$$\mathcal{H} = -t \sum_{j=1}^{M} (e^{-i\frac{2\pi\Omega}{M}} b_j^\dagger b_{j+1} + \text{H.c.}) + \sum_{j=1}^{M} \Lambda \delta_{j,1} n_j^b \tag{3.2}$$

where the bosonic annihilation and creation operators have the additional on-site constraints $b_j^2 = b_j^{\dagger 2} = 0$ and $[b_j, b_j^\dagger]_+ = 1$. By applying the Jordan-Wigner transformation [144, 145]

$$b_j = \prod_{l=1}^{j-1} e^{i\pi f_l^\dagger f_l} f_j \ , \qquad b_j^\dagger = f_j^\dagger \prod_{l=1}^{j-1} e^{-i\pi f_l^\dagger f_l} f_j \ , \tag{3.3}$$

where f_i ($f_i^\dagger$) are fermionic annihilation (creation) operators, the Hamiltonian (3.2) can be mapped on the one for spinless fermions:

$$\mathcal{H} = -t \sum_{j=1}^{M} (e^{-i\frac{2\pi\Omega}{M}} f_j^\dagger f_{j+1} + \text{H.c.}) + \sum_{j=1}^{M} \Lambda \delta_{j,1} n_j^f \tag{3.4}$$

This Bose-Fermi mapping is the analogue, for a discrete system, of the one introduced by Girardeau for a continuous system, see Sec. 1.2 for more details. Hamiltonians (3.2) and (3.4) have the same spectrum, but non-trivial differences appear for instance in the off-diagonal one-body density matrix: $\langle f_i^\dagger f_j \rangle$ *vs.* $\langle b_i^\dagger b_j \rangle$, which we have calculated following the scheme described in App. B in order to compute the momentum distribution in Sec. 3.4. Hamiltonian (3.4), can be readily represented in matrix form and diagonalized. The mapping thus allows us to calculate exactly the energy spectrum as a function of the flux Ω.

3.2.2 Gross-Pitaevskii equation

In the limit of weak interactions, we adopt a mean-field approximation to determine the ground state properties of the gas. We pursue this approach as a benchmark case for the BH model at weak interaction. Moreover the GP equation is a particularly

suitable tool for the large-N regime, which is routinely realized in experiments.

The Gross-Pitaevskii (GP) equation for the bosons subjected to a lattice potential in the presence of a gauge field reads

$$\frac{\hbar^2}{2m}\left(-i\frac{\partial}{\partial x}-\frac{2\pi}{L}\Omega\right)^2\Phi+U_0\delta(x)\Phi+V_0\sin^2\left(\pi x/a\right)\Phi+g|\Phi|^2\Phi=\mu\Phi\ , \qquad (3.5)$$

where Φ is the condensate wavefunction, μ is the chemical potential, V_0 is the optical-lattice depth, $a=L/M$ is the lattice spacing and L the system size, U_0 is the strength of the localized barrier, m is the particle mass, and g is the effective interaction coupling strength in one dimension. In this continuous model we have modelled the barrier as a delta potential $\delta(x)$. The barrier strength is connected to the discrete-model one Λ by $U_0=\Lambda a$.

In absence of the lattice potential, an analytical soliton solution for Eq. (3.5) has been found in App. A (see also Sec 2.3.2). In the presence of the lattice potential, we solve Eq. (3.5) numerically by imaginary time integration, see Sec. 1.3 fore more details.

3.3 Flux qubit and energy gap

The Hamiltonian (3.1) is manifestly periodic in Ω with period 1, which allows us to restrict its study to the first rotational Brillouin zone $\Omega\in[0,1]$. In addition, the energy spectrum is symmetric with respect to $\Omega\leftrightarrow-\Omega$, and we can further restrict to half of it $\Omega\in[0,0.5]$. As it has been detailed in Sec. 2.2, in the absence of a barrier ($\Lambda=0$), the system is also invariant under discrete rotations and the many-body ground-state energy, as a function of Ω, is given by a set of parabolas each corresponding to a well defined circulation and angular momentum state, shifted with respect to each other by a Galilean transformation and intersecting at frustration points at half-integer values of the flux. The presence of a finite barrier ($\Lambda>0$) breaks the axial rotational symmetry and couples different angular momenta states. Therefore the ground state becomes a superposition of states with different quanta of circulation, and the degeneracy at the frustration points is lifted by the appearance of a gap ΔE_1 in the spectrum, see Fig.2.3. The larger Λ, the larger is ΔE_1, corresponding to the width of the gap separating the first two bands. Provided that the other excitations are energetically far enough from these two levels, this identifies a two-level system and defines the working point for a qubit.

In this section I present a detailed study of the spectroscopy of the qubit. We analyse how the energy gaps ΔE_1, ΔE_2 between the ground and, respectively, the first-

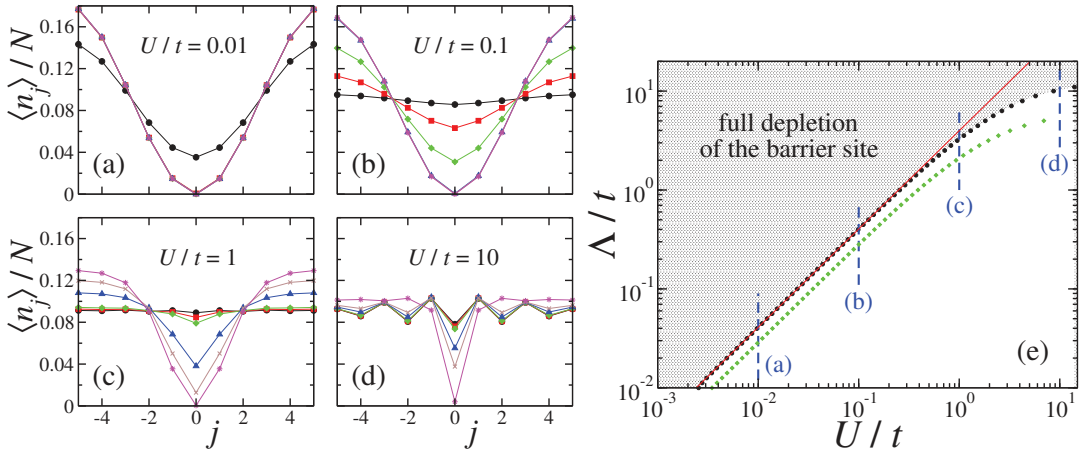

Figure 3.2: (**a-d**) Density profiles $\langle n_j \rangle / N$ at $\Omega = 0.5$, along a ring with $M = 11$ sites and $N = 5$ particles, for different interaction regimes. The various data sets correspond to different values of the barrier strength: $\Lambda/t = 0.01$ (black circles), 0.05 (red squares), 0.1 (green diamonds), 0.5 (blue triangles), 1 (brown crosses), 5 (purple stars). **(e)** Critical values of barrier and interaction strengths Λ and U discriminating the parameters region in which the boson density at the barrier position vanishes (black circles refer to $N/M = 5/11$, green diamonds are for $N/M = 4/16$); the vertical blue dashed lines indicate the interaction parameter corresponding to the densities shown in panels (a-d), while the straight red line is a linear fit.

excited and second-excited energy levels of the many-body Hamiltonian (3.1) depend on the system size and on the filling, for different Λ and U. We find that the qubit is well resolved in the mesoscopic regime of intermediate ring sizes, and that it is at best separated from the higher energy levels of the many-body spectrum in the regime of strong interactions and weak barrier.

3.3.1 Density profiles

Before entering into the detailed analysis of the gap properties, and in order to become familiar with the parameters that characterize the system, I show in Fig. 3.2 the density profiles of the gas at the frustration point $\Omega = 0.5$, for various values of the barrier and interactions strengths.

The presence of the barrier gives rise to a suppression of the particle density on a length scale determined by the healing length of the gas. Depending on the ring size, the whole system can be affected. The depth of the density suppression increases monotonously with Λ (inside each panel), while its width decreases with increasing U (compare the different panels). Notice that the density is suppressed at the barrier position at the expense of multi occupancy of the other sites, hence it competes with the repulsive on-site interactions. The latter effect implies a decrease of the

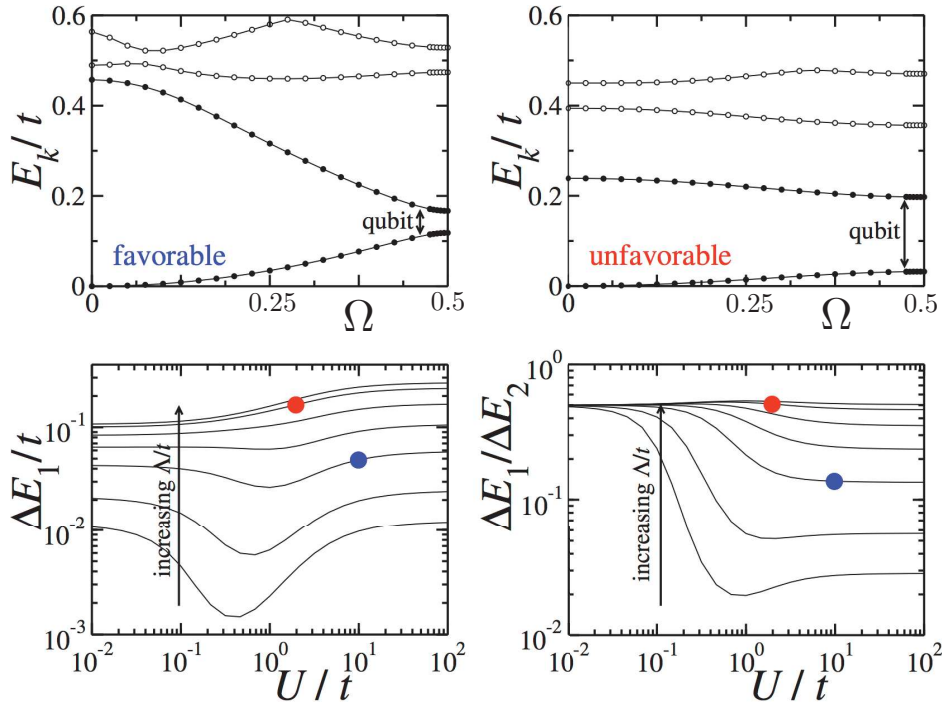

Figure 3.3: Low-energy spectrum of the BH model for various values of the interaction and the barrier strength at fixed size $M = 16$ and filling $\nu = 1/4$. Upper panels: the four lowest energy levels as a function of Ω, for $U/t = 10$, $\Lambda/t = 0.5$ (left) and $U/t = 2$, $\Lambda = 5$ (right). Lower panels: behaviour of ΔE_1 and $\Delta E_1/\Delta E_2$ as a function of U, for different values of Λ/t (curves from bottom to top: $\Lambda/t = 0.1, 0.2, 0.5, 1, 2, 5, 10$).

healing length at increasing the interaction strength. At strong repulsive interactions, Fig. 3.2(d), the barrier induces Friedel-like oscillations in the density [118], analogue to those observed for a uniform ring in Fig. 2.6. These are a consequence of the peculiar strong correlations of 1D bosons that make their response to impurities similar to the fermionic one.

We note also that, a sufficiently large barrier (at fixed U) makes the density at the barrier position vanish, thus effectively disconnecting the ring. The barrier strength required to disconnect the ring depends on the interaction strength. Fig. 3.2(e) shows the result of a thorough analysis of the transition line in the Λ *vs.* U plane. For a wide range of interaction strengths, the critical barrier strengths displays a nearly perfect linear behaviour with U, whose slope is proportional to the filling.

3.3.2 Identification of the qubit: effective two-level system

We consider the low-energy spectrum of Hamiltonian (3.1) obtained by an ED numerical analysis, as shown in Fig. 3.3. The upper-left panel shows how large interac-

tions and moderate barrier strengths cooperate to define a doublet of energy levels at $\Omega = 0.5$, well separated in energy with respect to the higher excited states; weaker interactions and larger barrier strengths, in contrast, do not allow for a clear definition of a two-level system (upper-right panel). We observe that for increasing Λ, as expected, the gap increases and the bands become flatter, thus weakening the dependence of the energy on Ω. The lower two panels display a complete analysis of the behaviour of the spectral gap and its distance to the next excited level at $\Omega = 0.5$ as a function of interactions and barrier strength, allowing us to identify the parameter regime for the existence of an effective two-level system. In particular, we find that a too-weakly interacting gas cannot give rise to a well-defined qubit, since one cannot isolate two levels out of the many-body spectrum with the sole tuning of the barrier strength. Instead, this is possible for larger interaction strengths U. In the light of these results, we conclude that in a certain parameter range, when the interpartice interactions are not too weak, it is possible to identify in the low-energy spectrum of the system an effective two level system that defines a qubit, corresponding to the ground and first excited states at the frustration point at half-integer value of the flux. The problem to identify the best parameter range to define a flux qubit is studied in the next section, taking into account also the gap dependence on the system size and filling.

3.3.3 Gap scaling with system size

It is very important, in view the experimental realization of the flux-qubit defined in the previous section, to study the dependence of ΔE_1 and its separation from the rest of the spectrum on the system size and filling.

In Fig. 3.4 we show both the qubit gap ΔE_1 and the separation of the two levels from the rest of the spectrum in terms of $\Delta E_1/\Delta E_2$, as obtained by DMRG simulations at constant filling $\nu = 1/4$. The three panels correspond to various barrier strengths, from weak to high, and each panel contains curves at varying interparticle interactions, from intermediate to the hard-core limit, the weak interaction regime being excluded based on the results of the previous section. We find a clear evidence of a power-law decay of ΔE_1 with the system size in all the interaction regimes, the exponent depending on the interplay between the barrier and interaction strengths.

In the low-filling regime under consideration ($\nu = 1/4$), the lattice model given by Hamiltonian (3.1) can be mapped on the continuous one of Hamiltonian (2.1), as I have discussed in Sec. 2.3.4. We can thus give an analytical interpretation of the observed scaling law of the gap resorting to the Luttinger-liquid theory for the continuous system. In the small-barrier limit, we have from Eq. (2.30) that $\Delta E_1 \propto n_0 U_{\text{eff}}$, where $U_{\text{eff}} = U_0(d/L)^K$ is the effective barrier strength of the continuous model renor-

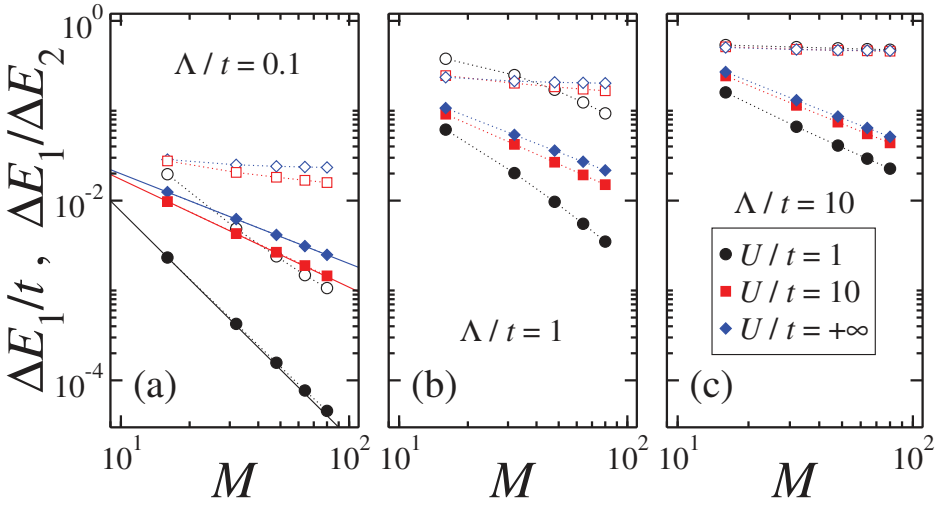

Figure 3.4: DMRG results for the scaling of the qubit gap ΔE_1 (filled symbols) and of the ratio between the gaps $\Delta E_1/\Delta E_2$ (empty symbols) with the system size, at fixed filling $\nu = 1/4$, $\Omega = 0.5$, and the barrier strength Λ specified in the panels. In each plot the various curves stand for different interaction strengths U, as specified in the legend. The straight solid lines in panel (a) correspond to the power-law behaviour predicted by the Luttinger-liquid analysis in the small-barrier limit (3.6), for the values of the Luttinger parameter $K|_{U=\infty} = 1.00$, $K|_{U=10} = 1.20$ and $K|_{U=1} = 2.52$, as extracted from the asymptotic expansions of $K(\gamma)$ given by Eqs. (1.26), (1.27), where $\gamma = U/2t\nu$.

malized by the quantum fluctuations of the density, d is a short distance cut-off of the low-energy theory, L is the system size, and K is the Luttinger parameter (see Sec. 1.4 for details). After converting the continuous barrier parameter in terms of the lattice one Λ, this yields the scaling of the gap with the number of lattice sites M as,

$$\Delta E_1 \propto \nu\Lambda(d/L)^K \propto M^{-K} \ . \tag{3.6}$$

As illustrated in Fig. 3.4(a), we find a very good agreement between the numerical data and the power-law predicted by the Luttinger theory. For stronger barriers, interestingly, we observe in Fig. 3.4(b-c) that the gap still scales as a power-law, even beyond the regime of validity of such perturbative analytical prediction.

By looking at the separation of the effective two-level system from the rest of the spectrum (dashed lines in Fig. 3.4), we get a first clue for identifying an optimal size for the implementation of the flux qubit. If the barrier strength is weak, *i.e.* $\Lambda/t = 0.1$ (Fig. 3.4(a)), the best choice appears to be a mesoscopic lattice size of few tens of sites, filled with strongly enough interacting bosons ($U/t \gtrsim 1$), such that the energy bands are not completely flattened by the presence of the barrier (see again Sec. 3.3.2). However, this parameter regime would allow for a very small qubit gap of the order of

$10^{-3}t$, while this being only about $0.01\Delta E_2$. At intermediate barrier strengths $\Lambda/t = 1$ (Fig. 3.4(b)), a nicely addressable pair of levels with an energy splitting of the order of $10^{-2}t$, and a relative separation from the spectrum of around $10^{-1}t$, can be obtained in a mesoscopic lattice of a few tens of sites. According to our analysis, this is the optimal parameter choice for the realization of a qubit. When the barrier becomes stronger (Fig. 3.4(c)), the size dependence of $\Delta E_1/\Delta E_2$ becomes less and less important, with its absolute value increasing more and more, *i.e.* the qubit gets less and less isolated in energy. If the barrier is strong enough to effectively cut the ring, the low lying levels of the many-body spectrum get almost equally spaced and therefore the qubit definition results to be very poor. Fianlly, rings that are too large in size would improve the definition of the two-level system, isolating it even more from the rest of the spectrum, yet at the price of too small a separation of the qubit levels for practical addressing.

3.3.4 Dependence of the qubit energy spectrum on the filling factor in mesoscopic rings

In the previous section we have identified the regime of mesoscopic size of a few tens of lattice sites, strong enough interactions ($U/t \gtrsim 1$), and not too strong a barrier strength ($\Lambda/t \lesssim 1$) as the best candidate for the flux qubit realization, which benefits simultaneously of a clear definition with respect to the other excited states and a good energy resolution. In this section we focus on the scaling properties of the gap as a function of the particles filling of the system.

In Figs. 3.5 and 3.6 we present our results for the gap ΔE_1 and ΔE_2 as a function of the filling at fixed system size, studying its dependence on the barrier and on the interaction strength. The upper panels of Fig. 3.5 present the data for fixed interaction strength ($U/t = 1$ and $U/t = 10$, respectively) with the different curves representing barrier strengths from weak to strong. At small U (upper-left panel), we observe a smooth dependence of ΔE_1 on the boson filling, as expected in the superfluid regime of Hamiltonian (3.1). The increase of the barrier strength has two effects: first, at fixed filling, it increases the gap since it enhances the effect of the breaking of the rotational invariance and therefore the lifting of the level degeneracy at half-flux. In addition, it changes the dependence of the gap on the filling from being monotonically decreasing to monotonically increasing, passing through a crossover situation. Since the healing length ξ of the system is proportional to $1/\sqrt{\nu U}$, at small barrier strengths a weakly interacting Bose gas screens the barrier, effectively reducing its height as the density is increased. On the contrary, for a large barrier, the system is effectively in the tunnel limit, and the situation is reversed. The barrier strength is effectively enhanced, since the tunnel energy required to move one particle from one side of the barrier to the

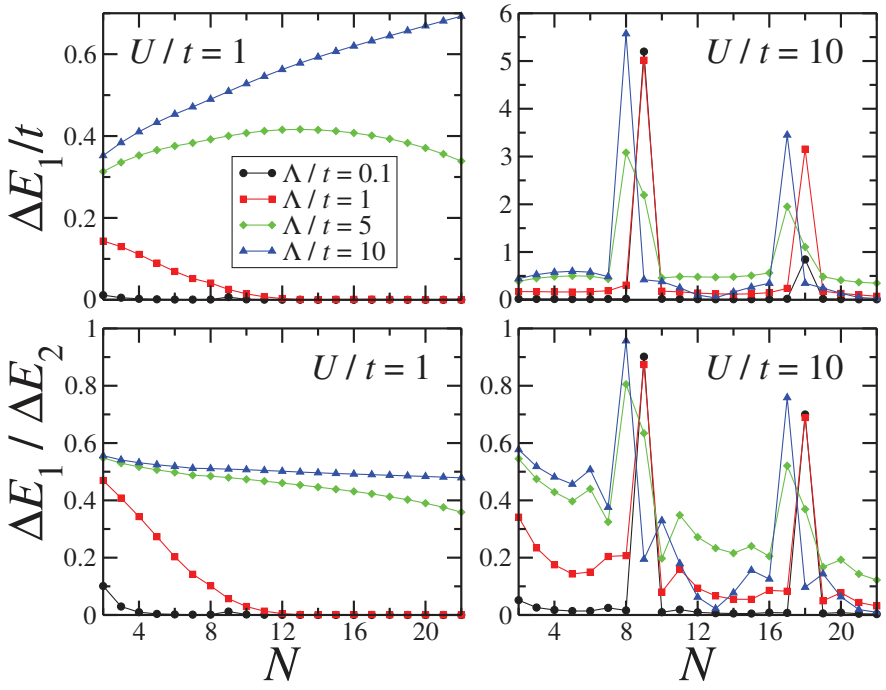

Figure 3.5: ED results for the energy gap ΔE_1 and the ratio $\Delta E_1/\Delta E_2$, as a function of the number of particles, for $M = 9$ lattice sites, at $\Omega = 0.5$, for the interaction strengths U specified in the panels. In each plot the various curves stand for different barrier strengths Λ, as specified in the legend.

other increases if the number of particles or the interaction strength are increased: in order to accommodate the tunnelling particle, the other particles have to readjust their configuration.

At large U (upper-right panel) in Fig. 3.5, ΔE_1 displays a more complex dependence on the filling, with pronounced peaks at particle numbers commensurate (or quasi) with the size, due to the presence of the Mott insulator phase in the phase diagram of Hamiltonian (3.1) [141, 146]. For a weak barrier the peaks appear at integer values of N/M, while for a very strong barrier the density vanishes completely on one site, the system being similar to a lattice with $M - 1$ sites and the peaks are consequently shifted. At intermediate barrier strengths we can observe a transient between the two regimes with broader peaks.

The upper panels of Fig. 3.6 show our results for fixed barrier strength ($\Lambda/t = 0.1$ and $\Lambda/t = 1$, respectively) with the curves representing interaction strengths from weak to the hard-core limit. First, one can clearly observe the non-monotonous dependence of the gap on the interaction strength U, which was illustrated in Fig. 3.3, to hold at all fillings in both panels. Secondly, the dependence of ΔE_1 on N drastically changes increasing the interaction strength, displaying different regimes: quickly

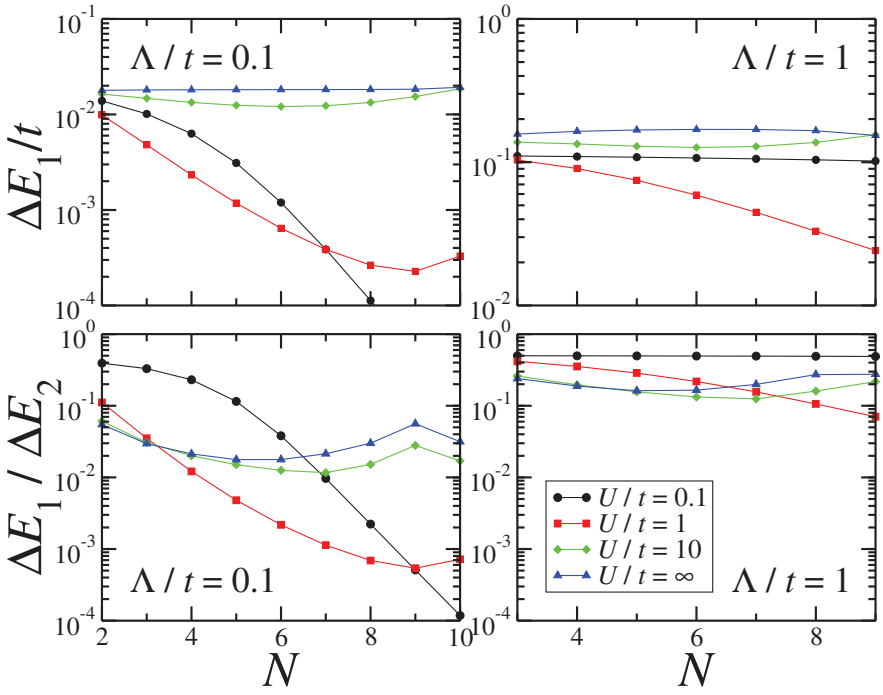

Figure 3.6: ED results for the energy gap ΔE_1 and the ratio $\Delta E_1/\Delta E_2$, as a function of the number of particles, for $M = 11$ lattice sites, at $\Omega = 0.5$, for the barrier strength Λ specified in the panels. In each plot the various curves stand for different interaction strengths U, as specified in the legend.

decreasing, non monotonous and almost constant. The rapid and unfavourable decrease of the energy gap with the number of particles at weak interactions can be understood again in terms of classical screening of the barrier, that is effectively reduced, as the healing length of the gas, by increasing the filling. In the opposite regime of hard core bosons, instead, the energy gap is the same as the one of the non-interacting Fermi gas. This can be readily understood in terms of the TG Bose-Fermi mapping: indeed, in a non-interacting Fermi gas the energy gap is given by $\Delta E_1 = (\sum_{j=1}^{N-1} \epsilon_j + \epsilon_{N+1}) - \sum_{j=1}^{N} \epsilon_j$, where ϵ_j are the single-particle energies. In particular, for a small barrier, using perturbation theory, one obtains that the single-particle energy gaps $\epsilon_{j+1} - \epsilon_j$ are identical for all the avoided levels crossings, hence the gap ΔE_1 is independent of the filling (see Sec. 2.3.1 for a detailed calculation in the continuum).

The lower panels of Figs. 3.5 and 3.6 display the ratio $\Delta E_1/\Delta E_2$, and allow us to complete the identification of the most favourable regime for the qubit to have a well defined gap, taking into account also the effect of the number of particles. This turns out to be, also in the light of these results, the weak-barrier ($\Lambda/t \lesssim 1$), and intermediate-to-strong interaction regime ($U/t \gtrsim 1$), for which the energy gap does

not decrease with the number of particles, but remains almost constant for any value of the filling, provided one is away from the commensurate values of particles and sites that lead to the Mott insulating phase. Indeed, depending on the interaction strength, too large a barrier yields an unfavourable situation similar to the one depicted in the top-right panel of Fig. 3.3, in which $\Delta E_2 \sim \Delta E_1$. It is interesting to notice that these unfavourable cases correspond to values of barrier and interaction strength in the Fig. 3.2(e) where the ring is effectively disconnected. The ratio Λ/U is thus a useful parameter to define the quality of the qubit in terms of its energy resolution: the most advantageous parameter regime for the qubit corresponds to the lower half-plane in Fig. 3.2(e), below the critical line.

Finally, it is interesting to give an estimate of the order of magnitude of the gaps discussed above for a realistic system. For a ^{87}Rb gas in a mesoscopic ring shaped deep optical lattice of $\sim 50\mu$m circumference and 10 lattice wells, the hopping energy is of the order of $t \sim 0.5$kHz. This yields a typical energy scale for the gap of tens to a few hundreds of Hz, depending on the choice of barrier strength, well within the range of experimental accessibility.

3.4 Momentum distribution of a superposition of circulation states

So far I have presented our analysis of the behaviour of the energy spectrum of the flux qubit as a function of the system parameters. Now we investigate the ground state of the system in more detail. Special attention is devoted to the regimes of parameters in which it corresponds to a superposition of states with different circulation. We assess the detectability of the latter through the study of the momentum distribution.

The measurement of the momentum distribution is the most common tool employed in ultracold atoms experiments to get information about the state of motion of the gas, and in particular about the current circulation along the ring [94,95], and it is experimentally accessible in ultracold atoms experiments via the time-of-flight (TOF) expansion technique, which is illustrated in Fig. 3.7. In such measurements, the confining potential that is used to trap the gas is switched off at a given time, at which the system is probed, hence releasing the gas that is free to expand due to its internal momentum. After an expansion time $t_{\rm TOF}$, typically of the order of tens of ms, the density profile of the gas is measured via standard absorption imaging techniques, *e.g.* by a CCD camera. The spatial density distribution measured in this way can be related to the initial momentum distribution of the gas in the trap immediately before the release $\langle n(\mathbf{x})\rangle_{\rm TOF} \propto \langle n(\mathbf{k})\rangle_{\rm trap}$, where the momentum of the gas in the trap $\mathbf{k}$ and

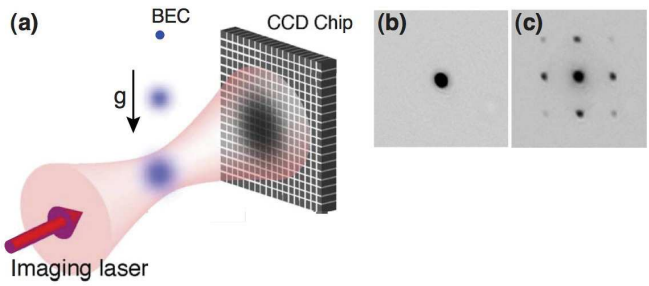

Figure 3.7: **(a)** Schematic set-up for absorption imaging after a TOF expansion time. **(b)** Absorption image for a Bose-Einstein condensate released from a harmonic trap. **(c)** Absorption image for a Bose-Einstein condensate released from a shallow optical lattice. (From Ref. [12]).

the position of the atoms $\mathbf{x}$ after the TOF are related by the ballistic expansion condition $\mathbf{k} = m\mathbf{x}/\hbar t_{\mathrm{TOF}}$, which holds under the assumption that there are no effects due to interaction during the expansion, as it is typically the case with good approximation in experiments [64].

The momentum distribution is defined as the Fourier transform with respect to the relative coordinate of the one-body density matrix

$$n(\mathbf{k}) = \int \mathrm{d}\mathbf{x} \int \mathrm{d}\mathbf{x}' \langle \hat{\psi}^\dagger(\mathbf{x}) \hat{\psi}(\mathbf{x}') \rangle e^{i\mathbf{k}\cdot(\mathbf{x}-\mathbf{x}')}, \tag{3.7}$$

where $\mathbf{x}$ and $\mathbf{x}'$ denote the position of two points along the ring's circumference. Although, in general, $\mathbf{k}$ is a three dimensional wave vector, due to the symmetry of the particular ring configuration we are considering here we restrict to a two dimensional $\mathbf{k}$ in the plane of the ring, which corresponds to a TOF image integrated along the symmetry axis of the ring. To adapt Eq. (3.7) to our lattice system, we expand the field operator in terms of the single particle Wannier functions $w_j(\mathbf{x}) = w(\mathbf{x} - \mathbf{x}_j)$, localized on the j-th lattice site, where $\mathbf{x}_j$ denotes the position of the j-th lattice site $\hat{\psi}(\mathbf{x}) = \sum_{j=1}^{M} w_j(\mathbf{x}) \hat{b}_j$, see *e.g.* [147]. Thereby, after substituting, Eq. (3.7) can be recast into

$$n(\mathbf{k}) = |\tilde{w}(\mathbf{k})|^2 \sum_{l,j=1}^{M} e^{i\mathbf{k}\cdot(\mathbf{x}_l - \mathbf{x}_j)} \langle \hat{b}_l^\dagger \hat{b}_j \rangle, \tag{3.8}$$

where $\tilde{w}(\mathbf{k})$ is the Fourier transform of the Wannier function. For the calculations presented in this section we have assumed an isotropic Gaussian form for the Wannier function. This corresponds to take a harmonic approximation for the lattice well, and is suitable in the tight-binding regime of deep optical lattice. This is the case we have chosen, taking a lattice depth $10E_r$, where $E_r = 2\hbar^2\pi^2 M^2/mL^2$ is the recoil energy of the lattice.

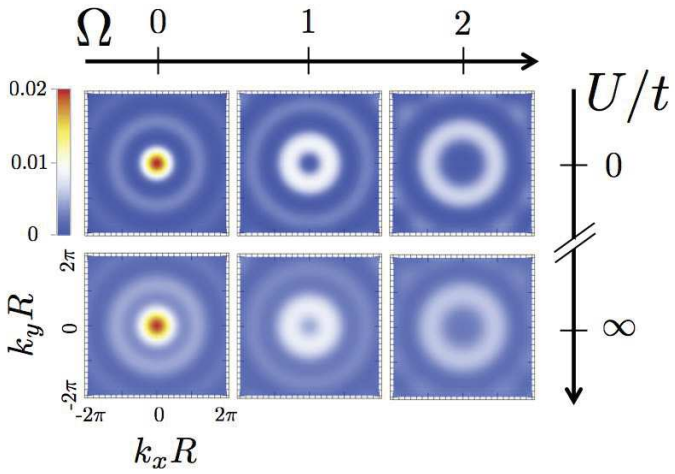

Figure 3.8: NI and TG results for the ground state momentum distribution in the absence of the barrier, for different values of the Coriolis flux: $\Omega = 0, 1, 2$ and different regimes of interaction strength: non-interacting (upper line) and infinite interactions (lower line), at filling $N/M = 5/11$. The wave vector is expressed in unit of the radius of the ring $R = L/2\pi$.

To avoid effects associated with the Mott insulating phase, in the following analysis we focus on incommensurate values of the filling parameter (see Section 3.3.4 for a more detailed discussion).

In absence of the barrier ($\Lambda = 0$), the ground state of the system has no circulation for $\Omega < 0.5$, in this case the momentum distribution is peaked at $\mathbf{k} = 0$, and has one quantum of circulation for $\Omega > 0.5$, in this case the momentum distribution is ring-shaped, the radius of the ring increasing for higher angular momentum states at larger values of Ω [94, 95] (see App. C for a calculation in the non-interacting limit in the continuum). Fig. 3.8 shows the predicted momentum distributions in the absence of the barrier for various values of the interaction strengths. The presence of the ring shape at all interaction strengths reflects angular momentum conservation, consistent with the fact that the persistent currents through a rotationally invariant system are not affected by the interactions [114, 115] (see Sec. 2.2). We note, however, that the detectability in the time-of-flight images is reduced for large interactions, due to the enhanced role of phase fluctuations.

Exactly at the frustration point $\Omega = 0.5$, instead, the momentum distribution displays an interference of the two situations (peaked and ring-shaped), reflecting the fact that the ground state is a superposition of the two states of well-defined angular momentum (see App. C). When $\Lambda > 0$, the superposition occurs for a wider range of Ω, thereby displaying interference effects as shown in Fig. 3.9. The relative weight of the two-quanta-of-circulation components in the superposition strongly depends on Ω, Λ

and U (see Fig. C.1 in App. C). In particular, at the frustration point, the superposition is perfectly balanced, independently of Λ, and U. Away from the frustration point, the relative weights tend to the unperturbed ones carrying zero or one quantum of angular momentum.This phenomenon occurs over a distance in $\Omega - \pi$ that depends on Λ: the smaller is Λ, the faster the unperturbed weights are recovered. For this reason, in Figs. 3.9 and 3.12, in order to study the effects of the barrier and of the interactions on the superposition, we slightly off-set Ω from the frustration point. In this case the weights of the circulating states are not equal, yet close enough to ensure that both angular momentum states contribute significantly to the superposition. For $\Omega > 0.5$, the component carrying one quantum of angular momentum has a larger weight in the superposition, making the effect of the barrier and its screening easily detectable in the momentum distribution; the opposite situation occurring for $\Omega < 0.5$. The momentum distribution results shown in Fig. 3.9 and 3.12 quantitatively depend on the choice of Ω, but the screening effect of the barrier and the detectability of the superposition are weakly affected by this choice. To understand the momentum distribution results of Fig. 3.9, it is instructive to consider first the case without interactions, that, in the continuum case of Hamiltonian (2.1), is easily analytically accessible. The corresponding momentum distribution close to the frustration point and for a weak barrier reads (see Eq. $(C.9)$ in App. C for the derivation)

$$\begin{aligned} n(\mathbf{k}) &= \sin^2(\varphi/2) J_n^2(|\mathbf{k}|R) + \cos^2(\varphi/2) J_{n+1}^2(|\mathbf{k}|R) \\ &\quad + \sin(\varphi)\cos(\gamma_{\mathbf{k}}) J_n(|\mathbf{k}|R) J_{n+1}(|\mathbf{k}|R)\ , \end{aligned} \tag{3.9}$$

where the Bessel functions J_n correspond to states with circulation n, and $\gamma_{\mathbf{k}}$ is the angle along the ring in momentum space; the parameter φ is a function of the flux and the barrier strength (see Eq. $(C.7)$ in App. C). In App. C the difference between the momentum distribution for the continuum model (Hamiltonian (2.1)) and the one on a lattice (Hamiltonian (3.1)) is also discussed. Eq. (3.9) shows that the TOF images allow to visualize the superposition of states with different angular momenta: the functions J_0 and J_1 interfere, giving rise to a peak at zero $\mathbf{k}$ and a fringe with ring-shaped symmetry. The detectability of this feature increases with the barrier strength Λ. Note that the angular position of the peak in momentum space depends on the position of the barrier in real space along the ring, and would be affected by a phase shift between the two states of well-defined angular momentum.

The superposition state for small U displays similar features. We note in Fig. 3.9 that, for sufficiently weak interactions, an angular modulation of the ring-shaped momentum distribution arises. A stronger barrier makes the angular asymmetry increas-

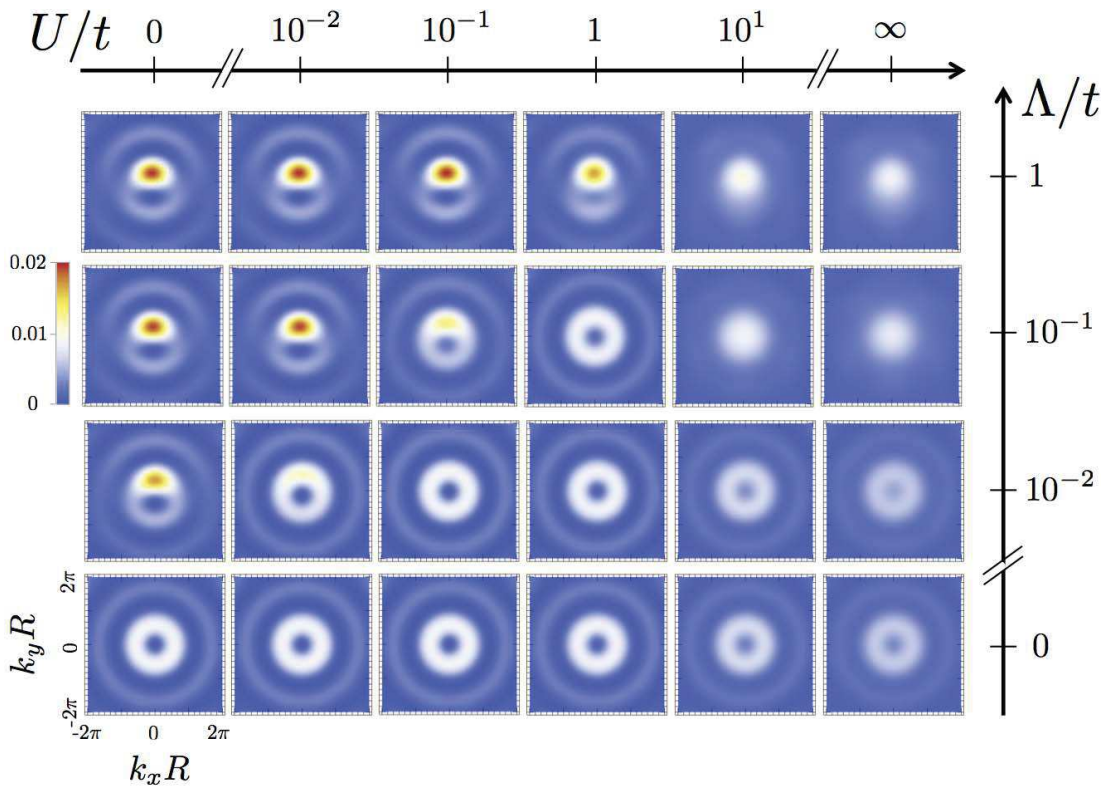

Figure 3.9: ED and TG results for the ground state momentum distribution close to the qubit frustration point: $\Omega = 0.5 + \epsilon$ (hereafter we fix $\epsilon = 10^{-3}$), for different values of the interaction and barrier strengths U and Λ, at filling $N/M = 5/11$. The superposition of circulation states depends on the interplay between U and Λ. For the filling adopted in these graphs, larger values of Λ yield momentum distributions very close to those for $\Lambda/t = 1$. The wave vector is expressed in unit of the radius of the ring $R = L/2\pi$.

ing, while the interaction strength, by screening the barrier, leads to the opposite phenomenon.

Upon increasing the interaction strength from intermediate to very large, we observe a smearing of the modulated ring-shape momentum distribution. This is an effect of increased quantum fluctuations, which leads, for strong barrier strengths, to a single maximum centred at non-zero $\mathbf{k}$ values. The very different momentum distributions between the regimes of weak and strong interactions can be understood by recalling the different nature of the superposition state in the various interaction regimes. A thorough exact diagonalizaiton study for a small system of the nature of the many-body superposition state has been carried out in [104]. For instance, at zero or very weak interactions, within the GP regime, the many-body state is a coherent state of single particle superpositions $|\Psi_0\rangle = [(b^\dagger_{J=0} - b^\dagger_{J=1})/\sqrt{2}]^N|0\rangle$, with J the circulation quanta. Increasing the interaction strength to the intermediate regime

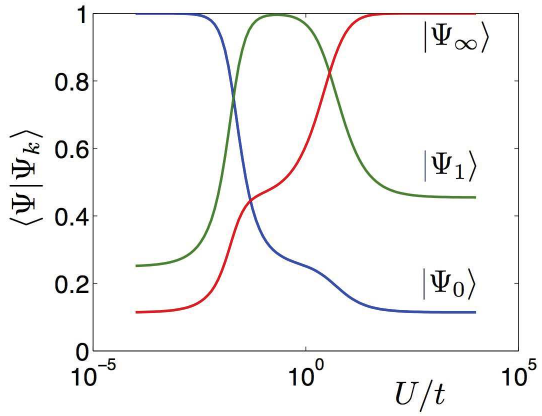

Figure 3.10: Fidelity of the many-body superposition state $|\Psi\rangle$ with respect to the states $|\Psi_0\rangle$, $|\Psi_1\rangle$, and $|\Psi_\infty\rangle$, obtained in [104] via exact diagonalization, for a system of $N = 3$ and $M = 5$ at $\Omega = 0.5$ with $\Lambda/t = 0.01$. (Figure adapted from Ref. [104]).

the superposition is well described by the so-called NOON state $|N, 0\rangle + |0, N\rangle$, *i.e.*, a macroscopic superposition of states where all bosons occupy either the state with zero circulation or the one carrying one quantum of circulation $|\Psi_1\rangle = [(b^\dagger_{J=0})^N - (b^\dagger_{J=1})^N]/\sqrt{2}|0\rangle$. Further increasing the interactions to the hard-core limit the many-body state becomes instead a macroscopic superposition of Fermi spheres $|\Psi_\infty\rangle = [\Psi^{J=0}_\infty - \Psi^{J=1}_\infty]/\sqrt{2}|0\rangle$. In Fig. 3.10 I report the results of [104] for the fidelity of the exact many-body ground state with the reference states mentioned above as a function of the interactions.

For all regimes of interactions, we find that the momentum distributions become independent of the barrier strength above a critical value, which well agrees with the critical value of barrier strength for disconnecting the ring, as identified in Fig. 3.2(e).

To quantify the detectability of the superposition state in the momentum distribution for different barrier and interaction strengths, we define the averaged contrast between the momentum distribution with and without barrier

$$\eta = \frac{\int \mathrm{d}\mathbf{k}\, |n_{\Lambda\neq 0}(\mathbf{k}) - n_{\Lambda=0}(\mathbf{k})|}{\int \mathrm{d}\mathbf{k}\, n_{\Lambda\neq 0}(\mathbf{k}) + n_{\Lambda=0}(\mathbf{k})}\,, \tag{3.10}$$

reflecting the modification in the integrated momentum distribution due to superposition of states induced by the barrier. For small values of barrier strengths, we find that η displays a non-monotonic behaviour upon increasing the interactions between the particles, see Fig. 3.11. This is an effect of the non-monotonic screening of the barrier as a function of interaction strength, analogously to what we found in Chap. 2 in the study of the persistent-current amplitude. We find a higher contrast when the screen-

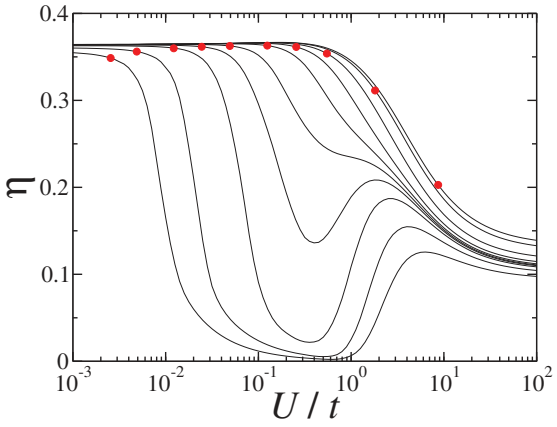

Figure 3.11: Averaged contrast η *vs.* interaction strength U for different values of the barrier strength (curves from left to right: $\Lambda/t = 0.01, 0.02, 0.05, 0.1, 0.2, 0.5, 1, 2, 5, 10$). The red circles denote the critical value of interactions strength, for each value of Λ, defined from the analysis of Fig. 3.2.

ing of the barrier is smaller, *i.e.* for a ratio Λ/U in the vicinity or above the critical line identified in Fig. 3.2(e). This should allow to easily distinguish the presence or not of a superposition state.

Finally, I comment on the expected behaviour for systems with a larger filling than the ones considered so far. The momentum distributions for larger fillings, ranging from values of N/M close to one, obtained via ED, to fillings much larger than one, obtained via the GP Eq. (3.5), are shown in Fig. 3.12. In both cases, they are qualitatively very similar to the ones shown in Fig. 3.9 for smaller number of particles, the main difference being that at higher filling a larger barrier strength is needed, with respect to the lower filling case, to produce the same superposition and to observe a similar momentum distribution, since the screening of the barrier is enhanced at higher filling. Our analysis for small systems is thus also relevant, at least qualitatively, for systems with larger number of particles, like the ones employed in most of the experiments so far.

3.5 Conclusion

In this chapter I have presented our study of a system of bosonic atoms loaded in a ring-shaped one-dimensional optical lattice, whose discrete rotational symmetry is broken by the presence of a potential barrier localized on one site of the lattice, that induces a weak link. In the presence of an artificial gauge flux threading the ring, we have demonstrated that at the frustration points at half-integer values of the flux this system can describe a qubit, whose effective two-level system is given by superposi-

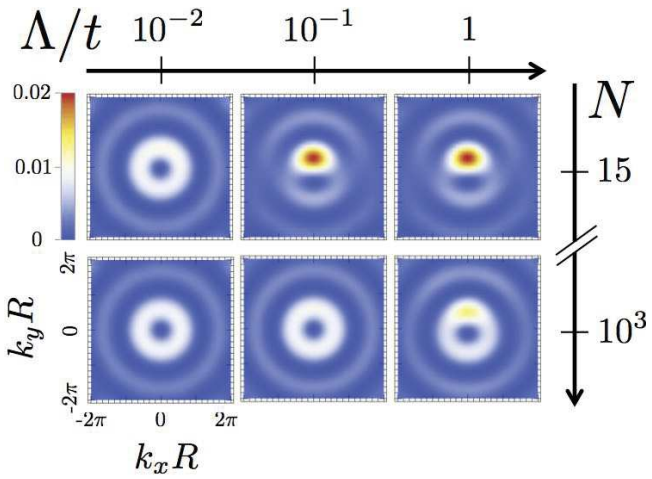

Figure 3.12: Ground state momentum distribution close to the qubit frustration point: $\Omega = 0.5+\epsilon$ for $U/t = 10^{-2}$, $M = 11$ and $N = 15, 10^3$ (obtained from truncated ED and GP respectively). The momentum distributions are qualitatively similar to the ones in Fig. 3.9, but the features of the superposition appear at larger values of Λ, compared to the case at lower filling.

tions of circulation states. In particular, first we have studied the resolution of the qubit by the analysis of the scaling properties of its energy gap and of its separation from the rest of the spectrum for various regimes of the system's parameters. Secondly, we have addressed its detectability from the analysis of the momentum distribution of its ground state.

Our scaling analysis allows us to identify the regime of mesoscopic size (tens of lattice sites) for a sufficiently correlated gas ($U/t \gtrsim 1$) in the presence of a moderately-weak barrier ($\Lambda/t \lesssim 1$) as the best suited for the realization and addressability of the qubit with an adequate number of particles for experimental implementations. Furthermore, we have demonstrated that the superposition of well-defined circulation states defining the ground state of the system is detectable through time-of-flight measurements of the momentum distribution, the best regime for its detection being the regime in which the barrier is less screened by the interactions. In particular, we have identified that the ratio U/Λ is an important parameter to characterize the behaviour of the qubit both in terms of its gap definition and in terms of the detectability of states superposition through the momentum distribution. The optimal regime, corresponding to the best trade-off between the two requirements, corresponds to values of the ratio U/Λ on the critical line identified in Fig. 3.2(e), where a full depletion of the density occurs in correspondence of the barrier site.

Résumé du chapitre

Flux qubit et superposition d'états de courant dans un reseau en anneau

Les développements récents dans la micro-fabrication de pièges annulaires pour les gaz atomiques ultrafroids a stimulé non seulement la recherche fondamentale, mais aussi le développement d'applications technologiques de ces systèmes, ce qui conduit à la fondation de l'atomtronique, un domaine interdisciplinaire émergeant qui cherche à développer des dispositifs où les atomes ultrafroids jouent le rôle des électrons en électronique. Les principales caractéristiques des circuits atomtronics sont le degré élevé de contrôle et la neutralité des atomes transportant le courant, réduisant considérablement les sources de décohérence.

L'exemple le plus paradigmatique d'un circuit atomtronique est constitué par un condensat de Bose-Einstein circulant dans un piège en forme d'anneau. Si une barrière de potentiel traverse l'anneau, donnant lieu à un lien faible, l'analogue du rf-SQUID: un anneau supraconducteur interrompu par une jonction Josephson, est crée par les atomes ultrafroids: un dispositif d'interférence quantique atomique (AQUID). L'intérêt de la création d'un analogue atomique du SQUID réside principalement dans les applications possibles dans le domaine de l'information quantique. Dans ce contexte, le SQUID a déjà été appliqué pour réaliser des qubits, et des états de superposition quantique macroscopiques, basés sur la superposition des états de courant.

La possibilité de réaliser des états de superposition macroscopique avec un AQUID a fait l'objet de plusieurs études théoriques récentes. Dans ce chapitre, je présente une étude systématique de la qualité du qubit dans un AQUID, dans le but d'identifier le meilleur régime de paramètres du système pour sa réalisation expérimentale. Nous considérons en particulier un gaz de Bose interagissant piégé dans un réseau optique en forme d'anneau unidimensionnel, en présence d'un potentiel de jauge effectif induisant un courant persistant, et d'une barrière de potentiel localisée. Nous avons établi dans une telle configuration l'émergence d'un système effectif à deux niveaux pour certaines valeurs du flux de jauge effectif, et nous avons étudié sa qualité, en termes de la difference d'energie interne entre les deux niveaux et leur séparation du reste du spectre, examinant la dépendance en fonction de la taille du système, la densité de bosons, l'interaction entre les particules et la force de la barrière. Nous avons également étudié la façon dont il est possible d'observer expérimentalement, par des mesures de la distribution d'impulsions, la superposition des états de circulation qui caractérisent les états du qubit.

En combinant des techniques analytiques et numériques, qui nous permet de couvrir tous les régimes physiques du système, nous avons montré qu'un réseau en anneau mésoscopique avec un faible barrière et des fortes interactions entre les atomes est le régime le plus favorable pour la mise en place et manipulation d'un qubit dans la prochaine génération d'expériences.

Chapter 4

Dipole excitation of a one-dimensional Bose gas in a split trap

4.1 Introduction

THE study of elementary excitations is a fundamental aspect of many-body theories. For neutral quantum fluids, these excitations at low energy correspond to sound waves for homogeneous systems and to inhomogeneous collective modes with discrete frequencies for confined ones. The analysis of the latter in ultracold quantum gases has been the subject of intense experimental [148–155] and theoretical [156–161] activity in the last decades. A variety of different excitation modes has been characterized, as the monopole (breathing), dipole (sloshing), quadrupole, and scissor modes, to cite the best known. An unprecedented precision has been reached in the measurement of their frequencies, becoming one of the most reliable tests for theoretical models and tools to investigate many-body phases [149, 162–164]. One of the most interesting aspects of these excitations is that their frequencies depend on the microscopic properties of the system, yielding information *e.g.* on the equation of state or on its superfluid properties.

The investigation of collective modes in ultracold quantum gases confined in low-dimensional geometries, in particular, has attracted a lot of theoretical [165–168] and experimental [26, 31, 40, 169] attention. In this chapter I present how, using a specific confining geometry, *i.e.* a split trap obtained by a localized barrier at the center of a quasi-one-dimensional harmonic trap, one can access the particularly rich interplay of

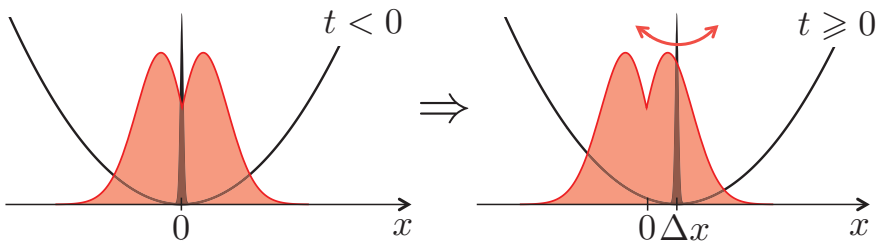

Figure 4.1: Sketch of the potential along the 1D waveguide. At $t = 0$ the potential is displaced by Δx to induce the dipole oscillation of the center of mass of the Bose gas.

effects due to interactions, transport through a potential barrier and quantum fluctuations, the effects of which are all enhanced in a low-dimensional geometry.

We focus on the dipolar excitation mode of a one-dimensional (1D) ultracold Bose gas, *i.e.* on the periodic oscillation of the center of mass of the atomic cloud, see the sketch in Fig. 4.1. In ultracold-gas experiments, this sloshing mode can be excited by a displacement of the center of the confining potential. A localized barrier can be created by microscope-focused laser beams [122] or by a light-sheet repulsive potential [170, 171]. For a purely harmonic potential, as predicted by Kohn's theorem [172, 173], the dipole mode has the same frequency as the harmonic trap for arbitrary interactions. In the presence of the barrier, instead, Kohn's theorem does not apply, and the situation becomes much more interesting. In our work we have found that the dipole mode displays an interaction-dependent frequency shift compared to the harmonic confining frequency, which allows to estimate directly the effective barrier strength seen by the fluid, yielding information on the classical screening of the barrier and on its renormalization due to quantum fluctuations. This effect generalizes the one found in Sec. 2.3 for the persistent current, to the case of an out-of-equilibrium, dynamical problem. We also find a surprising parity effect in the oscillation frequency, which becomes important in the strongly correlated phase, and that can be understood in terms of a fermionic rather than a bosonic transport process. The dipolar oscillation of the cloud realizes in fact a specific type of quantum transport across the barrier. The transport of correlated quantum fluids is more and more explored with ultracold atoms [174–176].

The results presented in this chapter are part of the original work of my PhD and are summarized in the fourth publication [19]. All the methods employed in this study, analytical and numerical, have been implemented by myself, and are detailed below in this section.

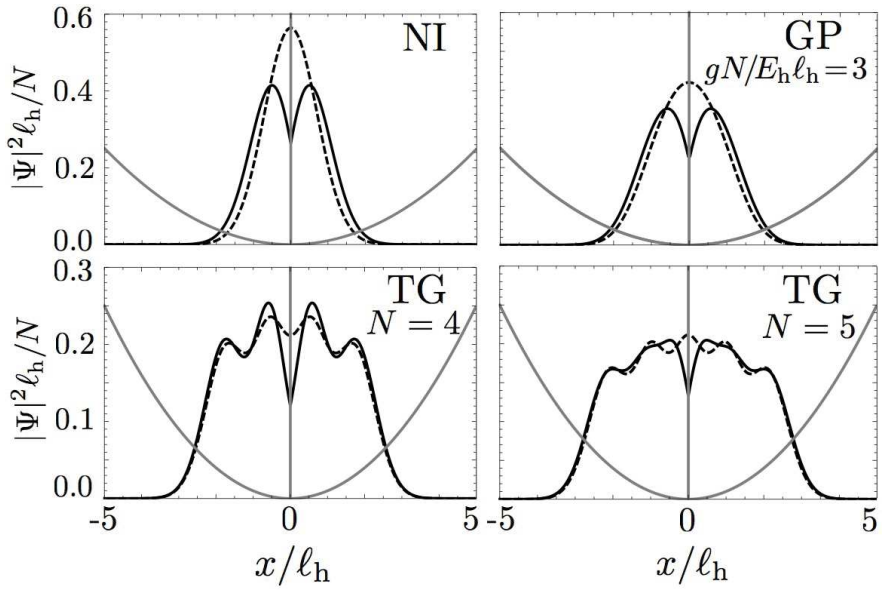

Figure 4.2: Ground state density for different interparticle interaction regimes and $U_0/E_h\ell_h = 0, 1$ (dashed and solid line respectively). In the TG case the barrier creates a notch in the density, in correspondence of a minimum or maximum, depending on whether the number of particles is even or odd. The grey line is a sketch of the potential in dimensionless units and divided by a factor of 50.

4.2 The model and the ground state

We consider a system of N bosons of mass m, confined in a 1D linear waveguide geometry at zero temperature. The bosons interact with each other via a contact interaction $V(x - x') = g\,\delta(x - x')$, and are subjected to the harmonic confinement $V_h(x) = \frac{1}{2}m\omega_h^2 x^2$ along the waveguide. The waveguide also contains a localized potential barrier at the center of the harmonic confinement, $V_b(x) = U_0\delta(x)$, which gives rise to a split trap for the particles, as the one sketched in Fig. 4.1. The corresponding system's Hamiltonian reads

$$\mathcal{H} = \sum_{j=1}^{N} -\frac{\hbar^2}{2m}\frac{\partial^2}{\partial^2 x_j} + U_0\delta(x_j) + \frac{1}{2}m\omega_h^2 x_j^2 + \frac{g}{2}\sum_{j,l=1}^{N}\delta(x_l - x_j)\,. \tag{4.1}$$

In Fig. 4.2 we show the effect of the localized barrier potential on the the ground state density profiles, for different interaction regimes. We notice that for increasing interactions the width of the density profile increases and, for very strong interactions, shell effects appear, as in a Fermi gas. The latter are readily explained by the Bose-Fermi mapping (see Sec. 1.2). Analogously to what is observed in a ring (see again

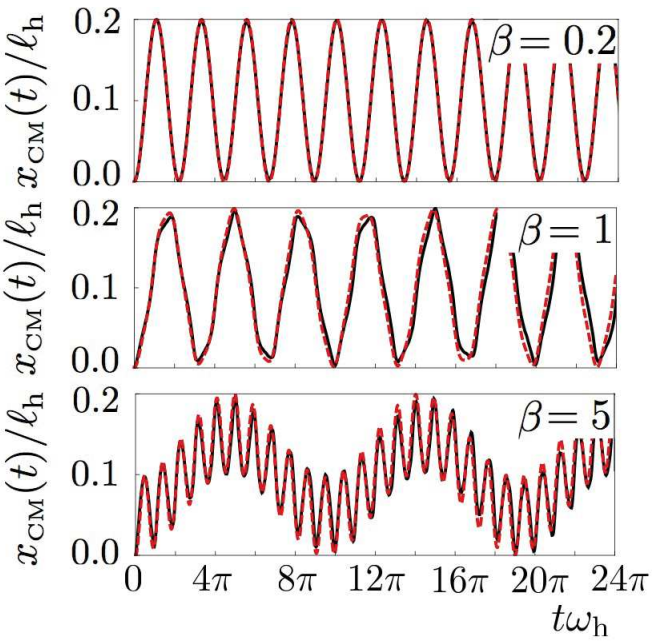

Figure 4.3: Time evolution of the center of mass position $x_{\rm CM}(t)$ for various values of barrier strength $\beta = U_0/E_{\rm h}\ell_{\rm h}$, with $E_{\rm h} = \hbar\omega_{\rm h}$, and for interaction strength $g = 0$. Solid black line: real-time evolution obtained from the numerical solution of the quench problem, red dashed line: estimate using the energy gaps of the many-body spectrum – a single frequency $(E_1 - E_0)/\hbar$ in the first panel, and an additional frequency for the second and third panel, weighted according to perturbation theory, Eq. (4.7).

Figs. 2.6), the effect of the barrier is to create a dip in the density profile, the size of which is governed by the healing length.

4.3 Dipole excitation

Starting from the ground state of the system in the split trap, we have studied the dynamics following a sudden quench of the harmonic and barrier potential positions, both being displaced at time $t = 0$ by a small amount $\Delta x \ll \ell_{\rm h}$, with $\ell_{\rm h} = \sqrt{\hbar/m\omega_{\rm h}}$ the characteristic harmonic oscillator length. The sudden displacement of the external potentials induces a collective excitation in the gas, whose center of mass (CM) starts to oscillate periodically in time around the new center of the trap, with a main frequency $\omega_{\rm d}$, hereafter referred as the dipole frequency, see the sketch in Fig. 4.1.

In the absence of the barrier ($U_0 = 0$), when only the harmonic confinement is present, the oscillation of the CM induced by the potential displacement is purely sinusoidal, with a dipole frequency that corresponds to the one of the harmonic confinement. This is a well-known result of Kohn's theorem [172, 173], that is specific to

the harmonic confinement, and is valid for arbitrary strength of the two-body interaction between the particles. It can be immediately understood from the separation of the CM degree of freedom from the internal ones for the harmonic confinement [41]. In the presence of the barrier ($U_0 > 0$), instead, the aforementioned separation of degrees of freedom can no longer be made, and, as we show in Fig. 4.3, we find the appearance of additional harmonics into the CM motion and a frequency shift of the fundamental dipole oscillation frequency with respect to the harmonic confining one. This frequency shift, and in particular its dependence on the interaction regime between the particles, is the main topic of the analysis presented in this chapter.

4.3.1 Dipole excitation frequency from many-body perturbation theory

In order to get a simple physical interpretation for the appearance of the additional harmonics entering the CM motion when the localized potential barrier is switched on, we have studied the excitation of the CM of the system applying perturbation theory. For $t < 0$ the system is assumed to be in its many-body ground state $|\Psi_0^{t<0}\rangle$ of the Hamiltonian $\mathcal{H}^{t<0}$ before the quench. In accordance with perturbation theory, we decompose the initial ground state into the eigenstates of the system after the quench

$$|\Psi_0^{t<0}\rangle = |\Psi_0^{t\geqslant 0}\rangle + \sum_{k=1}^{\infty} c_k |\Psi_k^{t\geqslant 0}\rangle \;, \tag{4.2}$$

where $\mathcal{H}^{t\geqslant 0}|\Psi_k^{t\geqslant 0}\rangle = E_k^{t\geqslant 0}|\Psi_k^{t\geqslant 0}\rangle$, and

$$c_k = \frac{\langle \Psi_k^{t\geqslant 0}|\mathcal{H}^{t<0} - \mathcal{H}^{t\geqslant 0}|\Psi_0^{t\geqslant 0}\rangle}{(E_0^{t\geqslant 0} - E_k^{t\geqslant 0})} \;. \tag{4.3}$$

Assuming a small displacement, $\Delta x \ll \ell_{\rm h}$, we have

$$\mathcal{H}^{t<0} \simeq \mathcal{H}^{t\geqslant 0} + \Delta x \sum_{j=1}^{N} \partial_{x_j} V_{\rm ext}^{t\geqslant 0}(x_j) + \mathcal{O}(\Delta x^2) \;, \tag{4.4}$$

where $V_{\rm ext} = \sum_{j=1}^{N} \frac{1}{2} m\omega_{\rm h}^2 x_j^2 + U_0 \delta(x_j)$, and therefore $\partial_{x_j} V_{\rm ext}^{t\geqslant 0}(x_j) = m\omega_{\rm h}^2 x_j + U_0 \delta'(x_j)$. The expectation value of the position of the center of mass as a function of time is given by

$$x_{\rm CM}(t) = \int_{-\infty}^{\infty} {\rm d}x \, x \, n(x,t) \;, \tag{4.5}$$

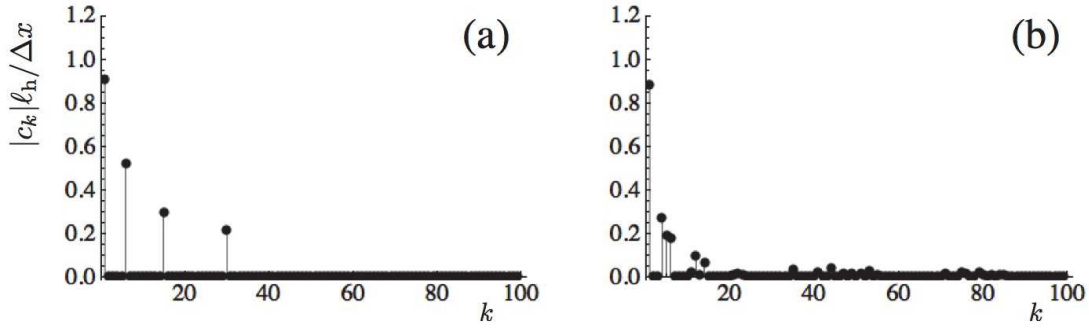

Figure 4.4: Absolute value of the matrix element c_k as a function of the quantum number k, for $\beta = U_0/E_h\ell_h = 1$, and different interparticle interaction strengths $g/E_h\ell_h = 0, 30$ (panel (a) and (b) respectively).

in terms of the density

$$n(x,t) = \int_{-\infty}^{\infty} \mathrm{d}x_1, \ldots, \mathrm{d}x_N \sum_{j=1}^{N} \delta(x - x_j) |\Psi_0^{t\geqslant 0}(x_1, \ldots, x_N, t)|^2 \,. \tag{4.6}$$

Perturbation theory thus yields

$$\begin{aligned} x_{\mathrm{CM}}(t) &= x_0 + \int_{-\infty}^{\infty} \mathrm{d}x\, x \int_{-\infty}^{\infty} \mathrm{d}x_1, \ldots, \mathrm{d}x_N \sum_{j=1}^{N} \delta(x - x_j) \\ &\quad \times \sum_{k=1}^{\infty} c_k \, 2\,\Re\mathrm{e}[\Psi_0^*(x_1, \ldots, x_N)\Psi_k(x_1, \ldots, x_N) e^{-i(E_k^{t\geqslant 0} - E_0^{t\geqslant 0})t/\hbar}] \,, \end{aligned} \tag{4.7}$$

where with x_0 we denote the unperturbed position of the CM in the displaced potential, *i.e.* $x_0 = \Delta x$. From this expression we see that the periodic oscillation of the center of mass motion is decomposed in a Fourier series at frequencies $(E_k^{t\geqslant 0} - E_0^{t\geqslant 0})/\hbar$, where the weight of each component depends on the coefficient c_k and the overlap integrals of the many-body wavefunctions $\Psi_0^*\Psi_k$.

In the absence of the barrier ($U_0 = 0$), we have checked by numerically diagonalizing the Hamiltonian $\mathcal{H}^{t\geqslant 0}$ (see Sec. 1.5 and 4.4.2 for details) that the only non vanishing matrix element c_k is the $k = 1$ one. Therefore the center of mass evolves at a single frequency

$$\omega_{\mathrm{d}} = \frac{(E_1^{t\geqslant 0} - E_0^{t\geqslant 0})}{\hbar} \,, \tag{4.8}$$

i.e. the dipole one, which we readily find to be $\omega_{\mathrm{d}} = \omega_{\mathrm{h}}$, since the eigenenergies of the Hamiltonian are those of the quantum harmonic oscillator, with a level spacing of $\hbar\omega_{\mathrm{h}}$, in agreement with Kohn's theorem.

In the presence of the barrier ($U_0 > 0$), the matrix elements c_k for $k > 1$ are instead in general non vanishing, and the dynamics of the CM is determined by more frequencies $(E_k^{t\geqslant 0} - E_0^{t\geqslant 0})/\hbar$. However, for small U_0, the contribution of the higher energy states with $k \geqslant 1$, gets less and less important, the most important contribution being the dipolar one. The dependence of the matrix element c_k on the quantum number k is shown in Fig. 4.4. The overlap integrals in Eq. (4.7) further decrease the weight of the higher-frequency components.

In conclusion, even in the presence of the barrier, we obtain that the sudden quench of the center of the trap excites mainly the dipole mode. The higher harmonics of the motion are also obtainable with this method, and well agree with the results of the exact time-evolution of the system, as shown in Fig. 4.3.

4.4 Barrier renormalization and parity effect

As I have anticipated above, in our study we have focused mainly on the dipole frequency shift produced by the barrier at various interparticle interaction regimes. The dipole frequency shift increases with the barrier strength, as is clearly visible in Fig. 4.3, and depends in a non trivial way on the interaction regime between the particles, as shown in Fig. 4.5(a, b). Indeed, for a weak barrier, the frequency shift directly reflects the effective strength of the barrier seen by the fluid. The effective barrier is maximally reduced for intermediate interactions as a consequence of the competition of classical screening of the barrier – occurring for weak interactions and increasing with the interaction strength, and barrier renormalization by the quantum fluctuations of the density – occurring for strong interactions and, being conjugate to phase fluctuations, decreasing for increasing interactions. Furthermore, we find that the frequency shift of the dipole mode in the strongly correlated regime depends on the particle number being even or odd, see again Fig. 4.5(a, b). This is particularly striking for a bosonic system, which does not display parity effects in other observables *e.g.* in the persistent currents [16, 116]. When the barrier potential is not placed at the center of the harmonic trap, the parity effect is still present, but it is modulated by the position of the barrier, as we show in Fig. 4.5(c). Remarkably, we find also that signatures of this mesoscopic effect remain visible at finite temperatures, Fig. 4.5(d).

In order to study the dipole frequency shift in all the regimes of interparticle interaction, we have resorted to a combination of analytical and numerical techniques suited for the 1D problem, that I detail below.

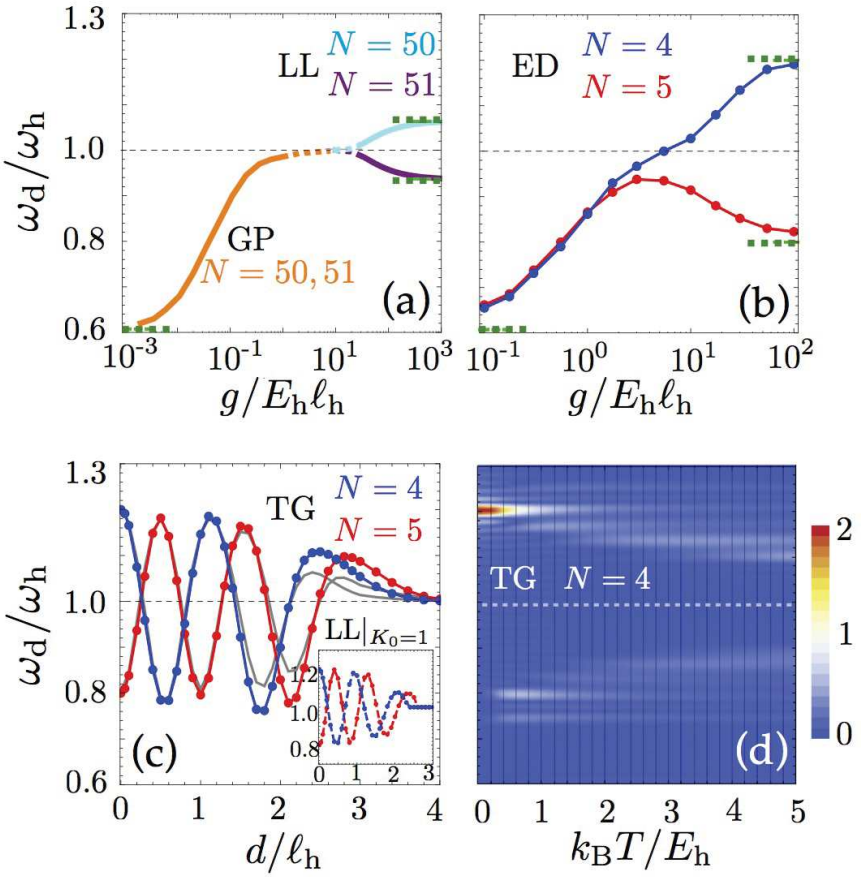

Figure 4.5: **(a, b)** Frequency of the dipole mode $\omega_{\rm d}$ as function of the interaction strength g for $\beta = U_0/E_{\rm h}\ell_{\rm h} = 1$, in different regimes: (a) GP and LL solution for $N = 50, 51$ (orange, cyan and purple lines respectively), the dotted lines at intermediate interactions are a guide to the eye in the regime beyond the validity of the GP and LL approaches; (b) ED solution for $N = 4, 5$ (blue and red respectively). The green dashed lines in the panels (a, b) correspond to the limiting cases of NI and TG gas ($g \to 0, \infty$). **(c)** Dependence of $\omega_{\rm d}$ on the position of the barrier d, for $g \to \infty$; calculated with the exact TG technique and corresponding LL for $K_0 = 1$ (inset, with the LDA density, and gray lines, using the exact TG density in Eq. (4.28)). **(d)** Density plot of the Fourier transform of the center of mass oscillation $|\Re{\rm e}[\delta x_{\rm CM}(\omega)]|$ as a function of frequency and temperature, in the TG limit, for $\beta = 1$ and $N = 4$.

4.4.1 Non-interacting and Tonks-Girardeau limits

In the two limiting cases of non-interacting (NI) and infinitely interacting or Tonks-Girardeau (TG) gas, we find an exact solution for the dynamical evolution of the gas. In both cases, starting from the analytical expression for the ground-state wavefunction $\Psi_0^{t<0}$ before the quench, that we can calculate by reducing the many-body problem to a single-particle one (see Sec. 1.2), we perform a numerical evolution of the

ground-state wave function in real-time $|\Psi_0^{t\geqslant 0}(t)\rangle = \exp(-i\mathcal{H}^{t\geqslant 0}t/\hbar)|\Psi_0^{t<0}\rangle$. The resulting time evolution of the position of the CM, $x_{\rm CM}(t) = \int_{-\infty}^{\infty} {\rm d}x\, x\, n(x,t)$, where $n(x,t)$ is the time-dependent gas density, is illustrated for instance in Fig. 4.3 for the NI case. A Fourier analysis of $x_{\rm CM}(t)$ shows that the center of mass motion is characterized by a main dipolar frequency, corresponding to the difference between the energy of the first excited many-body state and of the ground state of (4.1), $\omega_{\rm d} = (E_1 - E_0)/\hbar$, as well as by a higher harmonic with frequency $(E_3 - E_0)/\hbar$, in agreement with many-body perturbation theory (Sec. 4.3.1).

In the following we focus on the dipolar frequency $\omega_{\rm d}$. For the NI case, the N-particle ground-state energy is given by $E_0^{\rm NI} = N\varepsilon_0$, and the first excited one by $E_1^{\rm NI} = (N-1)\varepsilon_0 + \varepsilon_1$, where ε_j are the single particle energies, solutions of the one-body Schrödinger equation in the presence of harmonic and centred barrier potentials

$$\left[-\frac{\hbar^2}{2m}\partial_x^2 + U_0\delta(x) + \frac{1}{2}m\omega_{\rm h}^2 x^2\right]\psi_n = \varepsilon_n\psi_n \ . \tag{4.9}$$

In the TG case, the many-body energy spectrum coincides with the one of a free Fermi gas. In particular, the ground state energy is $E_0^{\rm TG} = \sum_{k=0}^{N-1}\varepsilon_k$ and the first excited state one is $E_1^{\rm TG} = \sum_{k=0}^{N-2}\varepsilon_k + \varepsilon_N$. Expressing all the quantities in units of the harmonic oscillator level spacing $E_{\rm h} = \hbar\omega_{\rm h}$ and characteristic length $\ell_{\rm h} = \sqrt{\hbar/m\omega_{\rm h}}$ we obtain the Schrödinger equation in the reduced form

$$\left[-\frac{1}{2}\partial_x^2 + \beta\delta(x) + \frac{1}{2}x^2\right]\psi_n = \varepsilon_n\psi_n \ , \tag{4.10}$$

where $\beta = U_0/E_{\rm h}\ell_{\rm h}$. The odd solutions ψ_{2n+1} of the quantum harmonic oscillator without barrier ($\beta = 0$), with $\varepsilon_{2n+1} = (2n+3/2)\hbar\omega_{\rm h}$, are still solutions of this equation with barrier, and having a node at the position of the barrier, they are independent of the strength of the barrier potential. The even solutions ψ_{2n}, instead, can be expressed in terms of Whittaker functions, after noticing that Eq. (4.10) for $x > 0$ corresponds to the differential equation for the parabolic cylinder functions [177, 178]:

$$\begin{aligned}
&\psi_{2n}(x) = \mathcal{N} D_{\varepsilon_n}(|x|) \ , \\
&D_{\varepsilon_n}(x) = \cos\left(\frac{\pi}{4} + \frac{\pi}{2}\varepsilon_n\right) Y_1 - \sin\left(\frac{\pi}{4} + \frac{\pi}{2}\varepsilon_n\right) Y_2 \ ,
\end{aligned} \tag{4.11}$$

where $\mathcal{N}$ is a normalization constant, and

$$\begin{aligned} Y_1 &= \frac{\Gamma\left(\frac{1}{4}-\frac{1}{2}\varepsilon_n\right)}{\sqrt{\pi}2^{\frac{1}{2}\varepsilon_n+\frac{1}{4}}}e^{-\frac{x^2}{2}}M\left(\frac{1}{2}\varepsilon_n+\frac{1}{4},\frac{1}{2},x^2\right) , \\ Y_2 &= \frac{\Gamma\left(\frac{3}{4}-\frac{1}{2}\varepsilon_n\right)}{\sqrt{\pi}2^{\frac{1}{2}\varepsilon_n-\frac{1}{4}}}e^{-\frac{x^2}{2}}\sqrt{2}xM\left(\frac{1}{2}\varepsilon_n+\frac{3}{4},\frac{3}{2},x^2\right) . \end{aligned}$$

Here, $M(...)$ is the confluent hypergeometric function and $\Gamma(...)$ is the Euler Gamma function. Imposing the cusp condition at the position of the barrier, $\partial_x\psi_n(0^+) - \partial_x\psi_n(0^-) = \beta\psi_n(0)$, we get the following expression for the eigenvalues ε_n:

$$\frac{\Gamma\left(\frac{3}{4}-\frac{1}{2}\varepsilon_n\right)}{\Gamma\left(\frac{1}{4}-\frac{1}{2}\varepsilon_n\right)} = -\frac{\beta}{2} . \tag{4.12}$$

We observe that for $\beta \to 0$ the energy eigenvalues ε_n tend to the even eigenvalues of the harmonic oscillator without barrier. In the opposite limit $\beta \to \infty$ they tend to the odd eigenvalues, that thus become doubly degenerate. The results for the dipole frequency in the NI and TG limits are shown in Fig. 4.5(a, b), while the corresponding ground-state densities are shown in Fig. 4.2.

The TG solution allows to readily get physical insight in the parity effect. Using perturbation theory in the barrier strength we have $\hbar\omega_{\rm d} = E_1^{\rm TG} - E_0^{\rm TG} = \hbar\omega_{\rm h} + \langle\Psi_1^{\rm TG}|\mathcal{H}_{\rm b}|\Psi_1^{\rm TG}\rangle - \langle\Psi_0^{\rm TG}|\mathcal{H}_{\rm b}|\Psi_0^{\rm TG}\rangle$, where $\mathcal{H}_{\rm b} = \sum_{j=1}^{N} U_0\delta(x_j)$. Using the explicit form of the ground- and first-excited many body wavefunction in the TG limit (see Sec. 1.2), $\Psi^{\rm TG}(x_1,...x_N) = \Pi_{1\le j<k\le N}\mathrm{sgn}(x_j-x_k)\det[\psi_n(x_\ell)]$, where $n = 0...N-1$ for the ground state and $n = 0...N-2, N$ for the first excited state, we readily obtain

$$\hbar\omega_{\rm d} = \hbar\omega_{\rm h} + U_0\left(|\psi_N(0)|^2 - |\psi_{N-1}(0)|^2\right) . \tag{4.13}$$

The single-particle orbitals $\psi_k(0)$ vanish for k odd and are finite for k even, therefore $\omega_{\rm d}$ is larger or smaller than $\omega_{\rm h}$ depending on the number of particles being even or odd. In analogy with transport phenomena in Fermi gases, for the strongly correlated (fermionized) bosons the dynamics of the gas at zero temperature is determined by the states at the (effective) Fermi level.

Scaling of the dipole frequency shift with number of particles – In Fig. 4.6 we show the scaling of the dipole frequency $\omega_{\rm d}$ on the number of particles N, as obtained from the TG exact calculation. For sufficiently large numbers of particles we find $|\omega_{\rm d} - \omega_{\rm h}| \propto 1/\sqrt{N}$. As I will show later in Sec. 4.4.4, this is a special case of a general power law behaviour predicted by the Luttinger liquid theory.

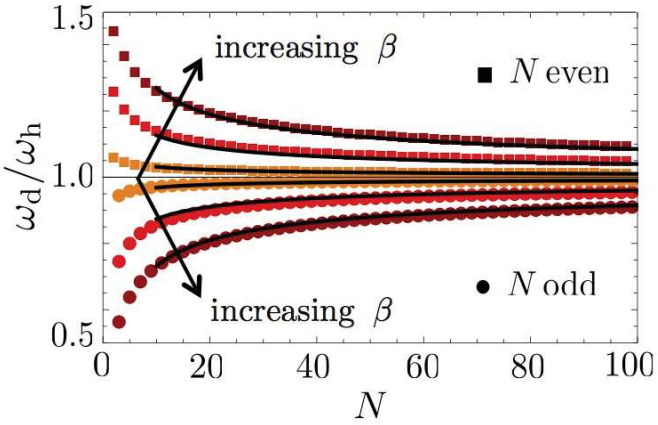

Figure 4.6: Scaling of ω_d as a function of the number of particles N in the TG regime. Different colors correspond to $\beta = U_0/E_h\ell_h = 0.2, 1$, and 5 (orange, red, and brown points respectively). For N sufficiently large ($N \gtrsim 10$) the scaling follows the power law $|\omega_d - \omega_h| \propto 1/\sqrt{N}$ (black solid lines).

Exact solution for a non-centred barrier – If the barrier is placed at a distance d from the center of the harmonic trap, it is still possible to calculate exactly the dipole frequency in the NI and TG limits, by solving the modified Eq. (4.9) with barrier potential $U_0\delta(x-d)$.

The one-body Schrödinger equation in the presence of harmonic and non-centred barrier potentials reads

$$\left[-\frac{\hbar^2}{2m}\partial_x^2 + U_0\delta(x-d) + \frac{1}{2}m\omega_h^2 x^2\right]\psi_n = \varepsilon_n\psi_n \ . \tag{4.14}$$

In this case the mirror symmetry $x \to -x$ of the system is broken, and the solutions do not have a well defined spatial symmetry. The solution can be written piecewise in the form [179]:

$$\psi_n(x) = \mathcal{N}_l\Theta(d-x)D_{\varepsilon_n}(-x) + \mathcal{N}_r\Theta(x-d)D_{\varepsilon_n}(x) \ , \tag{4.15}$$

where $\Theta(x)$ is the Heaviside function, $D_{\varepsilon_n}(x)$ are the parabolic cylinder functions defined in Eq. (4.11), and $\mathcal{N}_{l,r}$ are normalization factors. Imposing at the position of the barrier the condition of continuity $\mathcal{N}_l D_{\varepsilon_n}(-d) = \mathcal{N}_r D_{\varepsilon_n}(d)$, and the cusp condition $\partial_x\psi_n(d^+) - \partial_x\psi_n(d^-) = \beta\psi_n(d)$, and using the recursive relations for the derivatives of the parabolic cylinder functions [178], we obtain the trascendental equation for the energy eigenvalues:

$$\left(\varepsilon_n - \frac{1}{2}\right)\left(D_{\varepsilon_n-1}(-d)D_{\varepsilon_n}(d) + D_{\varepsilon_n-1}(d)D_{\varepsilon_n}(-d)\right) = \sqrt{2}\beta D_{\varepsilon_n}(-d)D_{\varepsilon_n}(d) \ . \tag{4.16}$$

As shown in Fig. 4.5(c), in this case the parity effect is modulated, displaying an oscillating behaviour as a function of d.

4.4.2 Numerical exact diagonalization

To cover all the interaction strength regimes, for small numbers of particles, we have adopted a numerical method based on the exact diagonalization (ED) of Hamiltonian (4.1): we calculate the low-energy eigenspectrum of the many-body system, and obtain the dipole mode frequency as $\omega_{\rm d} = (E_1 - E_0)/\hbar$. Details on this technique are given in Sec. 1.5. To represent Hamiltonian (4.1) we have chosen the N-particle basis built using the single-particle eigenfunctions of Eq. (4.9), which have been detailed in Sec. 4.4.1 above. The truncation of the Hilbert space to a number S of single-particle states is the only approximation performed with this technique. Since the dimension of the Hilbert space rapidly grows with S and the particle number N, we are limited to small N. In our calculations we have considered up to $N = 5$ and $S = 18$. To improve the estimate of the eigenspectrum obtained with the truncated Hilbert space we have also performed a finite-size scaling varying the number of single particle states. The ED results for the dipole frequency are shown in Fig. 4.5(b).

4.4.3 Mean-field Gross-Pitaevskii equation

For larger values of the particle number we adopt complementary approximate approaches. In the regime of weak interactions, we describe the fluid as a Bose-Einstein condensate by means of the Gross-Pitaevskii (GP) equation, see Sec. 1.3.

$$\left[-\frac{\hbar^2}{2m}\partial_x^2 + U_0\delta(x) + \frac{1}{2}m\omega_{\rm h}^2 x^2 + g|\Phi|^2\right]\Phi = \mu\Phi \ , \tag{4.17}$$

where $\Phi(x)$ is the condensate wave function and μ the chemical potential. We integrate this equation in imaginary time to find its ground state solution, as explained in Sec. 1.3, the ground-state density in the weak interaction regime is shown in Fig. 4.2. Subsequently, we evolve the ground state in real time with shifted potential, to calculate the time evolution of the position of the CM after the quench, as for the NI and TG cases. The frequency of the dipole mode is thus found through a Fourier analysis of the time-evolution of the CM position, which is obtained as $x_{\rm CM}(t) = \int_{-\infty}^{\infty} {\rm d}x\, x|\Phi(x,t)|^2$, and is shown in Fig. 4.5(a). We find that in the weak interaction regime, the dipole frequency shift decreases monotonically with the interaction strength g. This can be understood in terms of classical screening of the barrier, quantified by the healing length $\xi = \hbar/\sqrt{2mgn}$, that decreases at increasing interaction strength.

4.4.4 Luttinger liquid approach

In the strongly interacting regime we take into account the effect of quantum fluctuations using the Luttinger liquid (LL) theory, introduced in Sec. 1.4. The presence of the smoothly varying harmonic potential is taken into account within the local density approximation (LDA), *i.e.* expressing the equation of state of the inhomogeneous system as a functional of the local density $n(x)$. The effective LL Hamiltonian for the inhomogeneous system then reads [50,180]

$$\mathcal{H}_0 = \frac{\hbar}{2\pi}\int_{-\infty}^{\infty} \mathrm{d}x \ \left[v_s(x)K(x)(\partial_x\phi(x))^2 + \frac{v_s(x)}{K(x)}(\partial_x\theta(x))^2 \right] , \tag{4.18}$$

where $\theta(x)$ and $\phi(x)$ are canonically conjugate fields, corresponding to density fluctuations above the equilibrium density $n(x)$ and phase respectively. The local Luttinger parameter $K(x)$ and the sound velocity $v_s(x)$ depend on the microscopic interaction strength g, and are determined in LDA according to $v_s(x)K(x) = \hbar\pi n(x)/m$, and $v_s(x)/K(x) = \partial_n\mu(n(x))/\hbar\pi$, see Sec. 1.4.

In order to diagonalize the inhomogeneous LL Hamiltonian (4.18), we have introduced, in analogy to what is done for the quantum harmonic oscillator, the bosonic conjugate fields b_j and $b_j^\dagger$ in the following way:

$$\begin{aligned} \partial_x\phi(x,t) &= \sum_{j=0}^{\infty} i\sqrt{\frac{m\omega_j}{2\hbar n(x)}}\left(\varphi_j(x)e^{i\omega_j t}b_j^\dagger - \varphi_j^*(x)e^{-i\omega_j t}b_j\right) , \\ -\frac{\theta(x,t)}{\pi} &= \sum_{j=0}^{\infty}\sqrt{\frac{\hbar n(x)}{2m\omega_j}}\left(\varphi_j(x)e^{i\omega_j t}b_j^\dagger + \varphi_j^*(x)e^{-i\omega_j t}b_j\right) ; \end{aligned} \tag{4.19}$$

such that the canonical commutation relation $[-\theta(x)/\pi, \partial_{x'}\phi(x')] = i\delta(x-x')$ and the orthogonality relation $\int \mathrm{d}x\varphi_j^*(x)\varphi_l(x) = \delta_{j,l}$ imply that $[b_j, b_l^\dagger] = \delta_{j,l}$. Hamiltonian (4.18) is then diagonal in terms of the b_j and $b_j^\dagger$ fields,

$$\mathcal{H}_0 = \sum_{j=0}^{\infty}\hbar\omega_j\left(b_j^\dagger b_j + \frac{1}{2}\right) , \tag{4.20}$$

provided that the modes' wavefunctions $\varphi_j(x)$ satisfy the differential equation

$$-\omega_j^2\sqrt{v_s(x)K(x)}\varphi_j(x) = v_s(x)K(x)\partial_x\left(\frac{v_s(x)}{K(x)}\partial_x(\sqrt{v_s(x)K(x)}\varphi_j(x))\right) . \tag{4.21}$$

The spatial dependence of the parameters K and v_s can be determined in LDA, assuming an equation of state of the form $\mu(n) = \eta n^\nu$ [166,180]: this connects the GP regime,

where $\mu(n) = gn$, and TG regime, where $\mu(n) = (\hbar^2\pi^2/2m)n^2$. The parameters η and ν can be obtained from the Bethe ansatz solution of the homogeneous Lieb-Liniger model [181]. In the LDA, we get from the equation of state the following expression for the density: $n(x) = [\eta(\mu - V_{\rm h}(x))]^{1/\nu}$, where $V_{\rm h}(x) = m\omega_{\rm h}^2 x^2/2$ and $\mu = m\omega_{\rm h}^2 R^2/2$, where R is the Thomas-Fermi radius which is determined from the normalization condition $N = \int_{-R}^{R} {\rm d}x\, n(x)$. This yields the expressions $K(x) = K_0(1-x^2/R^2)^{1/\nu-1/2}$, and $v_s(x) = v_0\sqrt{1-x^2/R^2}$, with $v_0 = \sqrt{\nu/2}\omega_{\rm h}R$, and $K_0 = \sqrt{(\partial\mu/\partial n)|_{TG}/(\partial\mu/\partial n)|_{x=0}} = \sqrt{\hbar^2\pi^2 n(0)^{2-\nu}/m\eta\nu}$. The dependence on the interaction strength of such Luttinger parameters is known (see Eqs. (1.26), (1.27) and Fig. 1.7); in particular in the TG limit $K_0 = 1$ and $v_s = v_F$, the Fermi velocity of the fermionized Bose gas. Eq. (4.21) has an analytical solution [178,180]:

$$\begin{aligned} \varphi_j(x) &= \sqrt{\frac{j!(j+1/\nu+1/2)}{R\pi\Gamma(j+2/\nu+1)}}\, 2^{1/\nu}\Gamma(1/\nu+1/2)C_j^{1/\nu+1/2}(x/R)\ , \\ (\omega_j/\omega_{\rm h})^2 &= (j+1)(1+j\nu/2)\ , \end{aligned} \tag{4.22}$$

where $C_j^a(...)$ is the Gegenbauer polynomial and $\Gamma(...)$ is the Euler Gamma function. We notice immediately that the lowest eigenvalue $j = 0$, that corresponds to the frequency ω_0 of the dipole mode ($j = 0$), is given by $\omega_{\rm h}$ for any interaction strength, in agreement with Kohn's theorem.

Let us consider now how the barrier term of the Hamiltonian $\mathcal{H} = \mathcal{H}_0 + \mathcal{H}_{\rm b}$, affects the frequency of the dipole mode of $\mathcal{H}_0$ The barrier, located for the sake of generality at position d, yields a non-linear contribution to the Luttinger liquid Hamiltonian of the form $\mathcal{H}_{\rm b} = \int_{-\infty}^{\infty} {\rm d}x\, U_0\delta(x-d)\rho(x)$. Such a localized barrier potential induces a very rapid spatial variation of the confinement, hence cannot be taken into account in the LDA description of $\mathcal{H}_0$. We treat its effect perturbatively in the limit of weak barrier strength. Keeping only the lowest harmonics $l = \pm 1$ in the density field expansion $\rho(x) = [n(x) + \partial_x\theta(x)/\pi]\sum_{l=-\infty}^{+\infty} e^{i2l\theta(x)+i2l\pi\int_{-\infty}^{x}{\rm d}x' n(x')}$, see Eq. (1.32), we obtain as the most dominant term

$$\mathcal{H}_{\rm b} \simeq 2U_0 n(d)\cos\left[2\theta(d) + 2\pi\int_{-\infty}^{d} {\rm d}x\, n(x)\right]\ . \tag{4.23}$$

Since we are interested only in the dipole excitation mode, if the barrier strength is small compared to the characteristic energy of the dipole mode ($U_0/\ell_{\rm h} < \hbar\omega_{\rm d}$), we can integrate out all the higher modes, $j \geqslant 1$. Considering the Fourier decomposition of the field $\theta(x,t) = \sum_{j=0}^{\infty} e^{-i\omega_j t}\theta_j(x)$, we decompose the cos potential of the sum, and taking the zero-temperature average over the vacuum of excitations, we obtain a renormalization of the barrier strength by density quantum fluctuations

$U_{\rm eff} = U_0\langle 0|\cos(2\sum_{j=1}^{\infty}\theta_j(d))|0\rangle$. We define $\langle 0|\cos(2\sum_{j=1}^{N/c}\theta_j(d))|0\rangle = \exp[-2G(d)]$, where $G(d) = \langle 0|(\sum_{j=1}^{N/c}\theta_j(d)))^2|0\rangle$. The LL being an effective low-energy field theory, the sum over the modes can not extend up to infinity, but should stop at a certain cut-off j_c, that is intrinsic to the effective theory and that can not be determined within the theory itself. In our calculations we take it to be proportional to the Fermi energy [1], thus j_c is proportional to the number of particles $j_c = N/c$, up to some numerical factor c of order 1. The latter is fixed imposing the matching between the LL solution and the exact TG one in the infinitely strong interaction limit, $K_0 \to 1$. Thus, in general, the effective renormalized barrier strength for the lowest mode is given by

$$U_{\rm eff}(d) = U_0 e^{-2G(d)} \ . \tag{4.24}$$

Using the mode decompositions (4.19), the local two point correlation function for $\theta(x)$ takes the form $G(d) = (\pi/2)K(d)v_s(d)\sum_{j=1}^{N/c}(1/\omega_j)|\varphi_j(d)|^2$. In the particular case where the barrier is at the center of the trap and for large particle numbers we find

$$U_{\rm eff}(0) = U_0\left(\frac{a}{N}\right)^{\kappa} \ , \tag{4.25}$$

where $\kappa = K(0)v_s(0)/\omega_{\rm h}R = K_0\sqrt{\frac{\nu}{2}}$, and a is a non-universal parameter dependent on the cut-off of the effective LL theory [2]. Having integrated out the higher modes and consequently renormalized the barrier strength, we can rewrite the barrier term of the Hamiltonian in terms only of the field θ_0, as

$$\mathcal{H}_{\rm b} \simeq 2U_{\rm eff}(d)n(d)\cos\left[2\theta_0(d) + 2\pi\int_{-\infty}^{d}{\rm d}x\, n(x)\right] \ . \tag{4.26}$$

Upon a Taylor expansion for small θ_0 to second order, substituting Eq. (4.19) for the field θ_0, and neglecting constant contributions to the Hamiltonian, we get the final, diagonal, expression:

$$\mathcal{H}_{\rm b} \simeq 2n(d)U_{\rm eff}(d)\pi v_s(d)K(d)\varphi_0^2(d)\omega_{\rm h}^{-1}\cos\left[2\pi\int_{-\infty}^{d}{\rm d}x\, n(x)\right]\left(b_0^{\dagger}b_0 + {\rm H.c.}\right) \ . \tag{4.27}$$

This, after substituting the analytical expression of φ_0 given by Eq. (4.22), leads to the expression for the shift of the dipole mode frequency:

$$\omega_{\rm d} - \omega_{\rm h} = \frac{n(d)U^{\rm eff}(d)K(d)v_s(d)}{\hbar\omega_{\rm h}R}f(\nu)\cos\left(2\pi\int_{-\infty}^{d}{\rm d}x\, n(x)\right) \ , \tag{4.28}$$

[1] Here we chose the cutoff of the strongly interacting regime; in general j_c is interaction-dependent.
[2] We have used as an estimate for a its value in the TG limit, accessible through the exact solution.

where $f(\nu) = (\frac{1}{\nu}+\frac{1}{2})\Gamma^2(\frac{1}{\nu}+\frac{1}{2})2^{\frac{2}{\nu}+2}/\Gamma(\frac{2}{\nu}+1)$. The integral of the density gives rise to an oscillating term as a function of d, as shown in Fig. 4.5(c), which reduces to $(-1)^N$ for $d = 0$. This explains the parity-dependent frequency shift of the dipole mode. In the case of a centred barrier ($d = 0$), this expression simplifies to

$$\omega_{\rm d} - \omega_{\rm h} = (-1)^N n(0) U_0 \left(\frac{a}{N}\right)^{\kappa} K_0 \sqrt{\frac{\nu}{2}} \frac{1}{\hbar} \left(\frac{(\frac{1}{\nu}+\frac{1}{2})\Gamma^2(\frac{1}{\nu}+\frac{1}{2})2^{\frac{2}{\nu}+2}}{\Gamma(\frac{2}{\nu}+1)} \right) . \qquad (4.29)$$

We have used Eq. (4.29) to estimate the interaction-dependent frequency shift of the dipole mode in Fig. 4.5(a). For repulsive interactions the effective barrier strength is smaller than the bare one, since $\kappa \geqslant 1$, and decreases as the interaction strength is decreased from infinite to intermediate values ($\kappa \to 1$ for $g \to \infty$, and $\kappa \to \infty$ for $g \to 0$), which explains that $\omega_{\rm d}$ approaches $\omega_{\rm h}$ when decreasing the interaction strength. This is consistent with the larger suppression of density fluctuations for strong interactions expected from the Luttinger power-law behaviour of the density-density correlation function $\langle \rho(x)\rho(x')\rangle \propto |x-x'|^{-2K}$ [49, 50]. Finally, we notice that in the TG limit one has $\kappa = 1$ and $n^{\rm TG}(0) = (1/\ell_{\rm h})\sqrt{2N/\pi}$ in LDA; thus we find the scaling law $|\omega_{\rm d} - \omega_{\rm h}| \propto 1/\sqrt{N}$ for the dipole frequency shift, which in Fig. 4.6 is shown to be in excellent agreement with the TG exact solution.

4.4.5 Temperature effects

The analysis presented in the previous section refers to a system at zero temperature. Because of the relevance of thermal effects in realistic experimental situations, we have performed an exact finite-temperature calculation in the TG limit, see Fig. 4.5(d). Interestingly, the main features of the dipole-mode frequency shift remain visible at finite temperatures, even if for temperatures $k_{\rm B}T \gtrsim \hbar\omega_{\rm h}$ thermal fluctuations mix the characteristic zero-temperature frequencies of odd and even number of particles. As it is shown below, this can be understood in terms of smearing of the effective TG fermionic distribution function.

TG real time evolution – We have obtained the oscillation spectrum at finite temperature shown in Fig. 4.5(d) by performing a Fourier analysis of the time evolution of the position of the CM, $x_{\rm CM}(t) = \int_{-\infty}^{\infty} {\rm d}x\, x\ n_T(x,t)$, where the density at finite temperature is given by $n_T(x,t) = \sum_{j=0}^{\infty} f(\varepsilon_j)|\psi_j(x,t)|^2$, with $f(\varepsilon)$ the Fermi distribution function at finite temperature for a state of energy ε, ε_j the single particle energies determined in Section 4.4.1, and $\psi_j(x,t)$ the time dependent single particle wave functions determined by numerically evolving in real time the exact initial-state wave functions determined in Section 4.4.1 with the Hamiltonian $\mathcal{H}^{t\geqslant 0}$.

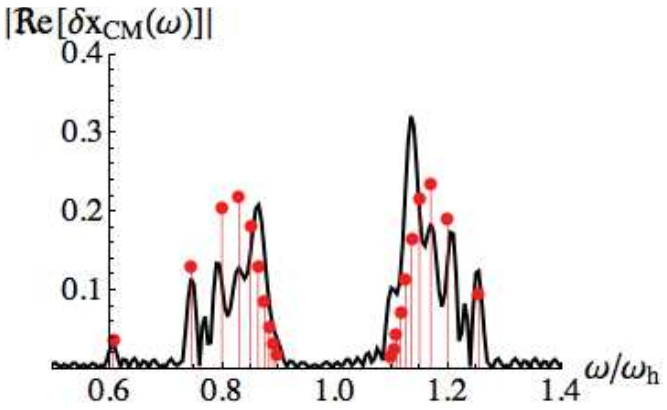

Figure 4.7: Fourier transform of the center of mass oscillation $|\Re\mathrm{e}[\delta x_{\rm CM}(\omega)]|$ as a function of frequency, in the TG limit obtained with the Fourier transform of the real-time evolution (black solid line) and from linear response theory (red vertical lines with dots).

Linear response theory – The dynamics of the center of mass of the system can also be analysed, in the limit of small oscillation amplitude, through linear response theory. This allows to obtain the time evolution of the particle density $n(x,t) = \langle \rho(x,t) \rangle$, where ρ is the density operator, in response to the perturbation operator $\mathcal{H}_{\rm p} = \int_{-\infty}^{\infty} {\rm d}x V_{\rm p}(x,t)\rho(x)$ where $V_{\rm p}(x,t) = \Theta(t)\Delta x \partial_x V_{\rm ext}^{t\geqslant 0}(x)$, and $\Theta(t)$ is the Heaviside function, see Sec. 4.3.1. Within the framework of linear response theory the corresponding evolution is then given by

$$\langle \rho(x,t) \rangle = \langle \rho^I(x,t) \rangle + \int_{-\infty}^{\infty} {\rm d}x' \int_{-\infty}^{\infty} {\rm d}t' \chi(x,x';t-t') V_{\rm p}(x',t') \; , \tag{4.30}$$

where $\chi(x,x';t,t') = (1/i\hbar)\Theta(t-t')\langle [\rho^I(x,t), \rho^I(x',t')] \rangle$ is the response function, and $\rho^I(x,t) = e^{i\mathcal{H}^{t\geqslant 0}t/\hbar}\rho(x)e^{-i\mathcal{H}^{t\geqslant 0}t/\hbar}$ gives the unperturbed evolution of the density operator. Recalling that the center of mass position is given by $x_{\rm CM}(t) = \int_{-\infty}^{\infty} {\rm d}x \; x \langle \rho(x,t) \rangle$, we readily obtain in Fourier space $\delta x_{\rm CM}(\omega) = \int_{-\infty}^{\infty} {\rm d}x \; x \int {\rm d}x' \; \chi(x,x';\omega) V_{\rm p}(x',\omega)$, with

$$\begin{aligned} \chi(x,x';\omega) \;\; &= \;\; \frac{1}{\hbar Z(\beta)} \sum_{n \neq m} \langle m|\rho(x)|n\rangle\langle n|\rho(x')|m\rangle e^{-\beta E_m} \\ &\times \left(\frac{1}{(\omega - (E_n - E_m)/\hbar) + i0^+} - \frac{1}{(\omega + (E_n - E_m)/\hbar) + i0^+} \right). \end{aligned} \tag{4.31}$$

Here, $Z(\beta) = \sum_m e^{-\beta E_m}$, $\beta = 1/k_{\rm B}T$, n and m denote the many-body states.

In the TG limit the density-density response function coincides with the one of a

non-interacting Fermi gas, and Eq. (4.31) simplifies to [182]:

$$\begin{aligned}\chi(x,x';\omega) &= (1/\hbar)\sum_{j\neq k}\psi_j^*(x)\psi_k(x)\psi_k^*(x')\psi_j(x')f(\varepsilon_j)[1-f(\varepsilon_k)] \\ &\times \left(\frac{1}{(\omega-(\varepsilon_k-\varepsilon_j)/\hbar)+i0^+}-\frac{1}{(\omega+(\varepsilon_k-\varepsilon_j)/\hbar)+i0^+}\right). \quad (4.32)\end{aligned}$$

In Fig. 4.7 we show the comparison between the oscillation spectrum at finite temperature in the TG case obtained with the real-time evolution, as explained above, with the linear response theory approach. The results obtained with the two methods agree quite well, which is remarkable given the finite simulation time used for the real-time evolution calculation that smears the frequency peaks.

4.5 Conclusion

In this chapter I have presented our study of an interacting, one-dimensional Bose gas confined in a split trap, obtained by an harmonic potential with a localized barrier at its center. In particular, as a prototype of quantum transport phenomena, we have studied the dipolar oscillations of the gas across the barrier, induced by a sudden quench of the position of the center of the trap. We have found that the main frequency of the dipole oscillation strongly depends on the interaction strength between the particles, allowing to determine the effective barrier strength seen by the fluid, and thus yielding information on the classical screening of the barrier and on its renormalization due to quantum fluctuations. The full quantum solution also displays a peculiar parity effect, due to the combination of fermionic transport properties for the correlated Bose gas and the harmonic trap geometry. Observation of this parity effect and of the shift of the dipole frequency with the interaction strength would provide a unambiguous evidence of the effect of quantum fluctuations.

A characterization of the full dynamics of the system shall include damping. Its study, which is beyond the scope of the present work since its contribution is negligible in the linear response regime we have considered, should include several sources of dissipation, such as quantum phase slips, phonon emission due to mode coupling and anharmonicities beyond the LL description. Numerical and experimental studies have been done in this direction [31, 161, 175, 183].

Résumé du chapitre

Excitation de dipole d'un gaz de bosons unidimensionnels dans un piège à double puits

L'étude des excitations élémentaires est un aspect fondamental des théories à plusieurs corps. Pour les fluides quantiques neutres, ces excitations à basse énergie correspondent à des ondes sonores pour les systèmes homogènes, et à des modes collectifs avec des fréquences discrètes pour ceux confinés. L'analyse de ces derniers dans les gaz quantiques ultrafroids a été l'objet d'une intense activité de recherche expérimentale et théorique au cours des dernières décennies, et une précision sans précédent a été atteinte dans la mesure de leurs fréquences. Un des aspects les plus intéressants de ces excitations est que leurs fréquences dépendent des propriétés microscopiques du système, ce qui donne des informations par exemple sur son équation d'état ou sur ses propriétés de superfluidité.

Dans ce chapitre, je présente notre étude d'un gaz de Bose unidimensionnel en interaction, dans un piège à double puits, obtenu par un potentiel harmonique avec une barrière localisée en son centre. En particulier, comme un prototype des phénomènes de transport quantique, nous avons étudié les oscillations dipolaires du gaz à travers la barrière induites par un deplacement istantané de la position du centre du piège.

En appliquant plusieurs méthodes analytiques et numériques valables dans différents régimes d'interaction entre les particules, nous avons trouvé que la fréquence principale de l'oscillation du dipole dépend fortement de la force d'interaction entre les particules, ce qui permet de déterminer la hauteur effective de la barriere vue par le fluide, et d'obtenir ainsi des informations sur l'écrantage classique de la barrière ainsi que sur sa renormalisation due aux fluctuations quantiques. La solution exacte de ce problème montre également un effet de parité particulière qui consiste en une fréquence d'oscillation du dipole qui dépend de la parité du nombre de particules. Ceci peut être expliqué en rappelant que un gaz de bosons en fortes repulsions a les mêmes propriétés de transport qu' un gaz des fermions. L'observation de cet effet de parité et la dépendance de la fréquence du mode de dipole avec la force des interactions constituerait une preuve sans équivoque de l'effet des fluctuations quantiques.

Conclusions and perspectives

In this thesis I have presented our study of a few mesoscopic quantum systems constituted by a one-dimensional (1D) ultracold Bose gas. These systems are relevant both for the study of fundamental properties of quantum fluids and, thanks to their high degree of experimental control and tunability, also in view of the future realization of atomic-based quantum devices *e.g.* in the field of quantum computation. In particular, we have studied the behaviour of these systems for various regimes of interaction strengths between the particles. In order to do so, we have applied a combination of several theoretical techniques, based on different approximations valid in different physical regimes, such as the mean-field Gross-Pitaevskii desprition for weak interactions, the Luttinger liquid effective theory for strong interactions, the Tonks-Girardeau exact solution in the infinitely strong interactions limit and numerical simulations based on density-matrix renormalization group and exact diagonalization algorithms in the intermediate regimes. In particular we have focused on the interplay of effects arising from the presence in such systems of interactions, quantum fluctuations and localized potential barriers, whose contributions are all enhanced in 1D compared to higher-dimensions.

In the second chapter of the thesis I have presented our study of the persistent currents phenomenon for interacting 1D bosons on a ring trap. The current is induced as a consequence of the Aharonov-Bohm effect by the presence of a rotating barrier potential, as in recent experiments with atomic condensates stirred by a laser beam on toroidal confinements. We provide a complete characterization of the persistent current for a ring of mesoscopic size and particle number, in all the interaction and barrier strength regimes. In particular, we disclose the presence of an optimal regime, for intermediate interaction strength, in which the amplitude of the persistent current is maximal. This is due to a non-monotonic screening effect of the barrier by the fluid, due to the competition between the tendency of a classical bosonic field to screen the

barrier more and more as interactions are increased, and the effect of quantum fluctuations that screen the barrier less and less going towards the strongly correlated regime. Furthermore, we have studied the scaling properties of the persistent current amplitude with the system size. Despite the fact that the persistent current is overall a mesoscopic phenomenon, which vanishes for an infinite system in the thermodynamic limit, we have found that the scaling of the current amplitude depends also non-monotonically on the interaction strength, displaying an optimal regime for intermediate interactions in which the persistent current amplitude decreases slower with the system size than for very large or very small interaction strengths.

In the third chapter I have presented our study of a system of bosonic atoms loaded in a ring-shaped 1D optical lattice, in the presence of a localized potential barrier, and an artificial gauge potential inducing a persistent current. This system represents an ultracold atoms analogue of the rf-SQUID, namely an atomtronic quantum interference device (AQUID), which is currently under investigation for the realization of flux-qubits based on the superpositions of circulation states. We have performed a systematic analysis of this system in order to identify the best parameter regime for the realization and addressability of a flux-qubit. In particular, we have studied the resolution of the qubit, the scaling properties of its energy gap, and its detectability from time-of-flight measurements of the momentum distribution. This allowed us to identify the regime of mesoscopic size (tens of lattice sites) for a sufficiently correlated gas in the presence of a weak barrier as the best suited for the resolution and addressability of the qubit with a sufficient number of particles for experimental implementations. At the same time, the best regime for the detection of the superposition of circulation states through the momentum distribution corresponds to the case in which the barrier is less screened by the bosonic fluid.

In the fourth chapter I have presented our study of an interacting, one-dimensional Bose gas confined in a split trap, obtained by a harmonic potential with a localized barrier at its center. A sudden quench of the position of the center of the trap induces an oscillation of the center of mass of the gas across the barrier, thus realizing a particular type of quantum transport phenomena. We have studied how the main frequency of this dipole excitation depends on the interaction strength between the particles for a mesoscopic system of a finite number of particles, thus obtaining information on the effective barrier seen by the fluid. Furthermore, we disclosed a peculiar parity dependence of the dipole frequency in the strongly correlated regime, due to the combination of fermionic transport properties of the Bose gas and the harmonic trap geometry.

As a recurring theme in all these systems, we have disclosed the important effects of screening and renormalization of localized potential barriers in a 1D bosonic system, due to the combination of the effects of interparticle interactions and quantum fluctuations. The presence of this screening, and in particular of a regime unknown so-far for intermediate interaction strength where it is maximized, has important consequences for the physics of the systems we have considered, affecting various physical observables, both at- and out-of-equilibrium. This behaviour needs to be taken into account in the design of future atomtronic quantum devices. Lastly, this phenomenon is very general, and we expect it to have an impact also on different situations from those considered by us, such as in the study of the motion of localized impurities through quantum fluids, just to cite one example.

Most of the problems considered in this thesis allow for a number of possible developments. Concerning the persistent currents it would be interesting to study via time-dependent exact solutions and DMRG simulations the effect on the current dynamics of an out-of-equilibrium and time-dependent driving of the barrier potential. In this way realistic experimental protocols of state preparation and setting into motion of the system could be fully taken into account. The study of the flux-qubit could be completed by further investigations of the superposition of circulations states, for instance by quantifying the amount of entanglement of the superposition. Also, in view of quantum computation applications, the effect of decoherence due to particle losses and the sensitivity to experimental inaccuracies should be analysed in detail. Regarding the dipole excitations, it would be interesting to study damping effects in the system dynamics, which can be induced by large displacement of the trap and by the presence of anharmonicities accounting for phonon interactions.

In my opinion, in the next years the experimental progress in the micro-fabrication of optical circuits for ultracold gases will lead to a boost in the development of quantum technologies, which are currently advancing towards realistic applications *e.g.* in the fields of quantum metrology and quantum information, and will provide the most accurate platform to investigate fundamental aspects of quantum many-body theory. From the technological point of view, the coupling of several atomtronics circuits like the ones considered in this thesis opens for the possibility to build coupled-qubit systems and quantum logic gates. From a fundamental point of view, these systems provide a clean quantum simulator for investigating the features of macroscopic quantum superposition states such as Scrödinger-cat-like states, and their quantum information properties. Furthermore, the study of the dimensional crossover of these systems, from 1D to higher dimensions, should help us to better understand superfluid properties of quantum fluids, and the microscopic mechanisms of formations

of phase slips and vortex excitations. As it has always been the case in science, the understanding of natural phenomena and the technological progress arise from the cross-fertilization between fundamental and applied research. The fields of ultracold gases and atomtronics are nowadays among the most promising ones in this sense.

Conclusion

Dans cette thèse, j'ai présenté notre étude de quelques systèmes quantiques mésoscopiques constitués par un gaz de Bose ultrafroid unidimensionnel (1D). Ces systèmes sont intéressants à la fois pour l'étude des propriétés fondamentales des fluides quantiques et, grâce à leur haut degré de contrôle expérimental, également en vue de la réalisation future des dispositifs quantiques atomiques dans le domaine du calcul quantique. En particulier, nous avons étudié le comportement de ces systèmes pour les différents régimes de force d'interaction entre les particules. Pour ce faire, nous avons appliqué une combinaison de plusieurs techniques théoriques, sur la base de différentes approximations valides dans différents régimes physiques, telles que la description de Gross-Pitaevskii en champ moyen pour les interactions faibles, la théorie effective du liquide de Luttinger pour les interactions fortes, la solution exacte de Tonks-Girardeau dans la limite des interactions infiniment fortes et des simulations numériques basées sur le groupe de renormalisation de la matrice densité et des algorithmes de diagonalisation exacte dans les régimes intermédiaires. En particulier, nous avons mis l'accent sur l'interaction des effets liés à la présence dans ces systèmes d'interactions entre les particules, des fluctuations quantiques et des barrières de potentiel localisées, dont les contributions sont toutes amplifiées en 1D par rapport aux dimensions supérieures.

Comme thème récurrent dans tous ces systèmes, nous avons décrit les effets importants de l'écrantage et de renormalisation des barrières de potentiel localisées dans un système de bosons 1D, en raison de la combinaison des effets des interactions entre les particules et des fluctuations quantiques. La présence de cet écrantage, et en particulier d'un régime inconnu jusqu'à maintenant où il est maximisé, pour une force d'interaction intermédiaire, a des conséquences très importantes pour la physique des systèmes que nous avons examinés, affectant diverses observables physiques, à la fois à l'équilibre et hors-équilibre. Cette propriété doit être prise en compte dans la conception des futurs dispositifs quantiques atomiques.

La plupart des problèmes considérés dans cette thèse permettent un certain nombre de développements possibles. En ce qui concerne les courants permanents, il serait intéressant d'étudier l'effet sur la dynamique d'un mouvement hors d'équilibre et dépendant du temps de la barrière de potentiel. L'étude du qubit de flux pourrait être complétée par d'autres recherches sur la nature des états de superposition de circulation. Aussi, en vue d'applications au calcul quantique, l'effet de la décoherence en raison de pertes des particules et de la sensibilité à aux inexactitudes expérimentales doivent être analysés en détail. En ce qui concerne les excitations dipolaires, il serait intéressant d'étudier les effets d'amortissement sur la dynamique du système.

Appendix A

Soliton solution of the Gross-Pitaevskii equation with a rotating barrier

In this Appendix I detail the derivation of the analytical soliton-like solution of the Gross-Pitaevskii (GP) equation (2.18). We first recast the GP equation in dimensionless form by introducing $\tilde{\Phi}(\theta) = \sqrt{L/2\pi}\Phi(2\pi x/L)$, $\tilde{\mu} = mL^2\mu/(2\pi^2\hbar^2)$ and $\tilde{g} = gmNL/(\pi\hbar^2)$, and take $\theta \in [0, 2\pi]$. A parametrization of the condensate wavefunction in density-phase representation $\tilde{\Phi}(\theta) = f(\theta)e^{i\phi(\theta)}$ yields

$$-f'' + f(\phi')^2 - 2\Omega f\phi' + (\Omega^2 - \tilde{\mu} + \tilde{g}f^2)f = 0\,, \tag{A.1}$$

$$-2f'\phi' - f\phi'' + 2\Omega f' = 0\,. \tag{A.2}$$

The effect of the delta barrier is replaced by the cusp condition $f'(0^+) - f'(0^-) = \lambda f(0)$, where $\lambda = mU_0L/\pi\hbar^2$, which assuming a symmetric cusp $f'(0^+) = -f'(0^-)$ and introducing the density $s = f^2$ reads $s'(0^+) = \lambda s(0)$. We first integrate Eq. (A.2) to obtain ϕ',

$$\phi' = \frac{C}{f^2} + \Omega\,, \tag{A.3}$$

where C is an integration constant. Substituting this result into Eq. (A.1) we get $-f'' + C^2/f^3 + (\tilde{g}f^2 - \tilde{\mu})f = 0$, which, upon integration and change of variables, yields $s'^2 = -4C^2 + 2\tilde{g}s^3 - 4\tilde{\mu}s^2 + 4As$, A being an integration constant. Introducing the potential $U(s) = 2C^2 - 2As + 2\tilde{\mu}s^2 - \tilde{g}s^3$, we see that the problem is equivalent to the one of a classical particle of unitary mass with position s and velocity s' having zero total energy. Denoting $U(s) = -\tilde{g}(s - s_1)(s - s_2)(s - s_3) = 0$ with $s_1 \leq s_2 \leq s_3$, an

allowed trajectory is possible in the interval $s_1 < s < s_2$ if $A > 0$. In the presence of the barrier, in order to satisfy the the cusp condition, the soliton trajectory starts at initial position $s_{\min} > s_1$. The soliton is then found upon integration,

$$\int_{s_{\min}}^{s(\theta)} \frac{\mathrm{d}s'}{\sqrt{-2U(s')}} = \int_0^{\theta} \mathrm{d}\theta' = \theta \tag{A.4}$$

Introducing the change of variable $y^2 = (s - s_1)/(s_2 - s_1)$, the integral corresponds to the Jacobi elliptic function $\mathrm{sn}(u|m)$ with $m = (s_2 - s_1)/(s_3 - s_1)$. By imposing periodic boundary conditions for the condensate density (*i.e.*, requiring that at half-period the soliton solution reaches its maximum value $s = s_2$), we find $\pi\sqrt{\tilde{g}(s_3 - s_1)/2} + \alpha = K$ and

$$s(\theta) = s_1 + (s_2 - s_1)\mathrm{sn}^2[(K - \alpha)\theta/\pi + \alpha]. \tag{A.5}$$

Here $\alpha = F[\arcsin(\sqrt{(s_{min} - s_1)/(s_2 - s_1)})|m]$, with $F[\phi|m]$ being the incomplete elliptic integral of the first kind, and K is the corresponding complete elliptic integral.

Imposing the normalization condition $\int_0^{2\pi} d\theta s(\theta) = 1$ we obtain

$$2\pi s_1 + 4(K - \alpha)(K - \alpha - E + \alpha')/(\pi\tilde{g}) = 1, \tag{A.6}$$

where $E[\phi|m]$ and E are respectively the incomplete and complete elliptic integrals of the second kind, and $\alpha' = E[\arcsin(\sqrt{(s_{min} - s_1)/(s_2 - s_1)})|m]$. Substituting Eq. (A.5) for s in equation $s'^2 = -2U(s)$ and equating the terms with the same power of sn, yields the following parameter identification:

$$\tilde{\mu} = 3\tilde{g}s_1/2 + (1 + m)[(K - \alpha)/\pi]^2\,; \tag{A.7}$$

$$A = 2\tilde{\mu}s_1 - 3\tilde{g}s_1^2/2 - 2m[(K - \alpha)/\pi]^4/\tilde{g}\,; \tag{A.8}$$

$$C^2 = As_1 - \tilde{\mu}s_1^2 + \tilde{g}s_1^3/2\,. \tag{A.9}$$

Finally, the cusp condition yields an equation for $s_{\min}$,

$$\lambda s_{\min} = \sqrt{-2U(s_{\min})}. \tag{A.10}$$

Equations (A.7 – A.10) form a coupled set of equations which can be solved as a function of m and $s_{\min}$.

Using Eqs. (A.3) and (A.5), we then obtain the solution for the phase of the soliton

solution:

$$\phi(\theta) = C\frac{\Pi[(s_1 - s_2)/s_1; (K-\alpha)\theta/\pi + K|m] - \Pi[(s_1 - s_2)/s_1; \alpha|m]}{(K-\alpha)s_1} + \Omega(\theta + \pi)\,, \tag{A.11}$$

where $\Pi[n; u|m]$ is the incomplete elliptic integral of the third kind.
Imposing 2π-periodicity of the condensate wave function, integration of Eq. (A.3) yields $2\pi n = \int_{-\pi}^{\pi} d\theta \frac{C}{s} + 2\pi\Omega$, hence

$$\frac{2\pi(n-\Omega)}{C} = 2\pi(\Pi[(s_1 - s_2)/s_1; K|m] - \frac{\Pi[(s_1 - s_2)/s_1; \alpha|m])}{(K-\alpha)s_1}\,. \tag{A.12}$$

In summary, we find the soliton solution according to the following strategy: for given values of the interaction constant $\tilde{g}$, the barrier strength λ and the Coriolis flux Ω, we express s_1, s_2 and s_3 (hence $\tilde{\mu}$, A, and C) as a function of m and $s_{\min}$, then solve simultaneously Eq. (A.10) and the one obtained after equating Eqs. (A.12) and (A.9). This uniquely fixes m and $s_{\min}$, and hence the entire soliton solution.

Appendix B

One-body density matrix for hard-core bosons on a lattice

In this Appendix I present the exact approach that I have pursued to calculate the one-body density matrix $g^{(1)}_{l,j} = \langle b^\dagger_l b_j \rangle$ for hard-core bosons in a one-dimensional lattice. I have used this method in Chap. 3 to calculate the momentum distribution according to Eq. (3.8).

The method follows the scheme presented in [145]. Applying the Jordan-Wigner mapping, Eq. (3.3) (see Sec. 3.2.1) the one-particle Green's function for the hard-core bosons can be written in the form

$$G_{l,j} = \langle \Psi_B | b_l b^\dagger_j | \Psi_B \rangle = \langle \Psi_F | \prod_{\beta=1}^{l-1} e^{i\pi f^\dagger_\beta f_\beta} f_l f^\dagger_j \prod_{\gamma=1}^{j-1} e^{-i\pi f^\dagger_\gamma f_\gamma} f_l f^\dagger_j | \Psi_F \rangle \equiv \langle \Psi^A_F | \Psi^B_F \rangle \ , \quad \text{(B.1)}$$

where $|\Psi_B\rangle$ is the hard-core bosonic ground-state, $|\Psi_F\rangle$ is the equivalent noninteracting fermionic ground-state, and we have denoted

$$\langle \Psi^A_F | = \left(f^\dagger_l \prod_{\beta=1}^{l-1} e^{-i\pi f^\dagger_\beta f_\beta} | \Psi_F \rangle \right)^\dagger \ , \quad |\Psi^B_F\rangle = f^\dagger_j \prod_{\gamma=1}^{j-1} e^{-i\pi f^\dagger_\gamma f_\gamma} | \Psi_F \rangle \ . \quad \text{(B.2)}$$

The ground-state of the equivalent noninteracting fermionic system can be obtained diagonalizing Hamiltonian (3.4), and can be recast in the form

$$|\Psi_F\rangle = \prod_{\delta=1}^{N} \sum_{\sigma=1}^{M} P_{\sigma,\delta} f^\dagger_\sigma |0\rangle \ , \quad \text{(B.3)}$$

with N the number of particles, M the number of lattice sites, $|0\rangle$ the vacuum state,

and the matrix components $P_{\sigma,\delta}$ are given by the N lowest eigenstates of Hamiltonian (3.4).

In order to calculate $|\Psi_F^A\rangle$, and $|\Psi_F^B\rangle$, we first observe that

$$\prod_{\beta=1}^{l-1} e^{-i\pi f_\beta^\dagger f_\beta} = \prod_{\beta=1}^{l-1} [1 - 2 f_\beta^\dagger f_\beta] \ , \tag{B.4}$$

then, the action of $\prod_{\beta=1}^{l-1} e^{-i\pi f_\beta^\dagger f_\beta}$ on the fermionic ground-state given by Eq. (B.3) implies only a change of sign of the elements $P_{\sigma,\delta}$ for $\sigma \leqslant l-1$, and the creation of a particle at site l implies the addition of one column to the matrix P, with the element $P_{l,N+1} = 1$ and all the others equal to zero. Thus, $|\Psi_F^A\rangle$, and $|\Psi_F^B\rangle$ can be rewritten as

$$|\Psi_F^{A,B}\rangle = \prod_{\delta=1}^{N+1} \sum_{\sigma=1}^{M} P_{\sigma,\delta}^{A,B} f_\sigma^\dagger |0\rangle \ , \tag{B.5}$$

where the matrices $P^{A,B}$ are obtained from P changing the proper signs and adding the new column $N+1$. The Green's function is then calculated numerically as

$$G_{l,j} = \langle \Psi_F^A | \Psi_F^B \rangle = \langle 0 | \prod_{\delta=1}^{N+1} \sum_{\sigma=1}^{M} P_{\sigma,\delta}^{A} f_\sigma \prod_{\delta'=1}^{N+1} \sum_{\sigma'=1}^{M} P_{\sigma',\delta'}^{B} f_{\sigma'}^\dagger |0\rangle \ , \tag{B.6}$$

and the one-particle density matrix is thus obtained as $g_{l,j}^{(1)} = (G_{l,j})^\dagger$.

Appendix C

Momentum distribution of a superposition of circulation states in the non-interacting limit

In this Appendix I detail the derivation of the momentum distribution, defined by Eq. (3.7) for the ground state of the continuum Hamiltonian (2.1), in the non-interacting regime. In this case the many-body problem reduces to a single-particle one, and in the absence of the barrier the Schrödinger equation, in polar coordinates and scaling the energies in units of $E_0 = 2\pi^2\hbar^2/mL^2$, with m being the particle mass, and L the system size, reads

$$\left(-i\frac{\partial}{\partial\theta} - \Omega\right)^2 \psi(\theta) = E\psi(\theta) \ , \tag{C.1}$$

where $\theta \in [0, 2\pi]$. The wave function for a state with defined circulation is a plane wave $\psi(\theta) = (1/\sqrt{2\pi})e^{in\theta}$, where $n \in \mathbb{Z}$ to satisfy periodic boundary conditions, and the corresponding spectrum is $E_n = (n-\Omega)^2$. The momentum distribution then reads

$$\begin{aligned} n(\mathbf{k}) &= \int \mathrm{d}\mathbf{x} \int \mathrm{d}\mathbf{x}' e^{i\mathbf{k}\cdot(\mathbf{x}-\mathbf{x}')}\psi^*(\mathbf{x})\psi(\mathbf{x}') \\ &\sim \left| \int_0^{2\pi} \mathrm{d}\theta \ e^{i(k_x R\cos\theta + k_y R\sin\theta)}\psi^*(\theta) \right|^2 \\ &= \left| e^{in\gamma} J_n(|\mathbf{k}|R) \right|^2 = |J_n(|\mathbf{k}|R)|^2 \ , \end{aligned} \tag{C.2}$$

where $R = L/2\pi$ is the ring radius, we have defined γ as $k_x = |\mathbf{k}|\sin\gamma$, $k_y = |\mathbf{k}|\cos\gamma$, and J_n is the n-th order Bessel function of the first kind. For $n = 0$ the momentum

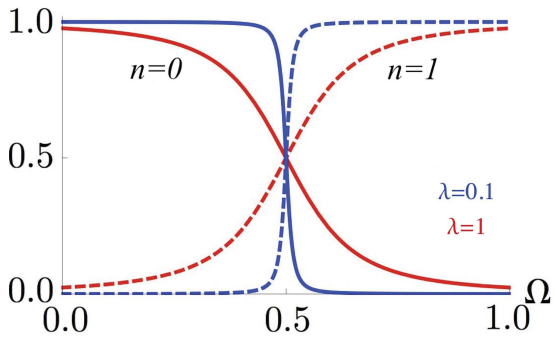

Figure C.1: Weights $|\sin(\varphi/2)|^2$ and $|\cos(\varphi/2)|^2$ of the $n = 0$ and $n = 1$ circulation states in the superposition Eq. (C.8) as a function of the flux Ω, for different values of the dimensionless barrier strength λ,

distribution is peaked at $\mathbf{k} = 0$, while for $n > 0$ it is ring shaped, with a radius that grows with n.

In the presence of a localized barrier of strength λ the Schrödinger equation becomes

$$\left(-i\frac{\partial}{\partial\theta} - \Omega\right)^2 \psi(\theta) + \lambda\delta(\theta)\psi(\theta) = E\psi(\theta) \; . \tag{C.3}$$

The effect of the δ-barrier is to mix states with different circulation states. For a small barrier we can reduce to the simplest case of mixing of states that differ by just one quantum of angular momentum, and apply degenerate perturbation theory. We write the Hamiltonian in the following form

$$\mathcal{H} = \begin{pmatrix} E_n & \lambda/2\pi \\ \lambda/2\pi & E_{n+1} \end{pmatrix} \; ; \tag{C.4}$$

the corresponding eigenvalues and eigenvectors reads:

$$\epsilon_{1,2} = \frac{E_{n+1} + E_n}{2} \pm \frac{\sqrt{\delta E^2 + \lambda^2/\pi^2}}{2} \; , \tag{C.5}$$

where $\delta E = E_{n+1} - E_n$, and

$$w_1 = \begin{pmatrix} \sin(\varphi/2) \\ \cos(\varphi/2) \end{pmatrix} \; , \qquad w_2 = \begin{pmatrix} \cos(\varphi/2) \\ -\sin(\varphi/2) \end{pmatrix} \; , \tag{C.6}$$

where

$$\cos^2(\varphi/2) = \frac{\sqrt{\delta E^2 + \lambda^2/\pi^2} - \delta E}{2\sqrt{\delta E^2 + \lambda^2/\pi^2}} \; . \tag{C.7}$$

We then write the wave function as

$$\psi(\theta) = \frac{1}{\sqrt{2\pi}} \sin(\varphi/2) e^{in\theta} + \frac{1}{\sqrt{2\pi}} \cos(\varphi/2) e^{i(n+1)\theta} \,, \tag{C.8}$$

where φ depends on λ and Ω.

The momentum distribution in this case becomes

$$\begin{aligned} n(\mathbf{k}) &\sim \left| \int_0^{2\pi} \mathrm{d}\theta \; e^{i(k_x R\cos\theta + k_y R \sin\theta)} \psi^*(\theta) \right|^2 \\ &= \left| \sin(\varphi/2) e^{in\gamma} J_n(|\mathbf{k}|R) + \cos(\varphi/2) e^{i(n+1)\gamma} J_{n+1}(|\mathbf{k}|R) \right|^2 \\ &= \sin^2(\varphi/2) J_n^2(|\mathbf{k}|R) + \cos^2(\varphi/2) J_{n+1}^2(|\mathbf{k}|R) \\ &\quad + 2\sin(\varphi/2)\cos(\varphi/2)\cos(\gamma) J_n(|\mathbf{k}|R) J_{n+1}(|\mathbf{k}|R) \,, \end{aligned} \tag{C.9}$$

where an interference term, proportional to $\cos\gamma$, appears between the two states with defined angular momentum, giving rise to a 2π-periodic angular modulation of the ring shape found previously. This behaviour is the same found in Fig. 3.9, where we observe an analogous modulation in the weak barrier and weak interaction case, that we can interpret than as direct consequence of the superposition of two stated that differ by one quantum of angular momentum.

Finally, in Fig. C.2 I show a comparison between the momentum distribution for the model on a lattice (Hamiltonian (3.1)) and the continuum one (Hamiltonian (2.1)). The main difference arising in the momentum distribution, is due to the product with

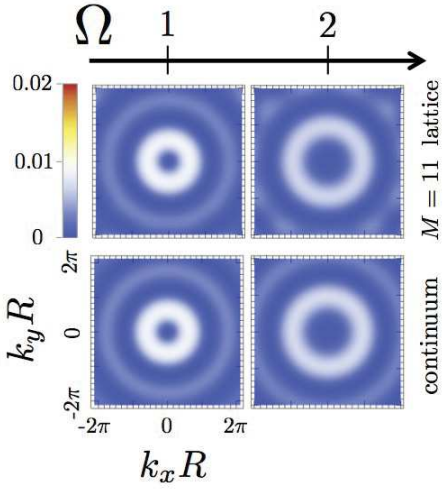

Figure C.2: Comparison between the momentum distribution of model on a lattice (Hamiltonian (3.1)) for $M = 11$ and the continuum one (Hamiltonian (2.1)) for different values of the flux Ω.

the Fourier transform of the Wannier function in the lattice case, see Eq. (3.8). This, however, being the Fourier transform of a very localized function in real space (the Wannier function) is a very slow-decaying function in k-space, that doesn't change the shape of the momentum distribution at low momenta. Also the effect of the discretization of space in the model on a lattice is visible only for very large momenta, see Fig C.2. The momentum distribution in the continuum and lattice model have thus the same qualitative form, and we can for simplicity consider the continuum model to obtain some analytical insight also for the model on a lattice.

Bibliography

[1] H. Bethe. Zur Theorie der Metalle. *Z. Phys.*, **71**, 205, 1931.

[2] T. Giamarchi. *Quantum Physics in One Dimension*. Oxford University Press, Oxford, 2004.

[3] M. A. Cazalilla, R. Citro, T. Giamarchi, E. Orignac, and M. Rigol. One dimensional bosons: From condensed matter systems to ultracold gases. *Rev. Mod. Phys.*, **83**, 1405, 2011.

[4] R. Saito, G. Dresselhaus, and M. S. Dresselhaus. *Physical Properties of Carbon Nanotubes*. World Scientific, 1998.

[5] L. L. Sohn, L. P. Kouwenhoven, and G. Schön. *Mesoscopic Electron Transport*, volume 345. NATO ASI Series E, 1997.

[6] A. N. Aleshin, H. J. Lee, Y. W. Park, and K. Akagi. One-Dimensional Transport in Polymer Nanofibers. *Phys. Rev. Lett.*, **93**, 196601, 2004.

[7] S. V. Zaitsev-Zotov, Y. A. Kumzerov, Y. A. Firsov, and P. Monceau. Luttinger-liquid-like transport in long InSb nanowires. *Journal of Physics: Condensed Matter*, **12**, L303, 2000.

[8] R. Fazio and H. van der Zant. Quantum phase transitions and vortex dynamics in superconducting networks. *Physics Reports*, **355**, 235, 2001.

[9] W. Teizer, R. B. Hallock, E. Dujardin, and T. W. Ebbesen. ^{4}He Desorption from Single Wall Carbon Nanotube Bundles: A One-Dimensional Adsorbate. *Phys. Rev. Lett.*, **82**, 5305, 1999.

[10] M. H. Anderson, J. R. Ensher, M. R. Matthews, C. E. Wieman, and E. A. Cornell. Observation of Bose-Einstein Condensation in a Dilute Atomic Vapor. *Science*, **269**, 198, 1995.

[11] K. B. Davis, M. O. Mewes, M. R. Andrews, N. J. van Druten, D. S. Durfee, D. M. Kurn, and W. Ketterle. Bose-Einstein Condensation in a Gas of Sodium Atoms. *Phys. Rev. Lett.*, **75**, 3969, 1995.

[12] I. Bloch, J. Dalibard, and W. Zwerger. Many-body physics with ultracold gases. *Rev. Mod. Phys.*, **80**, 885, 2008.

[13] A. N. Wenz, G. Zürn, S. Murmann, I. Brouzos, T. Lompe, and S. Jochim. From Few to Many: Observing the Formation of a Fermi Sea One Atom at a Time. *Science*, **342**, 457, 2013.

[14] I. Bloch, J. Dalibard, and S. Nascimbène. Quantum simulations with ultracold quantum gases. *Nat. Phys.*, **8**, 267, 2012.

[15] B. T. Seaman, M. Krämer, D. Z. Anderson, and M. J. Holland. Atomtronics: Ultracold-atom analogs of electronic devices. *Phys. Rev. A*, **75**, 023615, 2007.

[16] M. Cominotti, D. Rossini, M. Rizzi, F. Hekking, and A. Minguzzi. Optimal Persistent Currents for Interacting Bosons on a Ring with a Gauge Field. *Phys. Rev. Lett.*, **113**, 025301, 2014.

[17] M. Cominotti, M. Rizzi, D. Rossini, D. Aghamalyan, L. Amico, L.-C. Kwek, F. Hekking, and A. Minguzzi. Optimal scaling of persistent currents for interacting bosons on a ring. *The European Physical Journal Special Topics*, **224**, 519, 2015.

[18] D. Aghamalyan, M. Cominotti, M. Rizzi, D. Rossini, F. Hekking, A. Minguzzi, L.-C. Kwek, and L. Amico. Coherent superposition of current flows in an atomtronic quantum interference device. *New Journal of Physics*, **17**, 045023, 2015.

[19] M. Cominotti, F. Hekking, and A. Minguzzi. Dipole mode of a strongly correlated one-dimensional bose gas in a split trap: Parity effect and barrier renormalization. *Phys. Rev. A*, **92**, 033628, 2015.

[20] I. Bloch. Quantum coherence and entanglement with ultracold atoms in optical lattices. *Nature*, **453**, 1016, 2008.

[21] I. Bloch. Ultracold quantum gases in optical lattices. *Nat. Phys.*, **1**, 23, 2005.

[22] H. Moritz, T. Stöferle, M. Köhl, and T. Esslinger. Exciting Collective Oscillations in a Trapped 1D Gas. *Phys. Rev. Lett.*, **91**, 250402, 2003.

[23] R. Folman, P. Krüger, D. Cassettari, B. Hessmo, T. Maier, and J. Schmiedmayer. Controlling Cold Atoms using Nanofabricated Surfaces: Atom Chips. *Phys. Rev. Lett.*, **84**, 4749, 2000.

[24] J. Esteve, J.-B. Trebbia, T. Schumm, A. Aspect, C. I. Westbrook, and I. Bouchoule. Observations of Density Fluctuations in an Elongated Bose Gas: Ideal Gas and Quasicondensate Regimes. *Phys. Rev. Lett.*, **96**, 130403, 2006.

[25] M. Greiner, I. Bloch, O. Mandel, T. W. Hänsch, and T. Esslinger. Exploring Phase Coherence in a 2D Lattice of Bose-Einstein Condensates. *Phys. Rev. Lett.*, **87**, 160405, 2001.

[26] H. Moritz, T. Stöferle, M. Köhl, and T. Esslinger. Exciting Collective Oscillations in a Trapped 1D Gas. *Phys. Rev. Lett.*, **91**, 250402, 2003.

[27] T. Kinoshita, T Wenger, and D. S. Weiss. Observation of a One-Dimensional Tonks-Girardeau Gas. *Science*, **305**, 1125, 2004.

[28] B. Paredes, A. Widera, V. Murg, O. Mandel, S. Fölling, I. Cirac, G. V. Shlyapnikov, T. W. Hänsch, and I. Bloch. Tonks-Girardeau gas of ultracold atoms in an optical lattice. *Nature*, **429**, 277, 2004.

[29] T. Stöferle, H. Moritz, C. Schori, M. Köhl, and T. Esslinger. Transition from a Strongly Interacting 1D Superfluid to a Mott insulator. *Phys. Rev. Lett.*, **92**, 130403, 2004.

[30] B. Laburthe Tolra, K. M. O'Hara, J. H. Huckans, W. D. Phillips, S. L. Rolston, and J. V. Porto. Observation of Reduced Three-Body Recombination in a Correlated 1D Degenerate Bose Gas. *Phys. Rev. Lett.*, **92**, 190401, 2004.

[31] C. D. Fertig, K. M. O'Hara, J. H. Huckans, S. L. Rolston, W. D. Phillips, and J. V. Porto. Strongly Inhibited Transport of a Degenerate 1D Bose Gas in a Lattice. *Phys. Rev. Lett.*, **94**, 120403, 2005.

[32] E. Haller, R. Hart, M. J. Mark, J. G. Danzl, L. Reichsöllner, M. Gustavsson, M. Dalmonte, G. Pupillo, and H.-C. Nägerl. Pinning quantum phase transition for a Luttinger liquid of strongly interacting bosons. *Nature*, **466**, 597, 2010.

[33] J. Reichel. Microchip traps and Bose–Einstein condensation. *Applied Physics B*, **74**, 469, 2002.

[34] T. Schumm, S. Hofferberth, L. M. Andersson, S. Wildermuth, S. Groth, I. Bar-Joseph, J. Schmiedmayer, , and P. Krüger. Matter-wave interferometry in a double well on an atom chip. *Nat. Phys.*, **1**, 57, 2005.

[35] J.-B. Trebbia, J. Esteve, C. I. Westbrook, and I. Bouchoule. Experimental Evidence for the Breakdown of a Hartree-Fock Approach in a Weakly Interacting Bose Gas. *Phys. Rev. Lett.*, **97**, 250403, 2006.

[36] J. Fortágh and C. Zimmermann. Magnetic microtraps for ultracold atoms. *Rev. Mod. Phys.*, **79**, 235, 2007.

[37] S. Hofferberth, I. Lesanovsky, B. Fischer, T. Schumm, and J. Schmiedmayer. Non-equilibrium coherence dynamics in one-dimensional bose gases. *Nature*, **449**, 324, 2007.

[38] A. H. van Amerongen, J. J. P. van Es, P. Wicke, K. V. Kheruntsyan, and N. J. van Druten. Yang-Yang Thermodynamics on an Atom Chip. *Phys. Rev. Lett.*, **100**, 090402, 2008.

[39] T. Jacqmin, J. Armijo, T. Berrada, K. V. Kheruntsyan, and I. Bouchoule. Sub-Poissonian Fluctuations in a 1D Bose Gas: From the Quantum Quasicondensate to the Strongly Interacting Regime. *Phys. Rev. Lett.*, **106**, 230405, 2011.

[40] B. Fang, G. Carleo, A. Johnson, and I. Bouchoule. Quench-Induced Breathing Mode of One-Dimensional Bose Gases. *Phys. Rev. Lett.*, **113**, 035301, 2014.

[41] L. P. Pitaevskii and S. Stringari. *Bose-Einstein Condensation*. Oxford University Press, New York, 2003.

[42] M. Olshanii. Atomic Scattering in the Presence of an External Confinement and a Gas of Impenetrable Bosons. *Phys. Rev. Lett.*, **81**, 938, 1998.

[43] C. Chin, R. Grimm, P. Julienne, and E. Tiesinga. Feshbach resonances in ultracold gases. *Rev. Mod. Phys.*, **82**, 1225, 2010.

[44] G. E. Astrakharchik, D. Blume, S. Giorgini, and B. E. Granger. Quasi-One-Dimensional Bose Gases with a Large Scattering Length. *Phys. Rev. Lett.*, **92**, 030402, 2004.

[45] C. N. Yang. Concept of Off-Diagonal Long-Range Order and the Quantum Phases of Liquid He and of Superconductors. *Rev. Mod. Phys.*, **34**, 694, 1962.

[46] O. Penrose and L. Onsager. Bose-Einstein Condensation and Liquid Helium. *Phys. Rev.*, **104**, 576, 1956.

[47] P. C. Hohenberg. Existence of Long-Range Order in One and Two Dimensions. *Phys. Rev.*, **158**, 383, 1967.

[48] L. Pitaevskii and S. Stringari. Uncertainty principle, quantum fluctuations, and broken symmetries. *Journal of Low Temperature Physics*, **85**, 377, 1991.

[49] F. D. M. Haldane. Effective Harmonic-Fluid Approach to Low-Energy Properties of One-Dimensional Quantum Fluids. *Phys. Rev. Lett.*, **47**, 1840, 1981.

[50] M. A. Cazalilla. Bosonizing one-dimensional cold atomic gases. *Journal of Physics B: Atomic, Molecular and Optical Physics*, **37**, S1, 2004.

[51] D. Petrov, G. Shlyapnikov, and J. Walraven. Regimes of Quantum Degeneracy in Trapped 1D Gases. *Phys. Rev. Lett.*, **85**, 3745, 2000.

[52] W. Ketterle and N. J. van Druten. Bose-Einstein condensation of a finite number of particles trapped in one or three dimensions. *Phys. Rev. A*, **54**, 656, 1996.

[53] E. H. Lieb and W. Liniger. Exact Analysis of an Interacting Bose Gas. I. The General Solution and the Ground State. *Phys. Rev.*, **130**, 1605, 1963.

[54] E. H. Lieb. Exact Analysis of an Interacting Bose Gas. II. The Excitation Spectrum. *Phys. Rev.*, **130**, 1616, 1963.

[55] S. R. White. Density matrix formulation for quantum renormalization groups. *Phys. Rev. Lett.*, **69**, 2863, 1992.

[56] U. Schollwöck. The density-matrix renormalization group. *Rev. Mod. Phys.*, **77**, 259, 2005.

[57] U. Schollwöck. The density-matrix renormalization group in the age of matrix product states. *Annals of Physics*, **326**, 96, 2011.

[58] M. D. Girardeau. Relationship between Systems of Impenetrable Bosons and Fermions in One Dimension. *J. Mat. Phys.*, **1**, 516, 1960.

[59] A. Lenard. Momentum Distribution in the Ground State of the One-Dimensional System of Impenetrable Bosons. *J. Mat. Phys.*, **5**, 930, 1964.

[60] P. J. Forrester, N. E. Frankel, T. M. Garoni, and N. S. Witte. Finite one-dimensional impenetrable Bose systems: Occupation numbers. *Phys. Rev. A*, **67**, 043607, 2003.

[61] A. Minguzzi, P. Vignolo, and M. P. Tosi. High-momentum tail in the Tonks gas under harmonic confinement. *Physics Letters A*, **294**, 222, 2002.

[62] M. Olshanii and V. Dunjko. Short-Distance Correlation Properties of the Lieb-Liniger System and Momentum Distributions of Trapped One-Dimensional Atomic Gases. *Phys. Rev. Lett.*, **91**, 090401, 2003.

[63] M. D. Girardeau and E. M. Wright. Breakdown of Time-Dependent Mean-Field Theory for a One-Dimensional Condensate of Impenetrable Bosons. *Phys. Rev. Lett.*, **84**, 5239, 2000.

[64] F. Dalfovo, S. Giorgini, L. P. Pitaevskii, and S. Stringari. Theory of Bose-Einstein condensation in trapped gases. *Rev. Mod. Phys.*, **71**, 463, 1999.

[65] C. Mora and Y. Castin. Extension of Bogoliubov theory to quasicondensates. *Phys. Rev. A*, **67**, 053615, 2003.

[66] E. P. Gross. Structure of a quantized vortex in boson systems. *Il Nuovo Cimento Series 10*, **20**, 454, 1961.

[67] L. P. Pitaevskii. Vortex Lines in an Imperfect Bose Gas. *Sov. Phys. JETP*, **13**, 451, 1961.

[68] F. Dalfovo and S. Stringari. Bosons in anisotropic traps: Ground state and vortices. *Phys. Rev. A*, **53**, 2477, 1996.

[69] F. D. M. Haldane. 'luttinger liquid theory' of one-dimensional quantum fluids. I. Properties of the Luttinger model and their extension to the general 1D interacting spinless Fermi gas. *Journal of Physics C: Solid State Physics*, **14**, 2585, 1981.

[70] J. M. Luttinger. An Exactly Soluble Model of a Many Fermion System. *J. Mat. Phys.*, **4**, 1963.

[71] S.-I. Tomonaga. Remarks on Bloch's Method of Sound Waves applied to Many-Fermion Problems. *Progress of Theoretical Physics*, **5**, 544, 1950.

[72] N. D. Mermin and H. Wagner. Absence of Ferromagnetism or Antiferromagnetism in One- or Two-Dimensional Isotropic Heisenberg Models. *Phys. Rev. Lett.*, **17**, 1133, 1966.

[73] E. M. Lifshits and L. P. Pitaevskii. *Statistical Physics Part 2 Volume 9: Course of Theoretical Physics*. Butterworth-Heinemann, 1980.

[74] J.-S. Caux and P. Calabrese. Dynamical density-density correlations in the one-dimensional Bose gas. *Phys. Rev. A*, **74**, 031605, 2006.

[75] A. Yu. Cherny, J.-S. Caux, and J. Brand. Decay of superfluid currents in the interacting one-dimensional Bose gas. *Phys. Rev. A*, **80**, 043604, 2009.

[76] J. Brand and A. Yu. Cherny. Dynamic structure factor of the one-dimensional Bose gas near the Tonks-Girardeau limit. *Phys. Rev. A*, **72**, 033619, 2005.

[77] G. Lang, F. Hekking, and A. Minguzzi. Dynamic structure factor and drag force in a one-dimensional strongly interacting Bose gas at finite temperature. *Phys. Rev. A*, **91**, 063619, 2015.

[78] N. Fabbri, M. Panfil, D. Clément, L. Fallani, M. Inguscio, C. Fort, and J.-S. Caux. Dynamical structure factor of one-dimensional Bose gases: Experimental signatures of beyond-Luttinger-liquid physics. *Phys. Rev. A*, **91**, 043617, 2015.

[79] A. Weisse and H. Fehske. *Computational Many-Particle Physics: Exact Diagonalization Techniques*, volume 739 of *Lecture Notes in Physics*, pages 529–544. ed. H. Fehske, R. Schneider, A. Weisse. Springer Berlin, Heidelberg, 2008.

[80] A. L. Fetter and J. D. Walecka. *Quantum Theory of Many-Particle Systems*. McGraw-Hill, New York, 1971.

[81] D. W. Hallwood, T. Ernst, and J. Brand. Robust mesoscopic superposition of strongly correlated ultracold atoms. *Phys. Rev. A*, **82**, 063623, 2010.

[82] Y. Aharonov and D. Bohm. Significance of Electromagnetic Potentials in the Quantum Theory. *Phys. Rev.*, **115**, 485, 1959.

[83] M. Büttiker, Y. Imry, and R. Landauer. Josephson behavior in small normal one-dimensional rings. *Phys. Lett. A*, **96**, 365, 1983.

[84] A. A. Zvyagin and I. V. Krive. Persistent currents in one-dimensional systems of strongly correlated electrons. *Low. Temp. Phys.*, **21**, 533, 1995.

[85] B. S. Deaver and W. M. Fairbank. Experimental Evidence for Quantized Flux in Superconducting Cylinders. *Phys. Rev. Lett.*, **7**, 43, 1961.

[86] L. P. Lévy, G. Dolan, J. Dunsmuir, and H. Bouchiat. Magnetization of mesoscopic copper rings: Evidence for persistent currents. *Phys. Rev. Lett.*, **64**, 2074, 1990.

[87] H. Bluhm, N. C. Koshnick, J. A. Bert, M. E. Huber, and K. A. Moler. Persistent Currents in Normal Metal Rings. *Phys. Rev. Lett.*, **102**, 136802, 2009.

[88] A. C. Bleszynski-Jayich, W. E. Shanks, B. Peaudecerf, E. Ginossar, F. von Oppen, L. Glazman, and J. G. E. Harris. Persistent Currents in Normal Metal Rings. *Science*, **326**, 272, 2009.

[89] S. Gupta, K. W. Murch, K. L. Moore, T. P. Purdy, and D. M. Stamper-Kurn. Bose-Einstein Condensation in a Circular Waveguide. *Phys. Rev. Lett.*, **95**, 143201, 2005.

[90] O. Morizot, Y. Colombe, V. Lorent, H. Perrin, and B. M. Garraway. Ring trap for ultracold atoms. *Phys. Rev. A*, **74**, 023617, 2006.

[91] C. Ryu, M. F. Andersen, P. Cladé, V. Natarajan, K. Helmerson, and W. D. Phillips. Observation of persistent flow of a Bose-Einstein condensate in a toroidal trap. *Phys. Rev. Lett.*, **99**, 260401, 2007.

[92] W. H. Heathcote, E. Nugent, B. T. Sheard, and C. J. Foot. A ring trap for ultracold atoms in an RF-dressed state. *New J. Phys.*, **10**, 043012, 2008.

[93] B. E. Sherlock, M. Gildemeister, E. Owen, E. Nugent, and C. J. Foot. Time-averaged adiabatic ring potential for ultracold atoms. *Phys. Rev. A*, **83**, 043408, Apr 2011.

[94] S. Moulder, S. Beattie, R. P. Smith, N. Tammuz, and Z. Hadzibabic. Quantized supercurrent decay in an annular Bose-Einstein condensate. *Phys. Rev. A*, **86**, 013629, 2012.

[95] N. Murray, M. Krygier, M. Edwards, K.C. Wright, G.K. Campbell, and C. W. Clark. Probing the circulation of ring-shaped Bose-Einstein condensates. *Phys. Rev. A*, **88**, 053615, 2013.

[96] A. Ramanathan, K. C. Wright, S. R. Muniz, M. Zelan, W. T. Hill III, C. J. Lobb, K. Helmerson, W. D. Phillips, and G. K. Campbell. Superflow in a toroidal Bose-Einstein condensate: an atom circuit with a tunable weak link. *Phys. Rev. Lett.*, **106**, 130401, 2011.

[97] K. C. Wright, R. B. Blakestad, C. J. Lobb, W. D. Phillips, and G. K. Campbell. Driving phase slips in a superfluid atom circuit with a rotating weak link. *Phys. Rev. Lett.*, **110**, 025302, 2013.

[98] S. Eckel, J. G. Lee, F. Jendrzejewski, N. Murray, C. W. Clark, C. J Lobb, W. D. Phillips, M. Edwards, and G. K. Campbell. Hysteresis in a quantized superfluid atomtronic circuit. *Nature*, **506**, 200, 2014.

[99] S. Eckel, F. Jendrzejewski, A. Kumar, C. J. Lobb, and G. K. Campbell. Interferometric Measurement of the Current-Phase Relationship of a Superfluid Weak Link. *Phys. Rev. X*, **4**, 031052, 2014.

[100] R. Mathew, A. Kumar, S. Eckel, F. Jendrzejewski, G. K. Campbell, M. Edwards, and E. Tiesinga. Self-heterodyne detection of the *in-situ* phase of an atomic-SQUID. *arXiv:1506.09149*, 2015.

[101] F. Piazza, L. A. Collins, and A. Smerzi. Vortex-induced phase-slip dissipation in a toroidal Bose-Einstein condensate flowing through a barrier. *Phys. Rev. A*, **80**, 021601, 2009.

[102] J. J. Cooper, D. W. Hallwood, and J. A. Dunningham. Entanglement-enhanced atomic gyroscope. *Phys. Rev. A*, **81**, 043624, 2010.

[103] D. Solenov and D. Mozyrsky. Macroscopic two-state systems in trapped atomic condensates. *Phys. Rev. A*, **82**, 061601, 2010.

[104] A. Nunnenkamp, A. M. Rey, and K. Burnett. Superposition states of ultracold bosons in rotating rings with a realistic potential barrier. *Phys. Rev. A*, **84**, 053604, 2011.

[105] C. Schenke, A. Minguzzi, and F. W. J. Hekking. Nonadiabatic creation of macroscopic superpositions with strongly correlated one-dimensional bosons in a ring trap. *Phys. Rev. A*, **84**, 053636, 2011.

[106] D. W. Hallwood and J. Brand. Engineering mesoscopic superpositions of superfluid flow. *Phys. Rev. A*, **84**, 043620, 2011.

[107] A. L. Fetter. Rotating trapped Bose-Einstein condensates. *Rev. Mod. Phys.*, **81**, 647, 2009.

[108] A. E. Leanhardt, A. Görlitz, A. P. Chikkatur, D. Kielpinski, Y. Shin, D. E. Pritchard, and W. Ketterle. Imprinting vortices in a Bose-Einstein condensate using topological phases. *Phys. Rev. Lett.*, **89**, 190403, 2002.

[109] Y.-J. Lin, R. L. Compton, K. Jimenez-Garcia, J. V. Porto, and I. B. Spielman. Synthetic magnetic fields for ultracold neutral atoms. *Nature*, **462**, 628, 2009.

[110] J. Dalibard, F. Gerbier, G. Juzeliūnas, and P. Öhberg. Artificial gauge potentials for neutral atoms. *Rev. Mod. Phys.*, **83**, 1523, 2011.

[111] F. Bloch. Superfluidity in a Ring. *Phys. Rev. A*, **7**, 2187, 1973.

[112] A. Müller-Groeling, H. A. Weidenmueller, and C. H. Lewenkopf. Interacting electrons in mesoscopic rings. *Europhys. Lett.*, **22**, 193, 1993.

[113] F. Bloch. Josephson Effect in a Superconducting Ring. *Phys. Rev. B*, **2**, 109, 1970.

[114] A. J. Leggett. *Granular Nanoelectronics*, volume 251, page 297. D. K. Ferry, J. R. Barker, and C. Jacoboni, Nato ASI Series B, 1991.

[115] D. Loss. Parity effects in a Luttinger liquid: Diamagnetic and paramagnetic ground states. *Phys. Rev. Lett.*, **69**, 343, 1992.

[116] M. Manninen, S. Viefers, and S. M. Reimann. Quantum rings for beginners II: Bosons versus fermions. *Physica E: Low-dimensional Systems and Nanostructures*, **46**, 119, 2012.

[117] F. W. J. Hekking and L. I. Glazman. Quantum fluctuations in the equilibrium state of a thin superconducting loop. *Phys. Rev. B*, **55**, 6551, 1997.

[118] J. Friedel. Metallic alloys. *Nuovo Cimento Suppl.*, **7**, 287, 1958.

[119] W. Zwerger, L. Bönig, and K. Schönhammer. Exact scattering theory for the landauer residual-resistivity dipole. *Phys. Rev. B*, **43**, 6434, 1991.

[120] R. Kanamoto, L. D. Carr, and M. Ueda. Topological Winding and Unwinding in Metastable Bose-Einstein Condensates. *Phys. Rev. Lett.*, **100**, 060401, 2008.

[121] R. Kanamoto, L. D. Carr, and M. Ueda. Metastable quantum phase transitions in a periodic one-dimensional Bose gas: Mean-field and Bogoliubov analyses. *Phys. Rev. A*, **79**, 063616, 2009.

[122] R. Desbuquois, L. Chomaz, J. Yefsah, T. Leonard, J. Beugnon, C. Weitenberg, and J. Dalibard. Superfluid behaviour of a two-dimensional Bose gas. *Nat. Phys.*, **8**, 645, 2012.

[123] C. L. Kane and M. P. A. Fisher. Transmission through barriers and resonant tunneling in an interacting one-dimensional electron gas. *Phys. Rev. B*, **46**, 15233, 1992.

[124] M. P. A. Fisher and L. I. Glazman. *Transport in a One-Dimensional Luttinger Liquid*, volume 345 of *NATO ASI Series E*, page 331. L. L. Sohn, L. P. Kouwenhoven, and G. Schön, 1997.

[125] Yu. Kagan, N. V. Prokof'ev, and B. V. Svistunov. Supercurrent stability in a quasi-one-dimensional weakly interacting Bose gas. *Phys. Rev. A*, **61**, 045601, 2000.

[126] U. Weiss. Low-temperature conduction and DC current noise in a quantum wire with impurity. *Solid State Communications*, **100**, 281, 1996.

[127] J. M. Luttinger. The Effect of a Magnetic Field on Electrons in a Periodic Potential. *Phys. Rev.*, **84**, 814, 1951.

[128] K. K. Das, M. D. Girardeau, and E. M. Wright. Interference of a Thermal Tonks Gas on a Ring. *Phys. Rev. Lett.*, **89**, 170404, 2002.

[129] E. K. Riedel and F. von Oppen. Mesoscopic persistent current in small rings. *Phys. Rev. B*, **47**, 15449, 1993.

[130] J. Clarke and I. Braginski. *The SQUID Handbook*. Wiley, Weinheim, 2004.

[131] C. Ryu, P. W. Blackburn, A. A. Blinova, and M. G. Boshier. Experimental realization of josephson junctions for an atom SQUID. *Phys. Rev. Lett.*, **111**, 205301, 2013.

[132] J. R. Friedman, V. Patel, W. Chen, S. K. Tolpygo, and J. E. Lukens. Quantum superposition of distinct macroscopic states. *Nature*, **406**, 43, 2000.

[133] C. H. van der Wal, A. C. J. ter Haar, F. K. Wilhelm, R. N. Schouten, C. J. P. M. Harmans, T. P. Orlando, Seth Lloyd, and J. E. Mooij. Quantum Superposition of Macroscopic Persistent-Current States. *Science*, **290**, 773, 2000.

[134] J. Clarke and F. K. Wilhelm. Superconducting quantum bits. *Nature*, **453**, 1031, 2008.

[135] L. Amico, D. Aghamalyan, F. Auksztol, H. Crepaz, R. Dumke, and L.-C. Kwek. Superfluid qubit systems with ring shaped optical lattices. *Sci. Rep.*, **4**, 4298, 2014.

[136] A. Nunnenkamp, A. M. Rey, and K. Burnett. Generation of macroscopic superposition states in ring superlattices. *Phys. Rev. A*, **77**, 023622, 2008.

[137] L. Amico, A. Osterloh, and F. Cataliotti. Quantum Many Particle Systems in Ring-Shaped Optical Lattices. *Phys. Rev. Lett.*, **95**, 063201, 2005.

[138] M. Aidelsburger, M. Atala, S. Nascimbène, S. Trotzky, Y.-A. Chen, and I. Bloch. Experimental Realization of Strong Effective Magnetic Fields in an Optical Lattice. *Phys. Rev. Lett.*, **107**, 255301, 2011.

[139] J. Struck, C. Ölschläger, M. Weinberg, P. Hauke, J. Simonet, A. Eckardt, M. Lewenstein, K. Sengstock, and P. Windpassinger. Tunable Gauge Potential for Neutral and Spinless Particles in Driven Optical Lattices. *Phys. Rev. Lett.*, **108**, 225304, 2012.

[140] M. Atala, M. Aidelsburger, J. T. Barreiro, D. Abanin, T. Kitagawa, E. Demler, and I. Bloch. Direct measurement of the Zak phase in topological Bloch bands. *Nat. Phys.*, **9**, 795, 2013.

[141] M. P. A. Fisher, P. B. Weichman, G. Grinstein, and D. S. Fisher. Boson localization and the superfluid-insulator transition. *Phys. Rev. B*, **40**, 546, 1989.

[142] M. Greiner, O. Mandel, T. Esslinger, T. W. Hänsch, and I. Bloch. Quantum phase transition from a superfluid to a Mott insulator in a gas of ultracold atoms. *Nature*, **415**, 39, 2001.

[143] M. Niemeyer, J.K. Freericks, and H. Monien. Strong-coupling perturbation theory for the two-dimensional Bose-Hubbard model in a magnetic field. *Phys. Rev. B*, **60**, 2357, 1999.

[144] P. Jordan and E. Wigner. Über das Paulische Äquivalenzverbot. *Z. Phys.*, **47**, 631, 1928.

[145] M. Rigol and A. Muramatsu. Ground-state properties of hard-core bosons confined on one-dimensional optical lattices. *Phys. Rev. A*, **72**, 013604, 2005.

[146] K. Hettiarachchilage, V. G. Rousseau, K.-M. Tam, M. Jarrell, and J. Moreno. Phase diagram of the Bose-Hubbard model on a ring-shaped lattice with tunable weak links. *Phys. Rev. A*, **87**, 051607, 2013.

[147] N. W. Ashcroft and N. D. Mermin. *Solid State Physics*. Holt, Rinehardt and Winston, New York, 1976.

[148] D. S. Jin, J. R. Ensher, M. R. Matthews, C. E. Wieman, and E. A. Cornell. Collective Excitations of a Bose-Einstein Condensate in a Dilute Gas. *Phys. Rev. Lett.*, **77**, 420, 1996.

[149] M.-O. Mewes, M. R. Andrews, N. J. van Druten, D. M. Kurn, D. S. Durfee, C. G. Townsend, and W. Ketterle. Collective Excitations of a Bose-Einstein Condensate in a Magnetic Trap. *Phys. Rev. Lett.*, **77**, 988, 1996.

[150] D. S. Jin, M. R. Matthews, J. R. Ensher, C. E. Wieman, and E. A. Cornell. Temperature-Dependent Damping and Frequency Shifts in Collective Excitations of a Dilute Bose-Einstein Condensate. *Phys. Rev. Lett.*, **78**, 764, 1997.

[151] D. M. Stamper-Kurn, H.-J. Miesner, S. Inouye, M. R. Andrews, and W. Ketterle. Collisionless and hydrodynamic excitations of a bose-einstein condensate. *Phys. Rev. Lett.*, **81**, 500, 1998.

[152] O. M. Maragò, S. A. Hopkins, J. Arlt, E. Hodby, G. Hechenblaikner, and C. J. Foot. Observation of the Scissors Mode and Evidence for Superfluidity of a Trapped Bose-Einstein Condensed Gas. *Phys. Rev. Lett.*, **84**, 2056, 2000.

[153] C. Fort, F. S. Cataliotti, L. Fallani, F. Ferlaino, P. Maddaloni, and M. Inguscio. Collective Excitations of a Trapped Bose-Einstein Condensate in the Presence of a 1D Optical Lattice. *Phys. Rev. Lett.*, **90**, 140405, 2003.

[154] G. Bismut, B. Pasquiou, E. Maréchal, P. Pedri, L. Vernac, O. Gorceix, and B. Laburthe-Tolra. Collective Excitations of a Dipolar Bose-Einstein Condensate. *Phys. Rev. Lett.*, **105**, 040404, 2010.

[155] M. K. Tey, L. A. Sidorenkov, E. R. S. Guajardo, R. Grimm, M. J. H. Ku, M. W. Zwierlein, Y.-H. Hou, L. Pitaevskii, and S. Stringari. Collective Modes in a Unitary Fermi Gas across the Superfluid Phase Transition. *Phys. Rev. Lett.*, **110**, 055303, 2013.

[156] K. G. Singh and D. S. Rokhsar. Collective Excitations of a Confined Bose Condensate. *Phys. Rev. Lett.*, **77**, 1667, 1996.

[157] S. Stringari. Collective Excitations of a Trapped Bose-Condensed Gas. *Phys. Rev. Lett.*, **77**, 2360, 1996.

[158] D. Guéry-Odelin and S. Stringari. Scissors Mode and Superfluidity of a Trapped Bose-Einstein Condensed Gas. *Phys. Rev. Lett.*, **83**, 4452, 1999.

[159] A. Minguzzi and M. P. Tosi. Scissors mode in a superfluid Fermi gas. *Phys. Rev. A*, **63**, 023609, 2001.

[160] A. Minguzzi, P. Vignolo, M. L. Chiofalo, and M. P. Tosi. Hydrodynamic excitations in a spin-polarized Fermi gas under harmonic confinement in one dimension. *Phys. Rev. A*, **64**, 033605, 2001.

[161] S. Montangero, R. Fazio, P. Zoller, and G. Pupillo. Dipole oscillations of confined lattice bosons in one dimension. *Phys. Rev. A*, **79**, 041602, 2009.

[162] M. Edwards, P. A. Ruprecht, K. Burnett, R. J. Dodd, and Charles W. Clark. Collective Excitations of Atomic Bose-Einstein Condensates. *Phys. Rev. Lett.*, **77**, 1671, 1996.

[163] A. Altmeyer, S. Riedl, C. Kohstall, M. J. Wright, R. Geursen, M. Bartenstein, C. Chin, J. Hecker Denschlag, and R. Grimm. Precision Measurements of Collective Oscillations in the BEC-BCS Crossover. *Phys. Rev. Lett.*, **98**, 040401, 2007.

[164] I. Ferrier-Barbut, M. Delehaye, S. Laurent, A. T. Grier, M. Pierce, B. S. Rem, F. Chevy, and C. Salomon. A mixture of Bose and Fermi superfluids. *Science*, **345**, 1035, 2014.

[165] L. P. Pitaevskii and A. Rosch. Breathing modes and hidden symmetry of trapped atoms in two dimensions. *Phys. Rev. A*, **55**, R853, 1997.

[166] C. Menotti and S. Stringari. Collective oscillations of a one-dimensional trapped Bose-Einstein gas. *Phys. Rev. A*, **66**, 043610, 2002.

[167] P. Pedri, S. De Palo, E. Orignac, R. Citro, and M. L. Chiofalo. Collective excitations of trapped one-dimensional dipolar quantum gases. *Phys. Rev. A*, **77**, 015601, 2008.

[168] M. Olshanii, H. Perrin, and V. Lorent. Example of a Quantum Anomaly in the Physics of Ultracold Gases. *Phys. Rev. Lett.*, **105**, 095302, 2010.

[169] E. Haller, M. Gustavsson, M. J. Mark, J. G. Danzl, R. Hart, G. Pupillo, and H.-C. Nägerl. Realization of an Excited, Strongly Correlated Quantum Gas Phase. *Science*, **325**, 1224, 2009.

[170] J. Catani, G. Lamporesi, D. Naik, M. Gring, M. Inguscio, F. Minardi, A. Kantian, and T. Giamarchi. Quantum dynamics of impurities in a one-dimensional Bose gas. *Phys. Rev. A*, **85**, 023623, 2012.

[171] I. Stroescu, D. B. Hume, and M. K. Oberthaler. Double-well atom trap for fluorescence detection at the Heisenberg limit. *Phys. Rev. A*, **91**, 013412, 2015.

[172] W. Kohn. Cyclotron Resonance and de Haas-van Alphen Oscillations of an Interacting Electron Gas. *Phys. Rev.*, **123**, 1242, 1961.

[173] J. Dobson. Harmonic-Potential Theorem: Implications for Approximate Many-Body Theories. *Phys. Rev. Lett.*, **73**, 2244, 1994.

[174] N. Strohmaier, K. Takasu, Y.and Günter, R. Jördens, M. Köhl, H. Moritz, and T. Esslinger. Interaction-Controlled Transport of an Ultracold Fermi Gas. *Phys. Rev. Lett.*, **99**, 220601, 2007.

[175] S. Peotta, D. Rossini, M. Polini, F. Minardi, and R. Fazio. Quantum Breathing of an Impurity in a One-Dimensional Bath of Interacting Bosons. *Phys. Rev. Lett.*, **110**, 015302, 2013.

[176] J. Léonard, M. Lee, A. Morales, T. M. Karg, T. Esslinger, and T. Donner. Optical transport and manipulation of an ultracold atomic cloud using focus-tunable lenses. *New J. Phys.*, **16**, 093028, 2014.

[177] T. Busch and G. Huyet. Low-density, one-dimensional quantum gases in a split trap. *Journal of Physics B: Atomic, Molecular and Optical Physics*, **36**, 2553, 2003.

[178] M. Abramowitz and I. A. Stegun. *Handbook of Mathematical Functions*. Dover, New York, 1972.

[179] J. Goold, M. Krych, Z. Idziaszek, T. Fogarty, and T. Busch. An eccentrically perturbed Tonks-Girardeau gas. *New J. Phys.*, **12**, 093041, 2010.

[180] R. Citro, S. De Palo, E. Orignac, P. Pedri, and M.-L. Chiofalo. Luttinger hydrodynamics of confined one-dimensional Bose gases with dipolar interactions. *New J. Phys.*, **10**, 045011, 2008.

[181] V. Dunjko, V. Lorent, and M. Olshanii. Bosons in Cigar-Shaped Traps: Thomas-Fermi Regime, Tonks-Girardeau Regime, and In Between. *Phys. Rev. Lett.*, **86**, 5413, 2001.

[182] P. Vignolo, A. Minguzzi, and M. P. Tosi. Light scattering from a degenerate quasi-one-dimensional confined gas of noninteracting fermions. *Phys. Rev. A*, **64**, 023421, 2001.

[183] I. Danshita. Universal Damping Behavior of Dipole Oscillations of One-Dimensional Ultracold Gases Induced by Quantum Phase Slips. *Phys. Rev. Lett.*, **111**, 025303, 2013.